

DEPARTMENT OF AEROSPACE ENGINEERING
COLLEGE OF ENGINEERING & TECHNOLOGY
OLD DOMINION UNIVERSITY
NORFOLK, VIRGINIA 23529

Final Report
W-34-C2
5 CT
Overpage

**AEROELASTIC, CFD, AND DYNAMIC COMPUTATION AND
OPTIMIZATION FOR BUFFET AND FLUTTER APPLICATIONS**

By

Osama Kandil, Principal Investigator

Final Report

For the period October 1, 1994 through November 30, 1995

Prepared for

National Aeronautics and Space Administration
Langley Research Center
Hampton, VA 23681-0001

Under

Research Grant NAG-1-⁶⁴⁸994

Dr. Robert M. Bennett, Technical Monitor
SD-Aeroelastic Anal & Optim Branch

February 1996

DEPARTMENT OF AEROSPACE ENGINEERING
COLLEGE OF ENGINEERING & TECHNOLOGY
OLD DOMINION UNIVERSITY
NORFOLK, VIRGINIA 23529

**AEROELASTIC, CFD, AND DYNAMIC COMPUTATION AND
OPTIMIZATION FOR BUFFET AND FLUTTER APPLICATIONS**

By

Osama Kandil, Principal Investigator

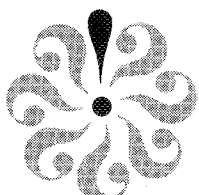
Final Report

For the period October 1, 1994 through November 30, 1995

Prepared for
National Aeronautics and Space Administration
Langley Research Center
Hampton, VA 23681-0001

Under *648*
Research Grant NAG-1-994
Dr. Robert M. Bennett, Technical Monitor
SD-Aeroelastic Anal & Optim Branch

Submitted by the
Old Dominion University Research Foundation
P.O. Box 6369
Norfolk, VA 23508-0369



February 1996

**AEROELASTIC, CFD AND DYNAMICS COMPUTATION AND
OPTIMIZATION FOR BUFFET AND FLUTTER APPLICATIONS**

GRANT NO. NAG-1-648

Osama A. Kandil

Aerospace Engineering Department

Old Dominion University, Norfolk, VA 23529-0247

ACCOMPLISHMENTS

In the period of October 1, 1994 to November 30, 1995, the Principal Investigator (PI) along with the assistance of three Ph.D. students have achieved the following accomplishments under this grant:

I. Publications

- I.1. Kandil, O.A. and Menzies, M.A., "Coupled Rolling and Pitching Oscillation Effects on a Transonic Shock-Induced Vortex Breakdown Flow on a Delta Wing," AIAA 96-0828, AIAA 34th Aerospace Sciences Meeting, Reno, NV, January 15-18, 1996.
- I.2. Kandil, O.A. and Menzies, M.A., "Effects of Coupled Rolling and Pitching Oscillations on Transonic Shock-Induced Vortex Breakdown Flow on a Delta Wing," Proceedings of Sixth International Symposium on CFD, Vol. II, pp. 564-569, Lake Tahoe, NV, September 4-8, 1995 (Invited Paper).
- I.3. Kandil, O.A., Sheta, E.F. and Massey, S.J., "Buffet Responses of a Vertical Tail in Vortex Breakdown Flows," AIAA 95-3464-CP, AIAA Atmospheric Flight Mechanics Conference, Baltimore, MD, August 7-10, 1995, pp. 345-360.
- I.4 Menzies, M., Kandil, O.A., and Kandil, H.A., "Forced Rolling Oscillation of A 65°-Delta Wing in Transonic Vortex Breakdown Flow," AIAA 95-1771-CP, Applied Aerodynamics Conference, San Diego, CA, June 19-22, 1995, pp. 69-89.
- I.5. Kandil, O.A., Massey, S.J. and Sheta, E.F., "Structural Dynamics/CFD Interaction For Computation of Vertical Tail Buffet," The Royal Aeronautical Society, International Forum

on Aeroelasticity and Structural Dynamics, RAS Paper No. 16.52, Manchester, UK, June 26-28, 1995, pp. 52.1-52.14.

I.6. Hu, H. and Kandil, O.A., "A Hybrid Boundary Element-Finite Volume Method for Unsteady Transonic Airfoil Flows," Journal of Engineering Analysis with Boundary Elements, Elsevier, vol. 14, pp. 149-157, 1995.

II. Abstracts Submitted to Technical Conferences:

II.1 Kandil, O.A., Massey, S.J. and Sheta, E.F., "Prediction of Tail Buffet On a Delta Wing-Twin Vertical Tail Configuration," AIAA Applied Aerodynamics Conference, New Orleans, LA, June 17-20, 1996.

II.2. Kandil, O.A., Massey, S.J. and Sheta, E.F., 15th International Conference on Numerical Methods in Fluid Dynamics, Monterey, CA, June 24-28, 1996.

III. Animation Movies Produced

III.1. "Coupled CFD/Structural Dynamics Computations of Vertical Tail Buffet," Kandil, O.A., Massey, S.J. and Sheta, E.F., June 20, 1995.

III.2. "Rolling Oscillations of a Delta Wing in Transonic Vortex Breakdown Flow," Kandil, O.A. and Menzies, M.A., December 8, 1994.

Forty copies of each animation movie have been produced and distributed to the Technical Monitor, Branch Head, Division Chief, Deputy Director of Research and Technology group; all of NASA Langley Research Center. They have also been distributed to interested national and international technical scientists and groups.

IV. Graduate Students

There are three Ph.D. students working with the P.I. on this Research Grant. They are supported by this grant and the Aerospace Engineering Department of Old Dominion University. These students are:

IV.1. Ms. Margaret A. Menzies (US Citizen): She joined the AE Dept. in May 1993 for her Ph.D. degree. She has been supported under this grant, a fellowship from the AE Dept. and The Virginia Space Consortium Fellowship. She passed her qualifying examination in February 1995 and is expected to finish her degree in May or August, 1996. Her Ph.D. dissertation focuses on forced and natural single and multi-mode-coupled responses of a delta wing in transonic vortex breakdown flows.

IV.2. Mr. Steven J. Massey (US Citizen): He has been working on his Ph.D. degree since May 1994. He has been supported under this grant and a Fellowship from the AE Dept. He passed the written part of his Ph.D. Qualifying Examination in Fall 1995. He will take the oral part in February 1996 and is expected to finish his Ph.D. degree in May or August, 1997. His Ph.D. dissertation focuses on single and twin tail buffet of a delta wing-vertical tails configuration undergoing bending and torsional vibrations, including buffet control.

IV.3. Mr. Mark W. Flanagan (US Citizen): He has been working on his Ph.D. degree since January 1994. He has been supported under this grant and a Fellowship from the AE Dept. He passed the written part of his Ph.D. Qualifying Examination in Fall 1995. He will take the oral part in February 1996 and is expected to finish his Ph.D. degree in August, 1997. His Ph.D. dissertation focuses on simulation and optimizational control of tail buffet in supersonic internal vortex breakdown flows in a configured duct.

V. Conference and Technical Meetings Presentations and Activities:

V.1. "Coupled Rolling and Pitching Oscillation Effects on a Transonic Shock-Induced Vortex Breakdown Flow on a Delta Wing," AIAA 34th ASM, Reno, NV, January 15-18, 1996.
Ms. M.A. Menzies will give the presentation.

V.2. "Effects of Coupled Rolling and Pitching Oscillations on Transonic Shock-Induced Vortex Breakdown Flow on a Delta Wing," Sixth International symposium on CFD, Lake Tahoe, NV, September 4-8, 1995. Prof. O.A. Kandil gave the presentation.

- V.3. "Forced Coupled Rolling and Pitching Oscillations of a Delta Wing in Transonic Vortex Breakdown Flow," Aerospace Engineering Department Seminar, Old Dominion University, Norfolk, VA, October 6, 1995. Ms. M.A. Menzies gave the presentation.
- V.4. "Computational Simulation and Analysis of Tail Buffet and Delta wing Coupled-Oscillation Responses," Aeroelasticity Branch Briefing on the Grant Accomplishments, August 24, 1995. Prof. O.A. Kandil gave the presentation.
- V.5. "Buffet Responses of a Vertical Tail in Vortex Breakdown Flows," AIAA Atmospheric Flight Mechanics Conference, Baltimore, MD, August 7-10, 1995. Mr. Steven Massey gave the presentation.
- V.6. "Forced rolling Oscillation of A 65°-Delta Wing in Transonic Vortex Breakdown Flow," Applied Aerodynamics Conference, San Diego, CA, June 19-22, 1995. Prof. O.A. Kandil gave the presentation.
- V.7. "Structural Dynamics/CFD Interaction for Computation of Vertical Tail Buffet," International Forum on Aeroelasticity and Structural Dynamics, Royal Aeronautical society, University of Manchester, Manchester, UK, June 28, 1995. Prof. O.A. Kandil gave the presentation.



NASA-648
51-023
38275

Donnide

AIAA-96-0828

Coupled Rolling and Pitching Oscillation Effects on Transonic Shock-Induced Vortex-Breadown Flow of a Delta Wing

Osama A. Kandil and Margaret A. Menzies

**Aerospace Engineering Department
Old Dominion University
Norfolk VA 23529**

**34th Aerospace Sciences
Meeting and Exhibit
Reno NV-January 13-18, 1996**

Coupled Rolling and Pitching Oscillation Effects on Transonic Shock-Induced Vortex-Breakdown Flow of a Delta Wing

Osama A. Kandil[†] and Margaret A. Menzies[‡]

Aerospace Engineering Department
Old Dominion University, Norfolk, VA 23529

ABSTRACT

Unsteady, transonic vortex dominated flow over a 65° sharp edged, cropped-delta wing of zero thickness undergoing forced coupled pitching and rolling oscillations is investigated computationally. The wing mean angle of attack is 20° and the free stream Mach number and Reynolds number are 0.85 and 3.23×10^6 , respectively. The initial condition of the flow is characterized by a transverse terminating shock and vortex breakdown of the leading edge vortex cores. The computational investigation uses the time-accurate solution of the laminar, unsteady, compressible, full Navier-Stokes equations with the implicit, upwind, Roe flux-difference splitting, finite-volume scheme. The main focus is to analyze the effects of coupled motion on the wing response and vortex-breakdown flow by varying oscillation frequency and phase angle while the maximum pitch and roll amplitude is kept constant at 4.0°. Four cases demonstrate the following: simultaneous motion at a frequency of 1π , motion with a 90° phase lead in pitch, motion with a rolling frequency of twice the pitching frequency, and simultaneous motion at a frequency of 2π . Comparisons with single mode motion at these frequencies complete this study and illustrate the effects of coupling the oscillations.

INTRODUCTION

Recent experimental measurements of transonic flows around 65° cropped delta wing¹⁻⁴ show that a complex shock-wave system appears over the upper wing surface. The shock-wave system consists of a ray shock wave beneath the leading-edge primary vortex and a transverse, time dependent², normal-shock wave (known as a terminating shock) which runs from the plane of symmetry to the wing leading edge. The terminating shock wave interacts with the primary-vortex core causing it to breakdown at an angle of attack as low as 18°.

Computational simulations for transonic delta-wing flows have been developed on a very limited scale by using the Euler equations^{3,5} and the thin-layer Navier-Stokes equations⁶. The Euler equations solutions were not capable of fully resolving the flow in the terminating shock region and the thin-layer Navier-Stokes equations solutions did not address that region. In Refs. 7 and 8, by Kandil, Kandil, and Liu, the laminar, unsteady, compressible, full Navier-Stokes equations are integrated time accurately to study and construct the flow field structure of a transonic flow around a 65° sharp-edged, cropped-delta wing at 20° angle of attack, 0.85 Mach number and 3.23×10^6 Reynolds number. A shock system, which consists of a ray shock under the primary vortex core and a transverse terminating shock, has been captured. Behind the terminating shock, the leading-edge vortex core breaks down into a bubble type. The flow field ahead of the terminating shock includes a supersonic pocket which is surrounded by the ray shock and the terminating shock. These results have been validated using the available experimental data and they are in good agreement.

In a recent computational study by Menzies, Kandil, and Kandil,¹⁰ interesting effects of the rolling frequency on the vortex breakdown were shown. The computational investigation in Ref. 10 has been performed on the same wing as that of Refs. 7 and 8. It has been shown that a forced rolling oscillation around the axis of symmetry with a maximum roll amplitude of 4.0° and a reduced frequency of 2π eliminated the vortex breakdown of the leading-edge vortex cores, and increased the lift coefficient by 19.5% of its original mean value. In this paper, a complete investigation of the effects of forced coupled rolling and pitching oscillations is presented. Of particular interest is the effect of the reduced frequency and phase angle on the vortex breakdown and the aerodynamic response of the wing.

FORMULATION

Governing Equations:

The conservative form of the dimensionless, unsteady, compressible, full Navier-Stokes equations in

[†]Professor, Eminent Scholar and Department Chairman, AIAA Associate Fellow.

[‡]Graduate Research Assistant, AIAA Member.

Copyright © 1996 by Osama A. Kandil. Published by the American Institute of Aeronautics and Astronautics, Inc. with permission.

terms of the time-dependent, body-conformed coordinates ξ^1 , ξ^2 , and ξ^3 , is given by:

$$\frac{\partial \bar{Q}}{\partial t} + \frac{\partial \bar{E}_m}{\partial \xi^m} - \frac{\partial (\bar{E}_v)_s}{\partial \xi^s} = 0 \quad (1)$$

$$m = 1, 2, 3; s = 1, 2, 3$$

where

$$\xi^m = \xi^m(x_1, x_2, x_3, t) \quad (2)$$

$$\bar{Q} = \frac{\hat{q}}{J} = \frac{1}{J} [\rho, \rho u_1, \rho u_2, \rho u_3, \rho e]^t \quad (3)$$

The definitions of the inviscid and viscous fluxes; \bar{E}_m and $(\bar{E}_v)_s$ are given in Ref. 9.

Boundary and Initial Conditions and Grid Motion:

All boundary conditions are explicitly implemented. They include inflow-outflow conditions, solid-boundary conditions and plane of geometric symmetry conditions. At the plane of geometric symmetry, periodic conditions are enforced. At the inflow boundaries, the Riemann-invariant boundary-type conditions are enforced. At the outflow boundaries, first-order extrapolation from the interior point is used.

Since the wing is undergoing coupled motion, the grid is moved with the same angular motion as that of the body. The grid speed, $\frac{\partial \xi^m}{\partial t}$, and the metric coefficient, $\frac{\partial \xi^m}{\partial x_n}$, are computed at each time step of the computational scheme. Consequently, the kinematical boundary conditions at the inflow-outflow boundaries and at the wing surface are expressed in terms of the relative velocities. The dynamical boundary condition, $\frac{\partial p}{\partial n}$, on the wing surface is no longer equal to zero. This condition is modified for the oscillating wing as:

$$\frac{\partial p}{\partial n} \Big|_{wing} = -\rho \vec{a} \cdot \hat{n} \quad (4)$$

where \vec{a} is the acceleration of a point on the wing flat surface; \hat{n} , the unit normal to the wing surface which is equal to the unit vector \vec{e}_z for a flat surface. The acceleration is given by:

$$\vec{a} = \vec{\Omega} \times \vec{r} + \vec{\Omega} \times (\vec{\Omega} \times \vec{r}) \quad (5)$$

where $\vec{\Omega}$ is the angular velocity. Notice that for a rigid body, the position vector \vec{r} , is not a function of time and hence, $\dot{\vec{r}} = \ddot{\vec{r}} = 0$. Finally, the boundary condition for the temperature is obtained from the adiabatic boundary condition and is given by:

$$\frac{\partial T}{\partial n} \Big|_{wing} = 0 \quad (6)$$

The initial conditions correspond to the flow solution around a stationary wing at an angle of attack of 20° that was impulsively inserted into a free stream with $M_\infty = 0.85$, and Reynolds number of 3.23×10^6 . The solution after 18,000 time steps with a time step of $\Delta t = 0.0002$ (corresponding to a total dimensionless time of 3.6) is then used for the starting point of all subsequent cases.

COMPUTATIONAL SCHEME

The implicit, upwind, flux-difference splitting, finite-volume scheme is used to solve the unsteady, compressible, full Navier-Stokes equations. This scheme uses the flux-difference splitting of Roe and a smooth flux limiter is used to eliminate oscillation at locations of large flow gradients. The viscous and heat flux terms are linearized in time and the cross derivative terms are eliminated in the implicit operator and retained in the explicit terms. The viscous terms are differenced using second-order accurate central differencing. The resulting difference equation is approximately factored to solve the equations in three sweeps in the ξ^1 , ξ^2 , and ξ^3 , directions. The computational scheme is coded in the computer program "FTNS3D"

The method of solution consists of two steps. In the first step, the problem is solved for the stationary wing at 20° angle of attack and a 0° roll angle. This solution represents the initial conditions for the second step. In the second step, the wing pitching and rolling functions are specified and the Navier-Stokes equations are solved accurately in time. At each time step, the wing and the grid are rotated through angles corresponding to the wing pitching and rolling angle. The metric coefficients and the grid speed are computed and the Roe flux-differencing scheme is used to obtain the solution. The computations proceed until periodic response is reached.

COMPUTATIONAL RESULTS AND DISCUSSION

A 65° swept-back, sharp edged, cropped delta wing of zero thickness is considered for the computational solutions. The cropping ratio (tip length/root-chord length) is 0.15. An O-H grid of $125 \times 85 \times 84$ in the wrap-around, normal, and axial directions, respectively, is used. The computational domain extends two-chord lengths forward and five-chord lengths backward from the wing trailing edge. The radius of the computational domain is four-chord lengths. The minimum grid size in the normal

direction to the wing surface is 5×10^{-4} from the leading edge to the plane of symmetry. The initial conditions correspond to the solution of the wing held at 20.0° angle of attack and 0.0° roll angle after 18,000 time steps. The grid is then coarsened due to impeding computational cost to $65 \times 43 \times 84$, wrap-around, normal, and axial directions, respectively. This is accomplished by retaining the odd numbered grid points in the wrap-around and normal directions. The cell centered fine solution is then interpolated to the coarsened grid by averaging in both the normal and lateral directions simultaneously.

Initial Condition (Stationary Wing):

$$\alpha_i = 20.0^\circ, \theta_i = 0.0^\circ$$

Plots of the initial condition depict a solution characterized by weak oblique shocks beneath the primary vortices and a terminating shock located at approximately $x = 0.86$ (See Fig. 1.) These shocks bound a substantial supersonic pocket. Immediately behind the transverse shock, centered about the plane of symmetry, a large high pressure region is observed. Careful study of the pressure contours in Fig. 1 shows that this area contains two regions of high pressure gradients; the leading edge, the terminating shock and at $x = 0.93$. Outboard of the oblique shocks, a subsonic, separated region depicts a secondary vortex which exists until $x = 0.91$. The primary vortex is enlarged at the vortex breakdown location and behaves as attracting and repelling spiral saddle critical points (not shown) indicating vortex breakdown due to the terminating shock. Plots of the Mach number contours, instantaneous streamlines, and surfaces of constant entropy are shown in Figure 2. These views depict clearly a bubble type vortex breakdown and the flow appears to be completely symmetric. The resulting lift coefficient is approximately 0.408.

Case I-Coupled Pitching and Rolling Oscillation: Same Frequency, $\alpha = 20^\circ + 4^\circ \sin \pi t$, $\theta = 4^\circ \sin \pi t$

From the initial condition, the wing is forced to oscillate in pitch around an axis located at the quarter-chord length and in roll around the axis of geometric symmetry. The amplitude of both the pitching, (α_a), and rolling, (θ_a), oscillation is 4.0° and the reduced frequency for the two motions, (k), is π . The period corresponding to the frequency is 2 and with a $\Delta t = 0.001$, each cycle of oscillation takes 2,000 time steps. The motion starts with the angle of attack increasing while simultaneously rolling with the left-hand side of the wing (looking in the upstream direction) rolling downward. The case was run for more than five complete cycles.

Figures 3, 4, and 5 compare the lift and rolling moment coefficient curves of the coupled in phase pitching and rolling case with the coefficient curves of the pitching-

alone and rolling-alone cases each studied separately, respectively. The lift coefficient curve of the coupled case is nearly identical to that of the pitching alone case while the rolling moment coefficient curve of the coupled case is nearly identical to the rolling alone case. This indicates that when the pitching and rolling oscillations are coupled, the lift-coefficient of the pitching-alone case and the rolling-moment coefficient of the rolling-alone case dominate the resulting responses. The coupled motions show periodic lift and rolling-moment coefficient responses.

Case II-Coupled Pitching and Rolling Oscillations: Effect of Phase Shift, $\alpha = 20^\circ + 4^\circ \sin \pi t$, $\theta = 4^\circ \sin \{\pi(t - 0.5)\}$

Restarting from the same initial condition as in Case I, the wing is again forced to oscillate in pitch around an axis located at the quarter-chord length and in roll around the axis of geometric symmetry with the same pitch and roll amplitude, ($\alpha_a, \theta_a = 4.0^\circ$), and reduced frequency, ($k = \pi$), as in Case I. For this case the motion starts with the angle of attack increasing without any rolling oscillation. Once the maximum angle of attack, ($\alpha = 24.0^\circ$), is attained, the wing is then forced to roll sinusoidally with the left-hand side of the wing (looking in the upstream direction) rolling downward while the angle of attack simultaneously decreases. This results in a 90° phase lead for the pitching motion. The case was run for more than five complete cycles of rolling.

Figures 6 is a plot of the motion, lift and rolling-moment coefficient curves of the coupled out of phase pitching and rolling case plotted versus time and both the angle of attack and the roll angle. With a 90° phase lead in the pitching motion, the lift coefficient curve is again nearly identical to that of pitching-alone case but the rolling-moment coefficient curve decreases with each cycle. With a phase lead, the breakdown of the vortices appears to strengthen as a result of coupling the motion and leads to a negative bias in the rolling moment curve.

Figure 7 shows snapshots of the Mach contours near the surface, instantaneous streamlines, and surfaces of constant entropy depicting the vortex core and breakdown. At $t = 9.0$, the wing is passing through a zero roll angle and an angle of attack of 20.0° and has reached peak pitch down velocity. Aft of the pitch axis of rotation, the wing is moving upwards, effectively compressing the fluid. In response, the position of the vortex cores and breakdown shifts upstream as compared to the breakdown position of the initial condition case.

Case III-Coupled Pitching and Rolling Oscillation: Frequency Effect, $\alpha = 20^\circ + 4^\circ \sin \pi t$, $\theta = 4^\circ \sin 2\pi t$

From the initial condition, the wing is forced to oscillate in pitch around an axis located at the quarter-chord length and in roll around the axis of geometric symmetry with the same pitch and roll amplitude, ($\alpha_a, \theta_a = 4.0^\circ$), as in Case I; however, the reduced frequency, (k), for the rolling oscillation is 2π -twice that of the pitching motion. In this case, the motion starts with the angle of attack increasing to the maximum angle of attack while the wing is simultaneously rolling with its left-hand side (looking in the upstream direction) downward then upward returning to 0° angle of roll before the angle of attack begins to decrease. Thus, the wing has 0° roll angle when its angle of attack is at the maximum, minimum, and mean values. This case was run for five complete cycles of pitching which equates to ten complete cycles of rolling.

Figure 8 shows the aerodynamic properties plotted versus the angle of attack and the roll angle, and a plot of the motion versus time. The coefficient of lift curve has the same characteristics as seen in Case I and II, but the general trend shows a distinct rise in lift as the motion continues. For comparison, plots of the lift coefficient for the rolling-alone at $k = 2\pi$ demonstrate that the lift coefficient rises with each cycle of motion until 6.5 cycles when periodicity is reached. (See Fig. 9). The rolling-moment coefficient reaches periodicity too.

Figure 10 compares snapshots of the Mach contours near the wing surface, instantaneous streamlines, and surfaces of constant entropy of the coupled oscillation case and the rolling-alone case. For the rolling-alone case, the terminating shock moved forward and dissipated as a result of the motion.¹⁰ It was surmised that the rolling motion causes one side to compress as that side of the wing moves upwards and the other to expand weakening the shock. When the motion is coupled at the different frequencies, the behavior of the shock over time is very similar to that of the rolling-alone case. However, the resultant coefficient of periodic lift of the coupled response is less than the lift of the rolling-alone case demonstrating the effect of the coupled motions.

Case IV-Coupled Pitching and Rolling Oscillation: Same Frequency, $\alpha = 20^\circ + 4^\circ \sin 2\pi t$, $\theta = 4^\circ \sin 2\pi t$

Again, from the initial condition, the wing is forced to oscillate in pitch around an axis located at the quarter-chord length and in roll around the axis of geometric symmetry with the same pitch and roll amplitude as in Case I; however, the reduced frequency, (k), for both the pitching and rolling oscillation is 2π -twice the value of Case I. As in the first case the motion starts with the angle of attack increasing while simultaneously rolling with the left-hand side of the wing (looking in the upstream direction) rolling downward. The case was run for one and a quarter cycles.

Figure 11 and 12 shows the aerodynamic properties plotted versus the angle of attack for both the coupled motion and the pitch-alone motion at a frequency of 2π , respectively. Comparison of the coefficient curves for the coupled motion and pitching-alone case, reveals that the lift coefficient and pitching moment coefficient curves are nearly identical. Comparison of the coefficient curves for the coupled motion case with the rolling-alone case, reveals that the rolling moment coefficient curve is also identical. The cases appear to be periodic after one and a quarter cycles and indicates that the coupling effect is similar to that of Case I.

CONCLUSIONS:

The unsteady, compressible, full Navier-Stokes equations are integrated time accurately using the implicit, upwind, flux-difference splitting, finite-volume scheme to study the unsteady transonic flow around a 65° sharp-edged, cropped delta wing. The wing is first forced to oscillate in pitch and roll with a maximum pitch amplitude, α_a , and roll amplitude, θ_a , of 4.0° and a reduced frequency, k , of π . The second case demonstrated the effect of a 90° pitching phase lead while maintaining the same amplitudes and reduced frequency. The third and fourth case increase the reduced frequency for the rolling motion and both rolling and pitching motion, respectively.

From these cases, it has been shown that even when coupled, forced rolling oscillation at a reduced frequency of $k = 2\pi$ eliminates the vortex breakdown which is washed downstream and results in an increase in the coefficient of lift. The coupling effect for in phase forced oscillations at a reduced frequency of $k = \pi$ and 2π shows that the lift-coefficient of the pitching-alone case and the rolling-moment coefficient of the rolling alone-case dominate the resulting response. However, with a phase lead in the pitching motion, the combination of forced rolling and pitching oscillations alter the vortex core position relative to the wing leading edge.

It has been shown that a phase shift and frequency difference between the pitching and rolling motions have substantial effects on the aerodynamic response of the wing and the vortex-breakdown flow. Using the computational methods described, complex details of unsteady, transonic flow around a delta wing undergoing coupled pitching and rolling oscillations of varied frequency and phase angle have been presented for the first time.

ACKNOWLEDGMENT

This work is supported by the NASA-Langley Research Center under grant No. NAG-1-648 along with

partial support from the Virginia Space Grant Consortium. The computational resources provided by the NAS Center at AMES and the NASA Langley Research Center are acknowledged and appreciated.

REFERENCES

- ¹Boersen, S. J. and Elsenaar, A., "Tests on the AFWAL 65° Delta Wing at NLR: A Study of Vortex Flow Development Between Mach = 0.4 and 4," Proceedings of Symposium on International Vortex Flow Experiment on Euler Code Validation, Stockholm, Sweden, October 1-3, 1986, pp. 23-36.
- ²Bannik, W. J. and Houtman, E. M., "Experiments on the Transonic Flow Over a Delta Wing at High Angles of Attack," Proceedings of Symposium on International Vortex Flow Experiment on Euler Code Validation, Stockholm, Sweden, October 1-3, 1986, pp. 37-46.
- ³Bannik, W. J. and Houtman, E. M., "Experimental and Computational Study of the Vortical Flow Over a Delta Wing at High Angles of Attack," IUTAM Symposium on Fluid Dynamics of High Angles of Attack, University of Japan, Tokyo, Japan, September 14-17, 1992.
- ⁴Erickson, G. E., "Wing Tunnel Investigation of the Interaction and Breakdown Characteristics of Slender-Wing Vortices at Subsonic, Transonic, and Supersonic Speeds," NASA Technical paper 3114, November 1991.
- ⁵Hitzel, S. M., "Wing Vortex-Flows Up into Vortex-Breakdown--A Numerical Simulation," AIAA 88-2518-CP, 1988, pp. 73-83.
- ⁶Laine, S., Siikonen, T., and Kaurinkoski, P., "Calculation of Transonic Viscous Flow Around a Delta Wing," ICAS 92-4.2.1, Beijing, Peoples Republic of China, September 22-25, 1992, pp. 286-295.
- ⁷Kandil, O. A., Kandil, H. A., and Liu, C. H., "Shock-Vortex Interaction Over a 65-Degree Delta Wing in Transonic Flow," AIAA Paper 93-2973, AIAA 24th Fluid Dynamics Conference, Orlando, FL, July 6-9, 1993.
- ⁸Kandil, H. A., Kandil, O. A., and Liu, C. H., "Supersonic Vortex Breakdown Over a Delta Wing in Transonic Flow," AIAA-93-3472-CP, AIAA Applied Aerodynamic Conference, Monterey, CA, August 9-11, 1993, pp. 582-596.
- ⁹Kandil, O. A. and Kandil, H. A., "Pitching Oscillation of a 65-Degree Delta Wing in Transonic Vortex Breakdown Flow," AIAA-94-1426-CP, AIAA/ASME/ASCE/AHS/ASC Structures and Structural Dynamics Conference, Hilton Head, SC, April 18-20, 1994.
- ¹⁰Menzies, M. A., Kandil, O. A., and Kandil, H. A., "Forced Rolling Oscillation of a 65°-Delta Wing in Transonic Vortex-Breakdown Flow," 13th AIAA Applied Aerodynamics Conference, Sheraton Harbor Island, San Diego, CA, June 19-22, 1995.

Initial Conditions

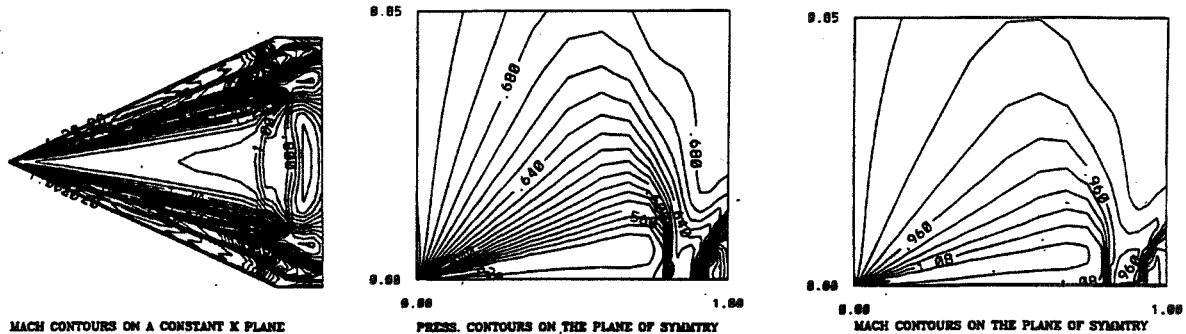


Figure 1. Mach Contours near the Wing Surface and Static Pressure Contours and Mach Contours on the Plane of Geometric Symmetry; $M_\infty = 0.85$, $Re = 3.23 \times 10^6$, $\alpha = 20.0^\circ$, $\theta = 0.0^\circ$.

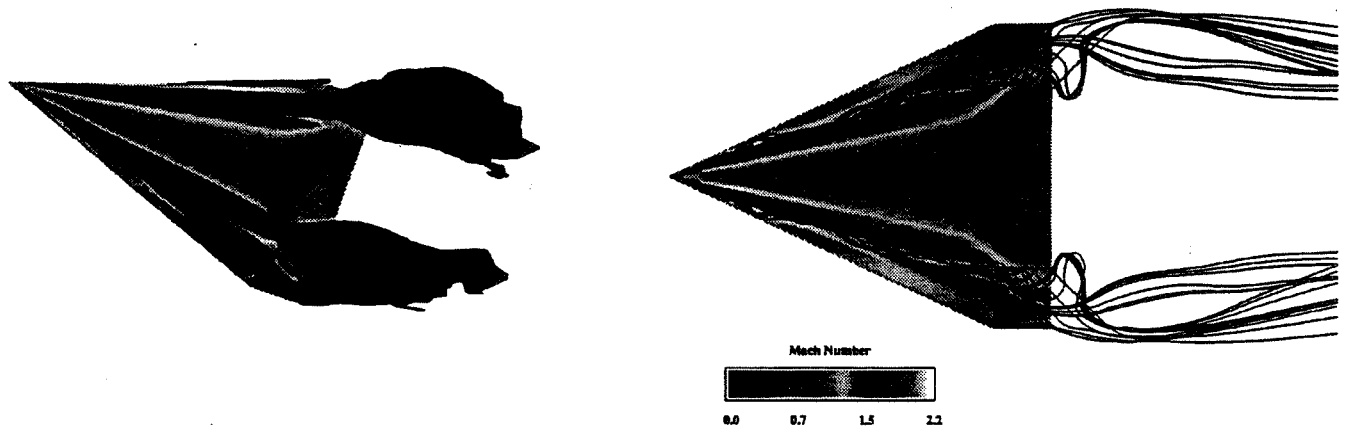


Figure 2. Mach Contours near the Wing Surface with Surfaces of Constant Entropy ($s = 0.5$) and Instantaneous Streamlines; $M_\infty = 0.85$, $Re = 3.23 \times 10^6$, $\alpha = 20.0^\circ$, $\theta = 0.0^\circ$.

Forced Coupled Pitching and Rolling Oscillation Case I

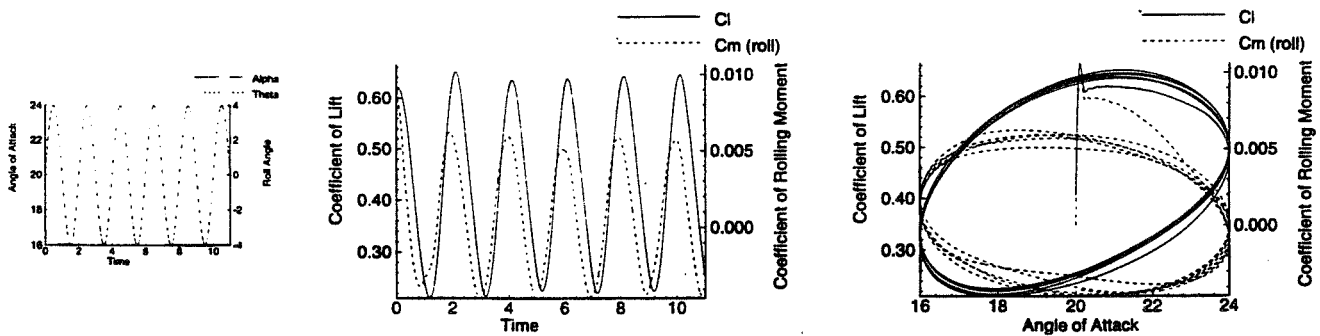


Figure 3. Aerodynamic Response, Forced Coupled Pitching and Rolling Oscillation Case I;
 $\alpha = 20.0^\circ + 4.0^\circ \sin(\pi t)$, $\theta = 4.0^\circ \sin(\pi t)$

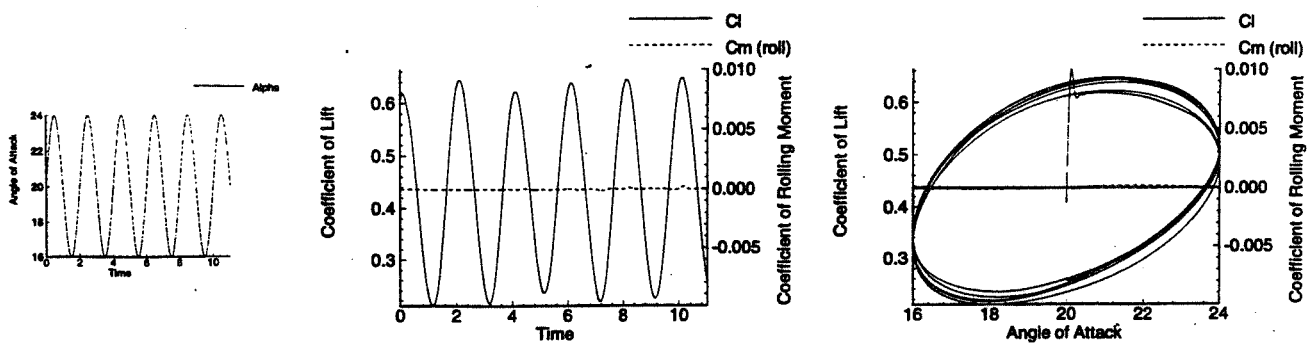


Figure 4. Aerodynamic Response, Forced Pitching-alone Oscillation Case I; $\alpha = 20.0^\circ + 4.0^\circ \sin(\pi t)$, $\theta = 0.0^\circ$

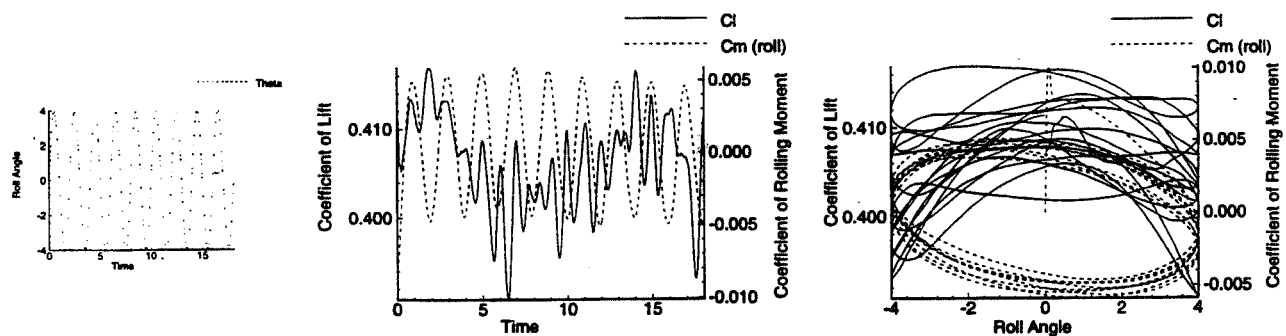


Figure 5. Aerodynamic Response, Forced Rolling-alone Oscillation Case I; $\alpha = 20.0^\circ$, $\theta = 4.0^\circ \sin(\pi t)$

Forced Coupled Pitching and Rolling Oscillation Case II

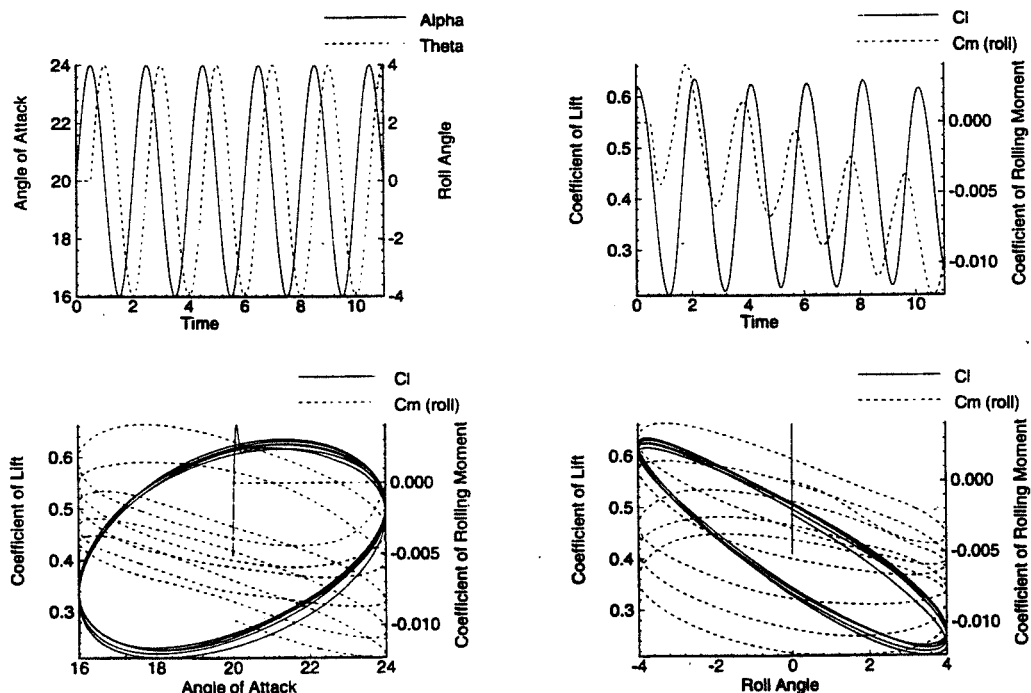


Figure 6. Aerodynamic Response, Forced Coupled Pitching and Rolling Oscillation Case II; $\alpha = 20.0^\circ + 4.0^\circ \sin(\pi t)$, $\theta = 4.0^\circ \sin(\pi(t - 0.5))$

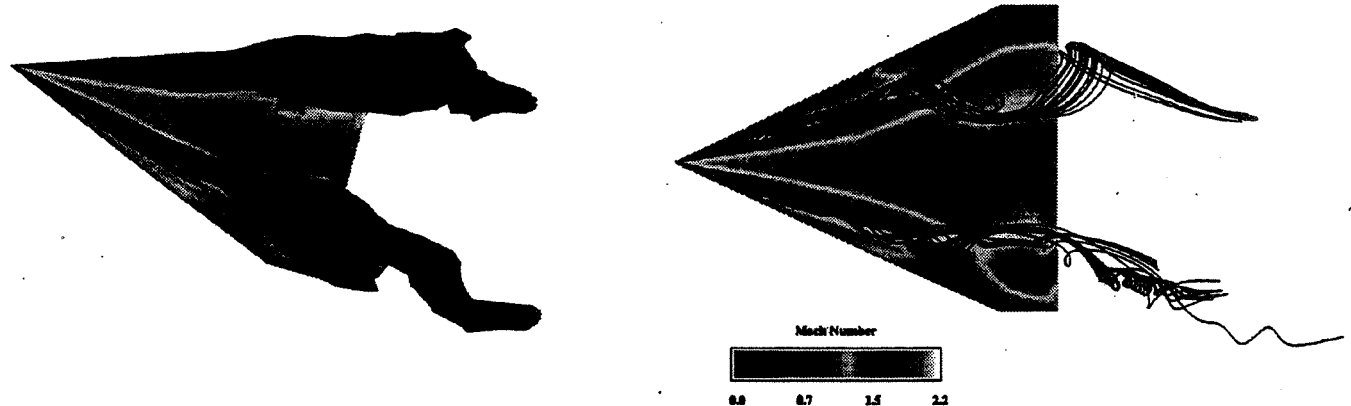


Figure 7. Mach Contours near the Wing Surface with Surfaces of Constant Entropy ($s = 0.5$) and Instantaneous Streamlines; at $t = 9.0$, $\alpha = 20.0^\circ$, $\theta = 4.0^\circ$ (maximum pitch down velocity and maximum positive roll angle)

Forced Coupled Pitching and Rolling Oscillation Case III

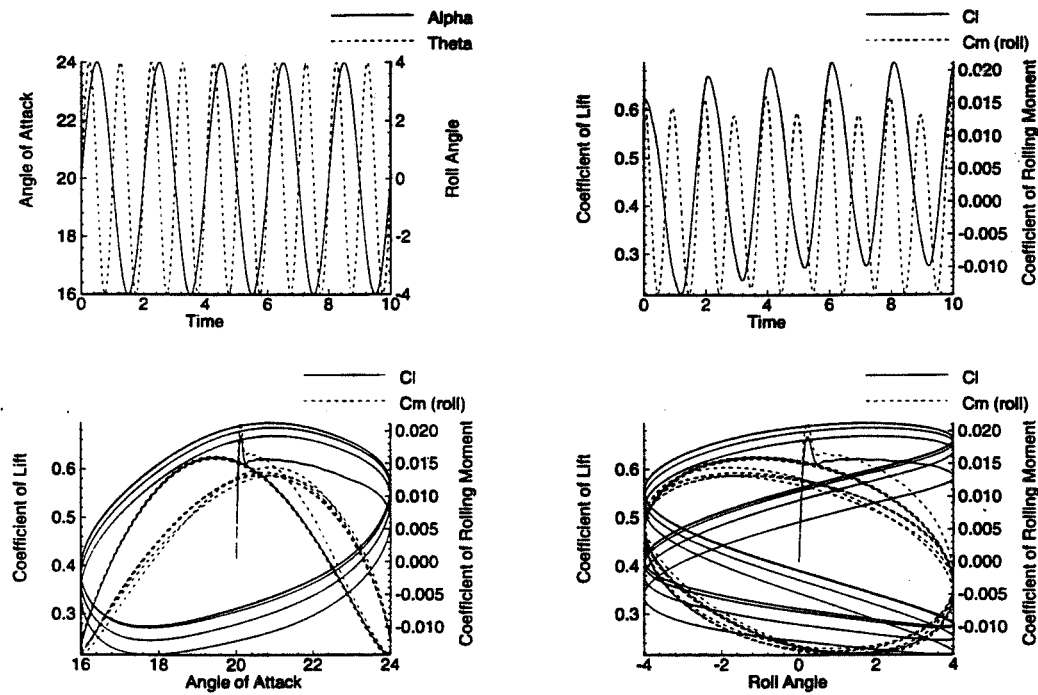


Figure 8. Aerodynamic Response, Forced Coupled Pitching and Rolling Oscillation Case III;
 $\alpha = 20.0^\circ + 4.0^\circ \sin(\pi t)$, $\theta = 4.0^\circ \sin(2\pi t)$

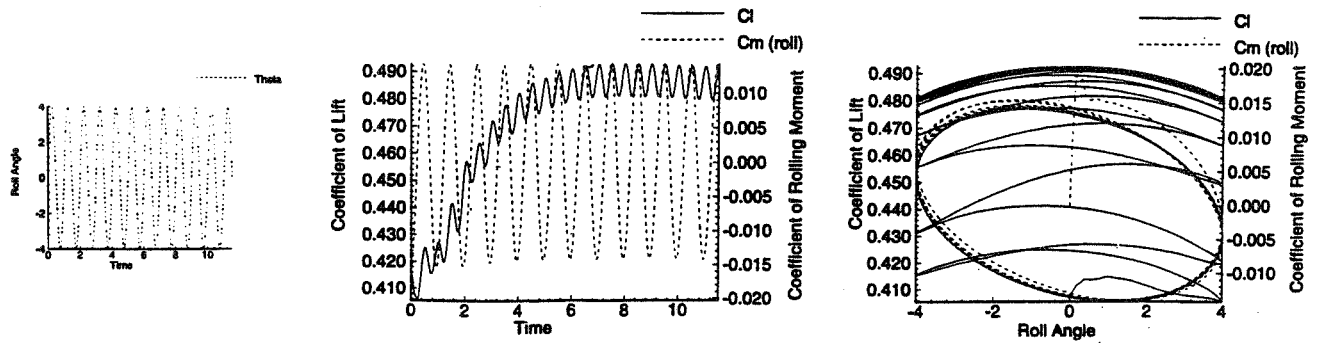
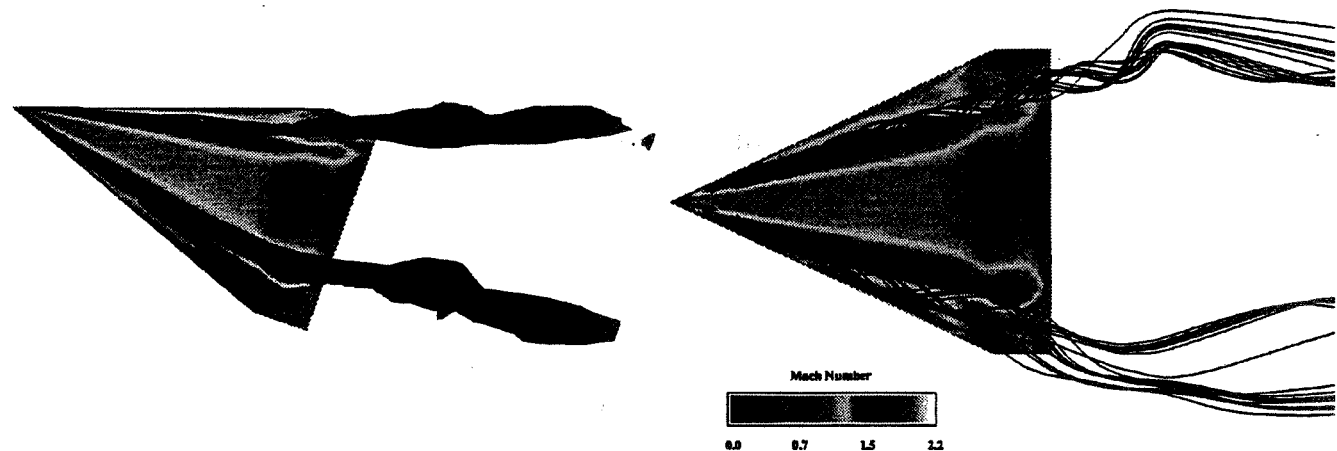
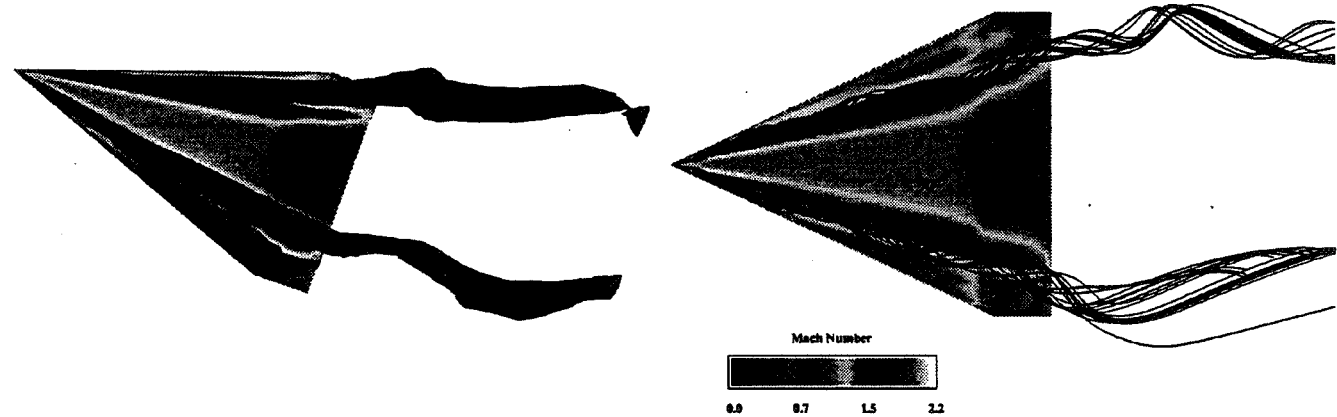


Figure 9. Aerodynamic Response, Forced Rolling-alone Oscillation Case II; $\alpha = 20.0^\circ$, $\theta = 4.0^\circ \sin(2\pi t)$



a) $\alpha = 20.0^\circ$, $\theta = 0.0^\circ$ (maximum pitch up velocity and maximum positive roll velocity)



b) $\alpha = 20.0^\circ$, $\theta = 0.0^\circ$ (forced rolling alone, maximum positive roll velocity)

Figure 10. Comparison of the Mach Contours near the Wing Surface with Surfaces of Constant Entropy ($s = 0.5$) and Instantaneous Streamlines of a) Forced Coupled Pitching and Rolling Oscillation Case III at $t = 10.0$, and b) Forced Rolling-alone Oscillation Case II at $t = 7.5$.

Forced Coupled Pitching and Rolling Oscillation Case IV

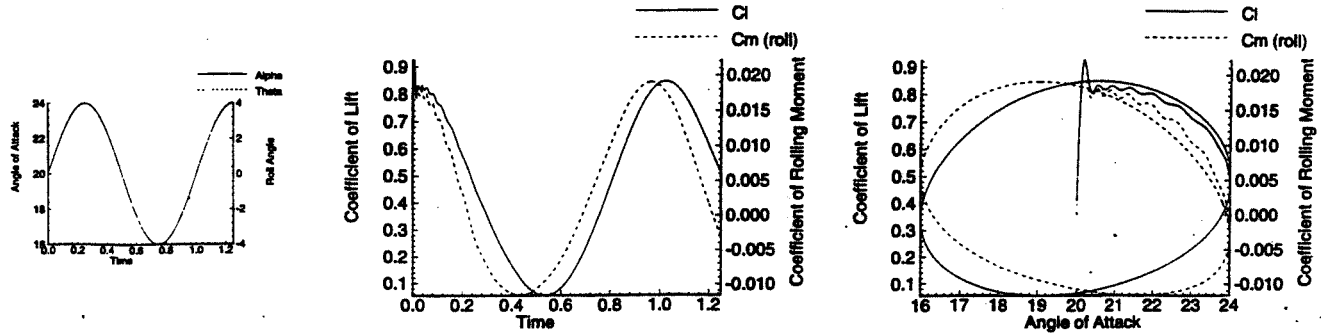


Figure 11. Aerodynamic Response, Forced Coupled Pitching and Rolling Oscillation Case IV;
 $\alpha = 20.0^\circ + 4.0^\circ \sin(2\pi t)$, $\theta = 4.0^\circ \sin(2\pi t)$

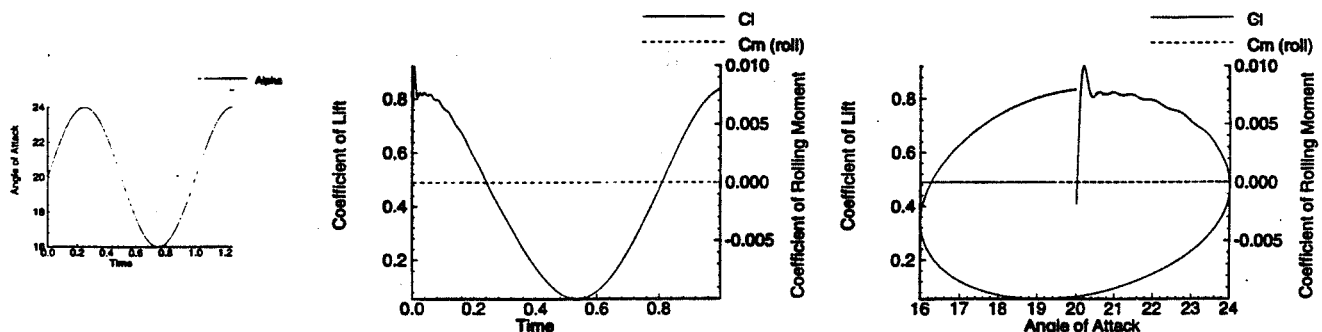


Figure 12. Aerodynamic Response, Forced Pitching-alone Oscillation Case II; $\alpha = 20.0^\circ + 4.0^\circ \sin(2\pi t)$, $\theta = 0.0^\circ$

**Effects of Coupled Rolling and Pitching Oscillations
on Transonic Shock-Induced Vortex-Breakdown Flow
of a Delta Wing**

**Osama A. Kandil and Margaret A. Menzies
Aerospace Engineering Department
Old Dominion University, Norfolk, VA 23529**

**Sixth International Symposium
On Computational Fluid Dynamics**

**September 4-8, 1995
Lake Tahoe, NV, USA**

52-02
2/27/88

Effects of Coupled Rolling and Pitching Oscillations on Transonic Shock-Induced Vortex-Breakdown Flow of a Delta Wing

Osama A. Kandil* and Margaret A. Menzies*

* Aerospace Engineering Department
Old Dominion University, Norfolk, VA 23529

ABSTRACT

Unsteady, transonic vortex-breakdown flow over a 65° sharp edged, cropped-delta wing of zero thickness undergoing forced coupled pitching and rolling oscillations is investigated computationally. The initial condition of the flow is characterized by a transverse terminating shock which induces of the leading edge vortex cores to breakdown. The computational investigation uses the time-accurate solution of the laminar, unsteady, compressible, full Navier-Stokes equations with the implicit, upwind, Roe flux-difference splitting, finite-volume scheme. The main focus is to analyze the effects of coupled motion on the wing response and vortex-breakdown flow by varying oscillation frequency and phase angle while keeping the maximum pitch and roll amplitude equal.

INTRODUCTION

Various computational and experimental investigations have been conducting using single mode oscillations of a delta wing for low speed and supersonic flows.¹⁻³ These studies emphasize analysis of the flow response for improving the stability, control and maneuvering capability of defense fighters. However, most fighters when super maneuvering operate in the transonic regime which necessitates experimental and computational simulations which use the full Navier-Stokes equations, for single and coupled mode responses. Recent experimental measurements of transonic flows around 65° cropped delta wing⁴⁻⁶ show that a complex shock-wave system appears over the upper wing surface which consists of a ray shock wave beneath the leading-edge primary vortex and a transverse, time dependent, normal-shock wave (known as a terminating shock) which induces breakdown of the primary vortices.

Kandil, Kandil, and Liu,⁷⁻⁸ used laminar, unsteady, compressible, full Navier-Stokes equations which were integrated time accurately to study and construct the flow field structure of transonic flow around a 65° sharp-edged, cropped-delta wing at 20° angle of attack, 0.85 Mach number and 3.23×10^6 Reynolds number. The complex shock system was captured and the results have been validated using available experimental data with good agreement. In Refs. 9 and 10, transonic flow over the delta wing undergoing single

mode oscillations of pitching and rolling respectively was examined and the response of the vortex-breakdown as a results of the motion analyzed. In this paper, investigation of the aerodynamic response of the wing and the vortex-breakdown due to coupled mode oscillations is presented and compared to the single mode responses. In this analysis, the phase shift and reduced frequency is varied in order to gain comprehensive understanding of the influence of coupling the motion.

HIGHLIGHTS OF FORMULATION AND COMPUTATIONAL SCHEME

The complete formulation of the conservative form of the dimensionless, unsteady, compressible, full Navier-Stokes equations in terms of the time-dependent, body-conformed coordinates ξ^1 , ξ^2 , and ξ^3 , is given in Ref. 9. All boundary conditions are explicitly implemented and details of the computational scheme are described in Ref. 10. Since the wing is undergoing coupled motion, the grid is moved with the same angular motion as that of the body. The grid speed, $\frac{\partial \xi^m}{\partial t}$, and the metric coefficient, $\frac{\partial \xi^m}{\partial x_n}$, are computed at each time step of the computational scheme. Consequently, the kinematical boundary conditions at the inflow-outflow boundaries and at the wing surface are expressed in terms of the relative velocities.

The method of solution consists of two steps. In the first step, the problem is solved for the stationary wing at 20° angle of attack and a 0° roll angle. This solution represents the initial conditions for the second step. In the second step, the wing pitching and rolling functions are specified and the Navier-Stokes equations are solved accurately in time. At each time step, the wing and the grid are rotated through angles corresponding to the wing pitching and rolling angle. The metric coefficients and the grid speed are computed and the Roe flux-differencing scheme is used to obtain the solution.

COMPUTATIONAL RESULTS AND DISCUSSION

A 65° swept-back, sharp edged, cropped delta wing of zero thickness is considered for the computational solutions. The cropping ratio (tip length/root-chord length) is 0.15. An O-H grid of $65 \times 43 \times 84$ in the wrap-around, normal, and axial directions, respectively, is used. The computational domain extends two-chord lengths forward and five-chord lengths backward from the wing trailing edge and has a radius of four-chord lengths. The initial conditions correspond to the flow solution around a stationary wing at an angle of attack of 20° and 0° roll angle, that was impulsively injected into a free stream with $M_\infty = 0.85$, and Reynolds number of 3.23×10^6 . The solution after 18,000 time steps at a $\Delta t = 0.0002$ (corresponding to a total dimensionless time of 3.6) is then used for the starting point of all subsequent cases. This solution is characterized by weak oblique shocks beneath the primary vortices and a transverse, strong, terminating shock which causes the primary vortices to breakdown showing attracting and repelling spiral saddle critical points which indicate vortex breakdown.

Case I-Coupled Pitch And Roll, In Phase Motion:

From the initial conditions, the wing is forced to oscillate in pitch around an axis located at the quarter-chord length and in roll around the axis of geometric symmetry. The amplitude of both the pitching, (α_a), and rolling, (θ_a), oscillation is 4.0° and the reduced frequency, (k), is 1π . The motion starts with the angle of attack increasing while simultaneously rolling with the left-hand side of the wing (looking in the upstream direction) rolling downward. The case was run for 5.5 cycles. Figures 1, 2 and 3, compare the lift and rolling moment coefficient curves of the coupled in phase pitching and rolling case with the coefficient curves of the pitching and rolling cases each studied separately. The lift coefficient curve of the coupled case is nearly identical to that of the pitching alone case while the rolling moment coefficient curve of the coupled case is nearly identical to the rolling alone case. This indicates that the coupling effect is negligible for in phase motion at a reduced frequency of 1π .

Case II-Coupled Pitch And Roll, Out of Phase Motion:

Restarting from the same initial condition as in case I, the wing is again forced to oscillate in pitch and roll with the same amplitude, ($\alpha_a, \theta_a = 4.0^\circ$), and reduced frequency, ($k = 1\pi$), as in case I, however a 90° phase lead for the pitching motion was introduced. This case was run for more than 5 complete cycles of rolling. Figure 4 depicts the coefficient curves for the out of phase motion for comparison. With a 90° phase lead in the pitching motion, the lift coefficient curve is again nearly identical to that of pitching alone but the rolling moment coefficient curve decreases with each cycle. With a phase lead the breakdown of the vortices appears to strengthen as a result of coupling the motion and leads to a negative bias in the rolling moment curve.

Case III-Coupled Pitch And Roll, Different Frequencies:

From the initial condition, the wing is forced to oscillate with the same pitch and roll amplitude, ($\alpha_a, \theta_a = 4.0^\circ$), however, the reduced frequency, (k), for the rolling oscillation is 2π , or twice the pitching motion. This case was run for 9.5 cycles of rolling. Figures 5 and 6, compare the aerodynamic response for the coupled case rolling at twice the frequency of the pitching motion and the rolling alone case with a reduced frequency of 2π . As in the rolling alone case, this coupled case experiences an increase in the lift but a periodic response was achieved before the vortex breakdown is eliminated from the wing surface. The rolling moment curve appears unaffected by the pitching motion. The coupling effect incorporates the relieving effect of the rolling motion by weakening the vortices, but the pitching motion prevents the breakdown from washing downstream.

Case IV-Coupled Pitch And Roll, 2π Frequency:

This case was run for 1.25 cycles with the reduced frequency, (k), for both the pitching and rolling oscillation equal to 2π . This case required a reduction in time step and due to

computational limitations was run for only one and a quarter cycles. Figures 7 and 8 compare the response for the coupled in phase case with the pitching alone case with a reduced frequency of 2π . As in case I, each response is nearly identical to the single mode cases which indicates that there is no coupling effect for in phase motion.

CONCLUSIONS:

The unsteady, compressible, full Navier-Stokes equations are integrated time accurately using the implicit, upwind, flux-difference splitting, finite-volume scheme to study the effects of frequencies and phase angle of forced oscillations on the unsteady transonic vortex-breakdown flow around a 65° sharp-edged, cropped delta wing. The wing is first forced to oscillate in pitch and roll with a maximum pitch amplitude, α_a , and roll amplitude, θ_a , of 4.0° and a reduced frequency, k , of 1π . The second case demonstrated the effect of a 90° pitching phase lead while maintaining the same amplitudes and reduced frequency. In the third and fourth case, the reduced frequency for the rolling motion and both rolling and pitching motion respectively is increased. Using the computational applications described, it has been shown that a phase shift or frequency difference between the pitching and rolling motions have substantial effects on the aerodynamic responses of the wing and the vortex-breakdown flow.

ACKNOWLEDGMENT

This work is supported by the NASA-Langley Research Center under grant No. NAG-1-648 along with partial support from the AFOSR and the Virginia Space Grant Consortium. The computational resources provided by the NAS Center at AMES and the NASA Langley Research Center are acknowledged and appreciated.

REFERENCES

- ¹Kandil, O. and Chuang, H., AIAA-88-0371-CP, January, 1988.
- ²Chaderjian, N., AIAA-92-4428-CP, August, 1992.
- ³Gordnier, R. and Visbal, M., AIAA-93-0554-CP, January, 1993.
- ⁴Boersen, S. and Elsenaar, A., Proceedings of Symposium on International Vortex Flow Experiment on Euler Code Validation, Stockholm, Sweden, October 1-3, 1986.
- ⁵Bannik, W. and Houtman, E., Proceedings of Symposium on International Vortex Flow Experiment on Euler Code Validation, Stockholm, Sweden, October 1-3, 1986.
- ⁶Erickson, G., NASA Technical paper 3114, November 1991.
- ⁷Kandil, O., Kandil, H., and Liu, C., AIAA-93-2973-CP, July 6-9, 1993.
- ⁸Kandil, H., Kandil, O., and Liu, C., AIAA-93-3472-CP, August 9-11, 1993.
- ⁹Kandil, O. and Kandil, H., AIAA-94-1426-CP, April 18-20, 1994.
- ¹⁰Menzies, M., Kandil, O., and Kandil, H., AIAA-95-1771-CP, June 19-22, 1995.

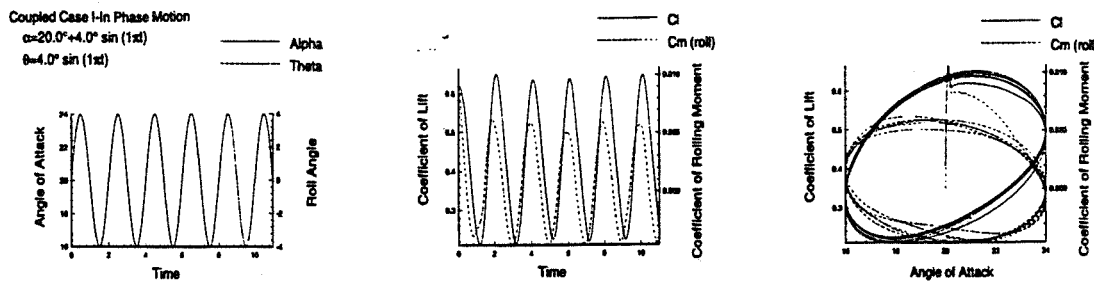


Figure 1. Coupled Case I-In Phase Motion. Angle of attack and roll angle plotted versus time and aerodynamic properties plotted versus time and angle of attack.

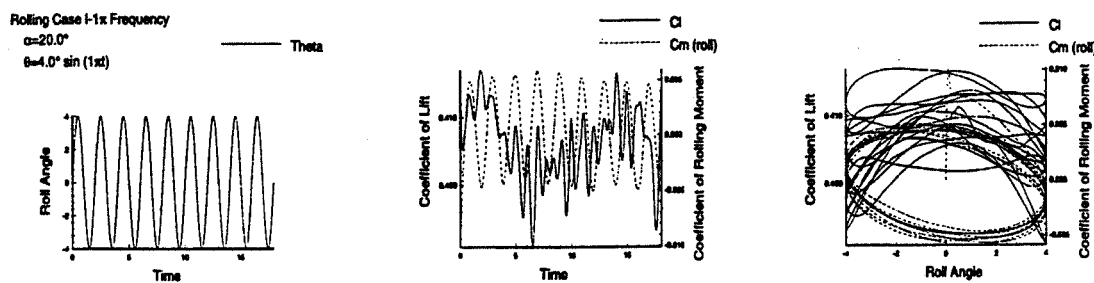


Figure 2. Rolling Case I-1 π Frequency. Roll angle plotted versus time and aerodynamic properties plotted versus time and roll angle.

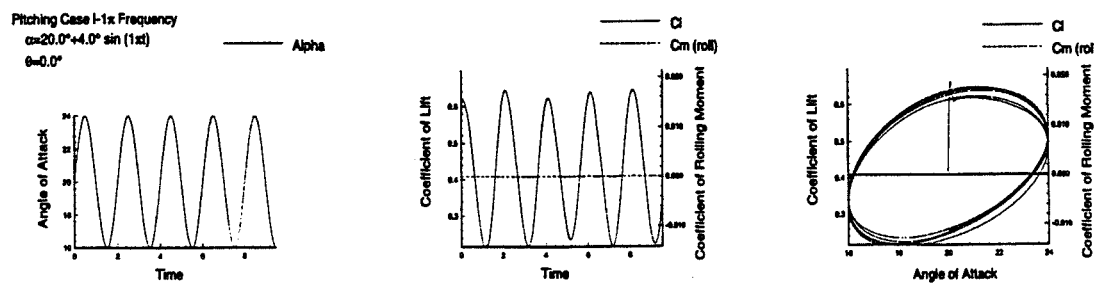


Figure 3. Pitching Case I-1 π Frequency. Angle of attack plotted versus time and aerodynamic properties plotted versus time and angle of attack.

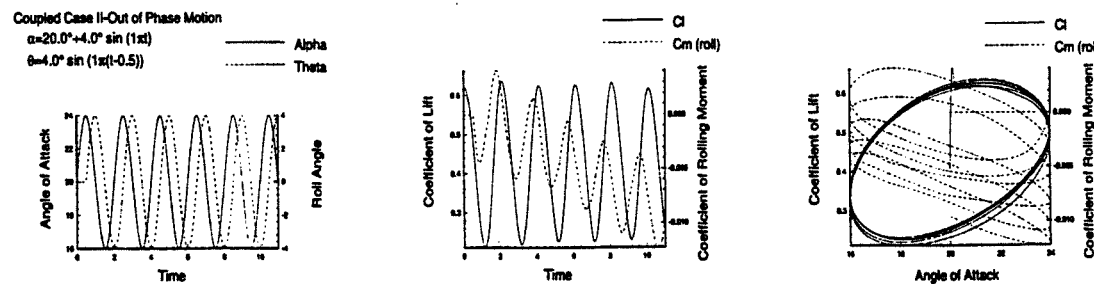


Figure 4. Coupled Case II-Out of Phase Motion. Angle of attack and roll angle plotted versus time and aerodynamic properties plotted versus time and angle of attack.

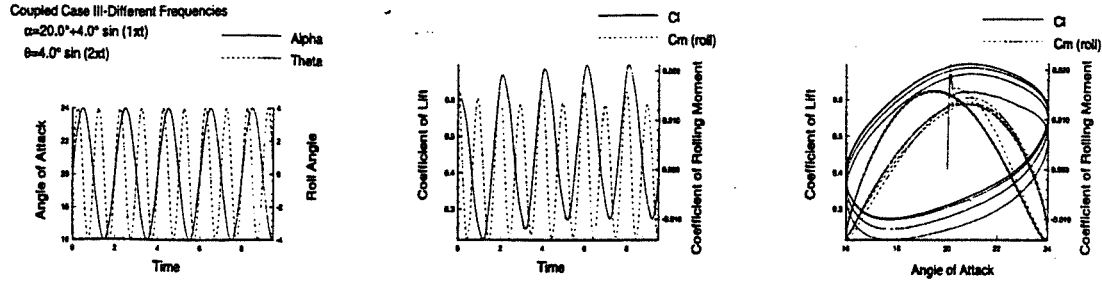


Figure 5. Coupled Case III-Different Frequencies. Angle of attack and roll angle plotted versus time and aerodynamic properties plotted versus time and angle of attack.

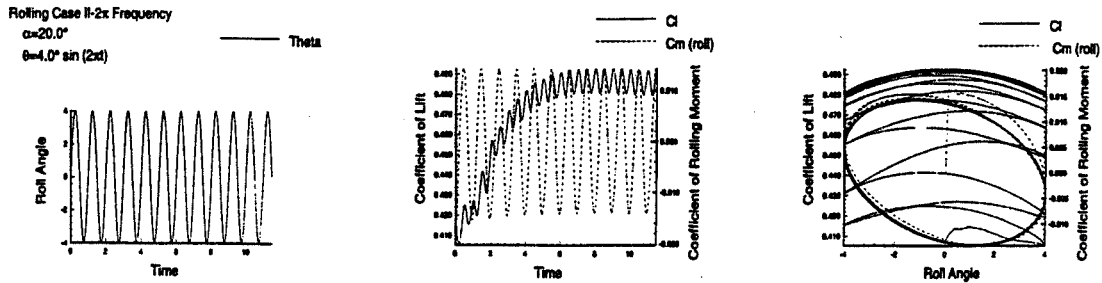


Figure 6. Rolling Case II- 2π Frequency. Roll angle plotted versus time and aerodynamic properties plotted versus time and roll angle.

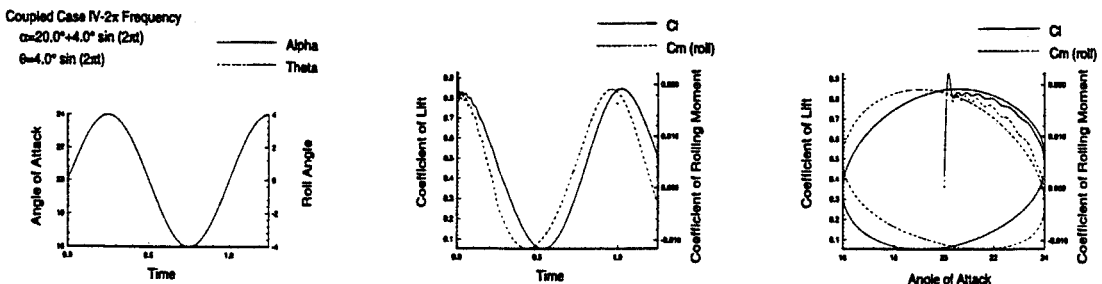


Figure 7. Coupled Case IV- 2π Frequency. Angle of attack and roll angle plotted versus time and aerodynamic properties plotted versus time and angle of attack.

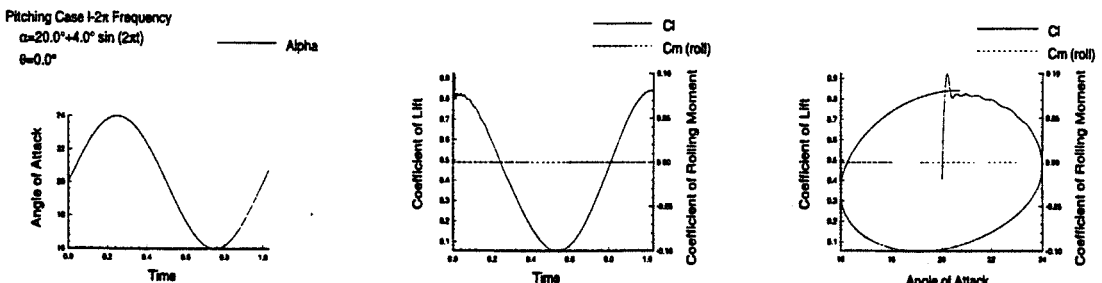


Figure 8. Pitching Case II- 2π Frequency. Angle of attack plotted versus time and aerodynamic properties plotted versus time and angle of attack.

53-02
38277

RAS PAPER No 16.52

**STRUCTURAL DYNAMIC/CFD INTERACTION
FOR COMPUTATION OF VERTICAL TAIL BUFFET**

**Osama A. Kandil, Steven J. Massey and
Essam F. Sheta**

**Old Dominion University
Norfolk, VA 23529, USA**

**The Royal Aeronautical Society
International Forum on Aeroelasticity and
Structural Dynamics 1995
Manchester, UK, June 26–28, 1995**

STRUCTURAL DYNAMICS/CFD INTERACTION FOR COMPUTATION OF VERTICAL TAIL BUFFET

Osama A. Kandil*, Steven J. Massey[†] and Essam F. Sheta[‡]

Aerospace Engineering Department

Old Dominion University, Norfolk, VA 23529-0247

Abstract

The multi-disciplinary problem of tail buffeting is solved using three sets of equations. The first set is the unsteady, compressible, full Navier-Stokes equations which are used for obtaining the flow-field vector and the aerodynamic loads. The second set is the coupled aeroelastic equations which are used for obtaining the bending and torsional deflections of the tail. The third set is the grid-displacement equations which are used for updating the grid coordinates due to the tail deflections. For the computational applications a sharp-edged delta wing of aspect ratio one and a rectangular vertical tail of aspect ratio one placed in the plane of geometric symmetry behind the wing are considered. The configuration is pitched at a critical angle of attack ($\alpha = 38^\circ$) which produces asymmetric, vortex-breakdown flow of the delta wing primary vortices. The results show the effects of coupled and uncoupled bending-torsional responses and the effects of the Reynolds number.

Nomenclature

C_p	Pressure coefficient
\bar{E}_m	Inviscid flux vector
\bar{E}_v	Viscous flux vector
EI	Bending stiffness of the tail section
GJ	Torsional stiffness of the tail section
\hat{I}	Number of bending modes
I_θ	Mass-moment of inertia per unit length about the elastic axis
K_{ij}	Stiffness matrix element
l_t	Tail length
m	Tail mass per unit length
M	Number of banding and torsion modes

M_{ij}	Mass matrix element
M_t	Twisting moment per unit length
N	Normal force per unit length
q	Generalized coordinate
\bar{Q}	Fluid flow vector
w	Bending deflection
x,y,z	Cartesian coordinates in the axial, spanwise and normal directions
x_θ	Distance between the elastic axis and inertia axis
θ	Twist angle
ϕ	Comparison function

Introduction

The ability of modern fighter aircraft to fly and maneuver at high angles of attack and at high loading conditions is of prime importance. This capability is achieved, for example in the F/A-18 fighter, through the combination of the leading-edge extension (LEX) with a delta wing and the use of vertical tails. The LEX maintains lift at high angles of attack by generating a pair of vortices that trail aft over the top of the aircraft. The vortex entrains air over the vertical tails to maintain stability of the aircraft. This combination of LEX, delta wing and vertical tails leads to the aircraft excellent high angle of attack performance. However, at some flight conditions, the vortices emanating from the highly-swept LEX of the delta wing breakdown before reaching the vertical tails which get bathed in a wake of unsteady highly-turbulent, swirling flow. The vortex-breakdown flow produces unsteady, unbalanced loads on the vertical tails which in turn produce severe buffet on the tails and has led to their premature fatigue failure.

*Professor, Eminent Scholar and Department Chairman.

[†]Ph.D. Student and Research Assistant.

[‡]Ph.D. Student and Research Assistant.

Experimental investigation of the vertical tail buffet of the F/A-18 models have been conducted by several investigators such as Sellers et al. (Ref 1), Erickson et al. (Ref 2), Wentz (Ref 3) and Lee and Brown (Ref 4). These experiments showed that the vortex produced by the LEX of the wing breaks down ahead of the vertical tails at angles of attack of 25° and higher and the breakdown flow produced unsteady loads on the vertical tails. Rao, Puram and Shah (Ref 5) proposed two aerodynamic concepts for alleviating high-alpha tail buffet characteristics of the twin tail fighter configurations. Cole, Moss and Doggett (Ref 6) tested a rigid, 1/6 size, full-span model of an F-18 airplane that was fitted with flexible vertical tails of two different stiffness. Vertical-tail buffet response results were obtained over the range of angle of attack from -10° to $+40^\circ$, and over the range of Mach numbers from 0.3 to 0.95. Their results indicated that the buffet response occurs in the first bending mode, increases with increasing dynamic pressure and is larger at $M = 0.3$ than that at a higher Mach number.

An extensive experimental investigation has been conducted to study vortex-fin interaction on a 76° sharp-edged delta wing with vertical twin-fin configuration by Washburn, Jenkins and Ferman (Ref 7). The vertical tails were placed at nine locations behind the wing. The experimental data showed that the aerodynamic loads are more sensitive to the chordwise tail location than its spanwise location. As the tails were moved toward the vortex core, the buffeting response and excitation were reduced. Although the tail location did not affect the vortex core trajectories, it affected the location of vortex-core breakdown. Moreover, the investigation showed that the presence of a flexible tail can affect the unsteady pressures on the rigid tail on the opposite side of the model. In a recent study by Bean and Lee (Ref 8) tests were performed on a rigid 6% scale F/A-18 in a trisonic blowdown wind tunnel over a range of angle of attack and Mach number. The flight data was reduced to a non-dimensional buffet excitation parameter, for each primary mode. It was found that buffeting in the torsional mode occurred at a lower angle of attack and at larger levels compared to the fundamental bending mode.

Kandil, Kandil and Massey (Ref 9) presented the first successful computational simulation of

the vertical tail buffet using a delta wing-vertical tail configuration. A 76° sharp-edged delta wing has been used along with a single rectangular vertical tail which was placed aft the wing along the plane of geometric symmetry. The tail was allowed to oscillate in bending modes. The flow conditions and wing angle of attack have been selected to produce an unsteady vortex-breakdown flow. The solution of this multidisciplinary problem was obtained using three set of equations (Navier-Stokes, aeroelastic and grid displacement equations) which were sequentially integrated with time-accurate stepping to obtain the flow field, aerodynamic loads, bending deflections and grid displacements. Unsteady vortex breakdown of leading-edge vortex cores was captured, and unsteady pressure forces were obtained on the tail. These computational results are in full qualitative agreement with the experimental data of Washburn, Jenkins and Ferman (Ref 7). An alternative simple model for simulation of the buffet problem was used by Kandil and Flanagan (Ref 10) and Flanagan (Ref 11). In this model, a configured circular duct was used to produce vortex-breakdown flow through the interaction of a supersonic swirling flow and a shock at the inlet of the duct. Downstream of the vortex-breakdown flow a cantilevered plate was placed. The problem was solved for the quasi-axisymmetric case.

Kandil, Kandil and Massey (Ref 12) extended the technique used in (Ref 9) to allow the vertical tail to oscillate in both bending and torsional modes. The total deflections and the frequencies of deflections and loads of the coupled bending-torsion case were found to be one order of magnitude higher than those of the bending case only. Also it has been shown that the tail oscillations change the vortex breakdown locations and the unsteady aerodynamic loads on the wing and tail.

In this paper, we address several issues related to the tail buffet response. First, we address the effects of coupling and uncoupling the bending and torsional modes within a long computational time. Second, we address the effect of the flow Reynolds number on the uncoupled bending-torsion response.

Formulation

The formulation of the problem consists of three sets of governing equations along with certain ini-

tial and boundary conditions. The first set is the unsteady, compressible, full Navier-Stokes equations. The second set consists of the aeroelastic equations for bending and torsional modes. The third set consists of equations for deforming the grid according to the tail deflections. The literature shows various methods to move the grid. The simplest method uses simple interpolation functions such that the grid points adjacent to the aeroelastic surface move with the surface while the grid points at the computational-region boundary do not move (Ref 13). The unsteady, linearized, Navier-displacement equations have also been used successfully by Kandil et al. to move the grid dynamically (Ref 14-15). In the present paper, we use simple grid interpolation to move the grid. Next, the governing equations for each set are given

Fluid-Flow Equations:

The conservative form of the dimensionless, unsteady, compressible, full Navier-Stokes equations in terms of time-dependent, body-conformed coordinates ξ^1 , ξ^2 and ξ^3 is given by

$$\frac{\partial \bar{Q}}{\partial t} + \frac{\partial \bar{E}_m}{\partial \xi^m} - \frac{\partial (\bar{E}_v)_s}{\partial \xi^s} = 0; m = 1-3, s = 1-3 \quad (1)$$

where

$$\xi^m = \xi^m(x_1, x_2, x_3, t) \quad (2)$$

$$\bar{Q} = \frac{1}{J} [\rho, \rho u_1, \rho u_2, \rho u_3, \rho e]^t, \quad (3)$$

\bar{E}_m and $(\bar{E}_v)_s$ are the ξ^m -inviscid flux and ξ^s -viscous and heat conduction flux, respectively. Details of these fluxes are given in (Ref 9).

Aeroelastic Equations:

The dimensionless, linearized governing equations for the coupled bending and torsional vibrations of a vertical tail that is treated as a cantilevered beam are considered. The tail bending and torsional deflections occur about an elastic axis that is displaced from the inertial axis. These equations for the bending deflections, w , and the twist angle, θ , are given by

$$\begin{aligned} & \frac{\partial^2}{\partial z^2} \left[EI(z) \frac{\partial^2 w}{\partial z^2}(z, t) \right] + m(z) \frac{\partial^2 w}{\partial t^2}(z, t) \\ & + m(z) x_\theta(z) \frac{\partial^2 \theta}{\partial t^2}(z, t) = N(z, t) \end{aligned} \quad (4)$$

$$\begin{aligned} & \frac{\partial}{\partial z} \left[GJ(z) \frac{\partial \theta}{\partial z} \right] - m(z) x_\theta \frac{\partial^2 w}{\partial t^2}(z, t) \\ & - I_\theta(z) \frac{\partial^2 \theta}{\partial t^2}(z, t) = -M_t(z, t) \end{aligned} \quad (5)$$

where z is the vertical distance from the fixed support along the tail length. The characteristic parameters for the dimensionless equations are c^* , a_∞^* , ρ_∞^* and c^*/a_∞^* for the length, speed, density and time; where c^* is the delta wing root-chord length, a_∞^* the freestream speed of sound and ρ_∞^* the freestream air density. The geometrical and natural boundary conditions on w and θ are given by

$$\begin{aligned} w(0, t) &= \frac{\partial w}{\partial z}(0, t) = \frac{\partial^2 w}{\partial z^2}(l_t, t) \\ &= \frac{\partial}{\partial z} \left[EI(l_t) \frac{\partial^2 w}{\partial z^2}(l_t, t) \right] = 0 \end{aligned} \quad (6)$$

$$\theta(0, t) = \frac{\partial \theta}{\partial z}(l_t, t) = 0 \quad (7)$$

The solution of Eqs. (4) and (5) are given by

$$w(z, t) = \sum_{i=1}^{\hat{I}} \phi_i(z) q_i(t) \quad (8)$$

$$\theta(z, t) = \sum_{j=\hat{I}+1}^M \phi_j(z) q_j(t) \quad (9)$$

where ϕ_i and ϕ_j are comparison functions satisfying the free-vibration modes of bending and torsion, respectively, and q_i and q_j are generalized coordinates for bending and torsion, respectively. Substituting Eqs. (8) and (9) into Eqs. (4) and (5) and using the Galerkin method along with integration by parts and the boundary conditions, Eqs (6) and (7), we get the following equation for the generalized coordinates q_i and q_j in matrix form:

$$\begin{bmatrix} M_{11} & M_{12} \\ M_{21} & M_{22} \end{bmatrix} \begin{pmatrix} \ddot{q}_i \\ \ddot{q}_j \end{pmatrix} + \begin{bmatrix} K_{11} & 0 \\ 0 & K_{22} \end{bmatrix} \begin{pmatrix} q_i \\ q_j \end{pmatrix} = \begin{pmatrix} \hat{N}_1 \\ \hat{N}_2 \end{pmatrix}; i = 1, 2, \dots, \hat{I}; j = \hat{I} + 1, \dots, M \quad (10)$$

where

$$\begin{aligned} M_{11} &= \int_0^{l_t} m \phi_r \phi_i dz \\ M_{12} &= M_{21} = \int_0^{l_t} m x_\theta \phi_r \phi_j dz \\ M_{22} &= \int_0^{l_t} I_\theta \phi_s \phi_j dz \end{aligned} \quad \left. \right\} \quad (11)$$

$$\left. \begin{array}{l} K_{11} = \int_0^{l_t} EI \frac{d^2\phi_r}{dz^2} \frac{d^2\phi_i}{dz^2} dz \\ K_{22} = \int_0^{l_t} GJ \frac{d\phi_s}{dz} \frac{d\phi_i}{dz} dz \end{array} \right\} \quad (12)$$

$$\left. \begin{array}{l} \hat{N}_1 = \int_0^{l_t} \phi_r N dz \\ \hat{N}_2 = \int_0^{l_t} \phi_s M_t dz \end{array} \right\} \quad (13)$$

Similar aeroelastic equations were developed for sonic analysis of wing flutter by Strganac (Ref 16), and Strganac, Mook and Mitchum (Ref 17). The numerical integration of Eqs. (11-13) is obtained using the trapezoidal method with 125 points to improve the accuracy of integrations. The solution of Eq. (10), for $q_i; i = 1, 2, \dots, \hat{I}$, and $q_j; j = \hat{I} + 1, \dots, M$, is obtained using the Runge-Kutta scheme. Next, w , and θ are obtained from Eqs. (8) and (9). In this paper, the number of bending modes, \hat{I} , is six and the number of torsion modes, $M - \hat{I}$, is also six.

Grid Displacement Equations:

Once w and θ are obtained at the $n+1$ time step, the new grid coordinates are obtained using simple interpolation equations. In these equations, the tail bending displacement, $w_{i,j,k}^{n+1}$, and the tail displacement through the torsion angle, $\theta_{i,j,k}^{n+1}$ are interpolated through a cosine function. These equations for the y and z coordinates to the right side of the tail and a head of its elastic axis are given by

$$y_{i,j,k}^{n+1} = y_{i,j,k}^n + [w_{i,j,k}^{n+1} + (X - x_{i,j,k}^n) \tan \theta_{i,j,k}^{n+1}] \cos \left(\frac{y_{i,j,k}^n \pi}{Y/2} \right) \quad (14)$$

$$z_{i,j,k}^{n+1} = z_{i,j,k}^n - [\Delta z^o - \sqrt{(\Delta z^o)^2 - (\Delta w^{n+1})^2}] \cos \left(\frac{z_{i,j,k}^n \pi}{Z/2} \right) \quad (15)$$

where $z_{i,j,k}^{n+1}$ and $y_{i,j,k}^{n+1}$ are the z and y coordinates of a grid point at the $n+1$ time step, $z_{i,j,k}^o$ is the original z coordinate of a tail grid point and $\Delta z_{i,j,k}^o = z_{i,j,k}^o - z_{i,j,k-1}^o$, Y is the maximum y coordinate from the tail-surface grid point to the corresponding point at the right boundary of the computational domain, Z is the maximum z coordinate from the tail root to the upper boundary of the computational domain and X is the x coordinate of the tail elastic axis. These equations result in displacing a grid point on the tail by the total deflection due to bending and torsion and keeping a grid point at the boundary fixed.

Similar equations are used for the other part of the computational domain.

Boundary and Initial Conditions:

Boundary conditions consists of conditions for the fluid flow and conditions for the aeroelastic bending and torsional deflections of the tail. For the fluid flow, the Riemann-invariant boundary conditions are enforced at the inflow and outflow boundaries of the computational domain. At the plane of geometric symmetry, a periodic boundary conditions is specified with the exception of grid points on the tail. On the wing surface, the no-slip and no-penetration conditions are enforced and $\frac{\partial p}{\partial n} = 0$. On the tail surface, the no-slip and no-penetration conditions for the relative velocity components are enforced (points on the tail surface are moving). The normal pressure gradient is no longer equal to zero due to the acceleration of the grid points on the tail surface. This equation becomes $\frac{\partial p}{\partial n} = -\rho \bar{a}_t \cdot \hat{n}$, where \bar{a}_t is the acceleration of a point on the tail and \hat{n} is the unit normal.

Initial conditions consist of conditions for the fluid flow and conditions for the aeroelastic deflections of the tail. For the fluid flow, the initial conditions correspond to the freestream conditions with no-slip and no-penetration conditions on the wing and tail. For the aeroelastic deflections of the tail, the initial conditions for any point on the tail is that the displacement and velocity are zeros, $w(z, 0) = 0$, $\frac{\partial w}{\partial t}(z, 0) = 0$, $\theta(z, 0) = 0$ and $\frac{\partial \theta}{\partial t}(z, 0) = 0$.

Method of Solution

The first step is to solve for the fluid flow problem using the vortex-breakdown conditions and keeping the tail as a rigid beam. Navier-Stokes equations are solved using the implicit, flux-difference splitting finite-volume scheme. The grid speed $\frac{\partial \xi^m}{\partial t}$ is set equal to zero in this step. This step provides the flow field solution along with the pressure difference across the tail. The pressure difference is used to generate the normal force and twisting moment per unit length of the tail. Next, the aeroelastic equations are used to obtain the tail deflections, $w_{i,j,k}$ and $\theta_{i,j,k}$. The grid displacement equations are then used to compute the new grid coordinates. The metric coefficient of the coordinate Jacobian matrix are updated as well as the grid speed, $\frac{\partial \xi^m}{\partial t}$. This computational cycle is repeated every time step.

Computational Applications

Delta Wing-Vertical Tail Configuration:

The delta wing-vertical tail configuration consists of a sharp-edged, delta wing of aspect ratio 1, which is placed in the plane of geometric symmetry. The vertical tail leading edge is located at the wing trailing edge. The lower edge of the tail is along the wing axis and the tail is clamped at that edge. The wing angle of attack is 38° , the freestream Mach number is 0.4. The Reynolds number has been chosen as 10,000 and 1 million. An O-H grid of $65 \times 43 \times 84$ grid points in the wrap-around, normal and axial directions, respectively, is used for the solution of the fluid-flow part of the problem.

Initial Conditions (Fluid-Flow Problem), $R_e = 10^6$:

Keeping the tail rigid, the unsteady, compressible, full Navier-Stokes equations are integrated time accurately using the implicit, flux-difference splitting scheme of Roe with $\Delta t = 0.0022$. For the present case the Reynolds number is 1 million. Figure (1) shows a top view and a three dimensional view at the time step $t = 8,000$ for the wing-rigid tail configuration. The stagnation pressure distribution is shown on the wing surface. The figure also shows the critical points of vortex breakdown which is asymmetric. Looking in the upstream direction, it is observed that the starting location of vortex breakdown on the left side is ahead of that on the right side. The vortex breakdown was time dependent up to the present time step. The solution of the problem at the present time step is taken as the initial conditions for the next cases of the aeroelastic tail response.

Uncoupled Bending-Torsion Tail Response, $R_e = 10^6$:

The tail is treated as a rectangular beam with thickness $d = 0.005$, width $b = 0.5$ and height $l_t = 0.5$. The tail material dimensionless moduli of elasticity and rigidity, E and G are 1.8×10^5 and 0.692×10^5 , respectively. For the coupled bending-torsion case, the tail mass is assumed to vary in the x-direction resulting into distance between the elastic axis and inertia axis of $x_\theta = 0.05$ (inertia axis is downstream of the elastic axis). For the uncoupled bending-torsion case, no mass variation is assumed, hence, $x_\theta = 0$. The mass per unit length, m , is taken as 0.0653 and the

mass-moment of inertia per unit length around the elastic axis, I_θ , is 0.00153.

Figures (2)-(4) show the results of the uncoupled bending-torsion responses of the tail. In Fig (2), we show four pairs (left and right columns) of responses. The first pair is for the variation of the bending deflection, w , and torsional deflection, θ , along the tail height z every 1000 time step (curves A,B,...,L at $t = 8,000; 9,000; \dots; 18,000$). The bending and torsion responses are mainly of the first-mode shape type. The second pair of response shows the variation of the normal force and twisting moment along the tail height z every 1000 time step. The third and fourth pair show the bending deflection, normal force, torsional deflection and twisting moment variation at the tail tip and its midpoint versus the number of time steps ($n = 10,000$ or $t = 22$). It is observed that the frequency of the normal force is twice that of the bending deflection and the frequency of the twisting moment is almost the same as that of the torsional deflection. The bending and torsional deflections are slightly damped at advanced levels of time. Figure (3) shows the combined response, W_{net} , of the bending and torsional deflections along the tail height every 1000 time step. Figure (4) shows a top view and a three-dimensional view of the wing-deformed tail configuration at $n = 12,000$. Comparing Fig (4) with Fig (1) (Rigid tail at $n=8,000$), it is observed that the vortex breakdown location and shape are different. This conclusively shows the upstream aerodynamic effects of the tail bending and torsional deflections.

Coupled Bending-Torsion Tail Response, $R_e = 10^6$:

Figures (5)-(7) show the results of the coupled bending-torsion responses of the tail. These Figures are arranged in the same sequence as that of the previous case. Comparing the results of this case with those of the previous case, it is observed that both bending and torsional responses of the coupled case are substantially higher than those of the uncoupled case. Moreover, the frequencies of the bending deflection and the normal force are almost the same and those of the torsional deflection and the twisting moment are also the same. It is also observed that periodic response is achieved at advanced time levels. Figure (7) shows that the vortex breakdown locations and shape are different from those of the uncoupled case and the rigid tail case.

Uncoupled Bending-Torsion Tail Response, $R_e = 10^4$:

The flow Reynolds number is reduced to $R_e = 10^4$ within 2,000 time steps starting from the initial condition at $it = 8,000$ and keeping the tail rigid. Next, the problem is solved for uncoupled bending-torsion response with $\Delta t = 0.0011$. Figures (8)-(10) show the results of this case in the same sequence as those of Figures (2)-(4) of the uncoupled bending-torsion tail response with $R_e = 10^6$. Comparing Fig (8) with Fig (2), it is observed that the bending deflection of the case with $R_e = 10^4$ is substantially lower than that of the case with $R_e = 10^6$. However, the torsional deflection deflection is of the same order as that of the high Reynolds number case. Figure (9) shows that the net deflection of the tail is more than 50% less than that of the high Reynolds number case, Fig (3). Figure (10) shows that the breakdown locations and shape are substantially different from those of the high Reynolds number case. It is concluded that the low Reynolds number of the flow provides more aerodynamic damping to the structural response.

Concluding Remarks

The tail buffet problem due to the unsteady aerodynamic loads induced by the vortex-breakdown flow of the wing leading-edge vortices has been simulated computationally and efficiently using a delta wing-vertical tail configuration. The wing aspect ratio and flow conditions have been carefully selected in order to produce unsteady vortex-breakdown flow. The solution has demonstrated the development of the tail buffet due to the unsteady loads produced by the vortex-breakdown flow. The problem is a multidisciplinary problem which requires three sets of equations to obtain its solution.

In the present paper, the CFD solver is the implicit, upwind, Roe flux-difference splitting scheme. This scheme has the advantage of lower numerical dissipation than that of the Van Leer flux-vector splitting scheme, which was used in (Ref 12) by the first authors. Thus, the contribution of the numerical dissipation to the aerodynamic damping is decreased. Two issues have been addressed in this paper. First, the effects of coupling and uncoupling the bending and torsional modes are investigated. It has been found that the coupled bending-torsion response produce higher deflection than that of the uncoupled

response. Moreover, the response of the coupled case reaches periodicity faster than the uncoupled case. Second, the effect of the flow Reynolds number is investigated for the case of the uncoupled response. It has been shown that the deflections of the low Reynolds number case are substantially lower than those of the higher Reynolds number case. In addition, it has been shown for the three cases under consideration that the tail response has substantial effects on the vortex breakdown shape and locations on the wing, upstream of the tail.

Acknowledgment

This research work is supported under Grants No. NAG-1-648 and NAG-1-994 by the NASA Langley Research Center. The authors would like to recognize the computational resources provided by the NAS facilities at Ames Research Center and the NASA Langley Research Center.

References

1. Sellers, W. L. III, Meyers, J. F. and Hepner, T. E., "LDV Survey Over a Fighter Model at Moderate to High Angle of Attack," SAE Paper 88-1448, 1988.
2. Erickson, G. E., Hall, R. M., Banks, D. W., Del Frate, J. H., Shreiner, J. A., Hanley, R. J. and Pulley, C. T., "Experimental Investigation of the F/A-18 Vortex Flows at Subsonic Through Transonic Speeds," AIAA 89-2222, 1989.
3. Wentz, W. H., "Vortex-Fin Interaction on a Fighter Aircraft," AIAA 87-2474, AIAA Fifth Applied Aerodynamics Conference, Monterey, CA August 1987.
4. Lee, B. and Brown, D., "Wind Tunnel Studies of F/A-18 Tail Buffet," AIAA 90-1432, 1990.
5. Rao, D. M., Puram, C. K. and Shah, G. H., "Vortex Control for Tail Buffet Alleviation on a twin-Tail Fighter Configuration," SAE Paper No. 89-2221, 1989.
6. Cole, S. R., Moss, S. W. and Doggett, R. V., Jr., "Some Buffet Response Characteristics of a Twin-Vertical-Tail Configuration," NASA TM-102749, October 1990.

7. Washburn, A. E., Jenkins, L. N. and Ferman, M. A., "Experimental Investigation of Vortex-Fin Interaction," AIAA 93-0050, AIAA 31st ASM, Reno, NV, January 1993.
8. Bean, D. E. and Lee, B. H. K., "Correlation of Wind Tunnel and Flight Test Data for F/A-18 Vertical Tail Buffet," AIAA 94-1800-CP, 1994
9. Kandil, O. A., Kandil, H. A. and Massey, S. J., "Simulation of Tail Buffet Using Delta Wing-Vertical Tail Configuration," AIAA 93-3688-CP, AIAA Atmospheric Flight Mechanics Conference, Monterey, CA August 1993, pp. 566-577.
10. Kandil, O. A. and Flanagan, M. W., "Vertical Tail Buffet in Vortex Breakdown Flows," 5th International Symposium on Computational Fluid Dynamics, Sendai-Japan, August 1993.
11. Flanagan, M. W., "Simulation of Vertical Tail Buffet in Internal Vortex Breakdown Flows," M.S. Thesis, Aerospace Engineering Department, Old Dominion University, Norfolk, VA, December 1993.
12. Kandil, O. A., Massey, S. J., and Kandil, H. A., "Computations of Vortex-Breakdown Induced Tail Buffet Undergoing Bending and Torsional Vibrations," AIAA 94-1428-CP, AIAA/ASME/ASCE/ASC Structural, Structural Dynamics and Material Conference, SC April 1994, pp. 977-993.
13. Schuster, D., Vadyak, J. and Atta, E., "Static Aeroelastic Analysis of Fighter Aircraft Using a Three-Dimensional Navier-Stokes Algorithm," AIAA 90-0435, January 1990.
14. Kandil, O. A., Chuang, H. A. and Salman, A. A., "Unsteady Flow Computation of Oscillating Flexible Wings," AIAA 90-0937-CP, April 1990, pp. 1370-1381.
15. Kandil, O. A. and Salman, A. A., "Unsteady Vortex-Dominated Flow Around Wings with Oscillating Leading-Edge Flaps," AIAA 91-0435, January 1991.
16. Straganac, T. W., "A Numerical Model of Unsteady, Subsonic Aeroelastic Behavior," NASA Technical Memorandum 100487, December 1987.
17. Straganac, T. W., Mook, D. T. and Mitchum, M. W., "The Numerical Simulation of Subsonic Flutter," AIAA 87-1428, June 1987.

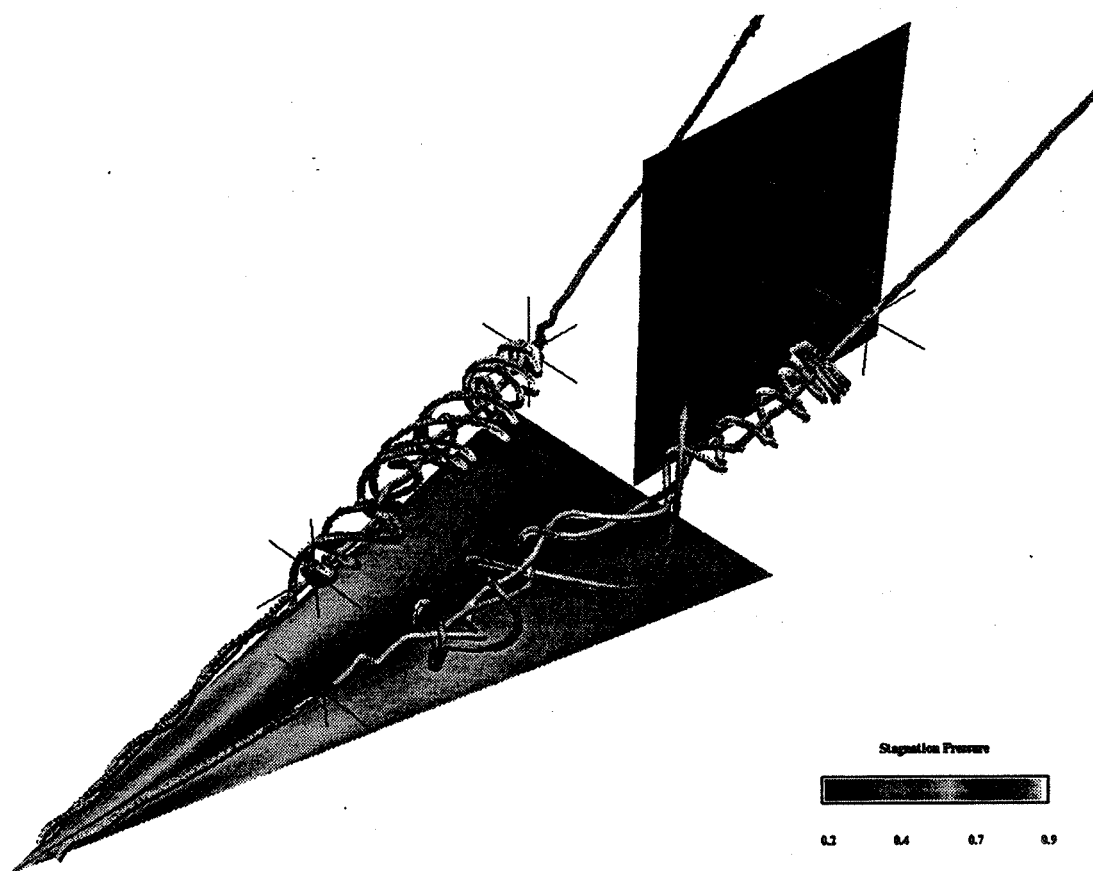
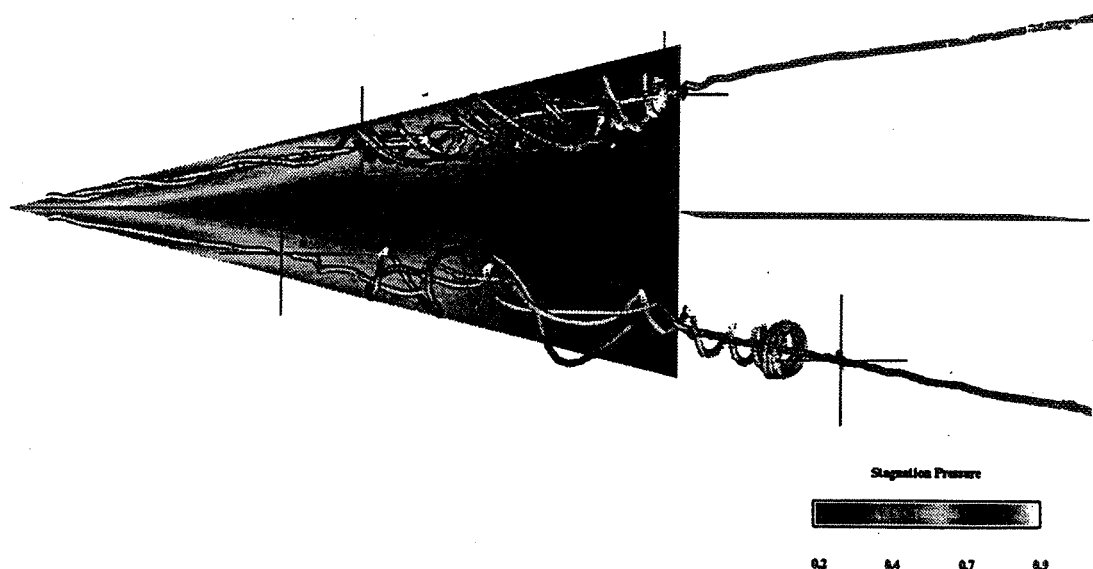


Fig (1) Top view and three-dimensional view of the wing-tail configuration for the initial conditions, $R_e = 10^6$, $\Delta t = 0.0022$, $it = 8,000$.

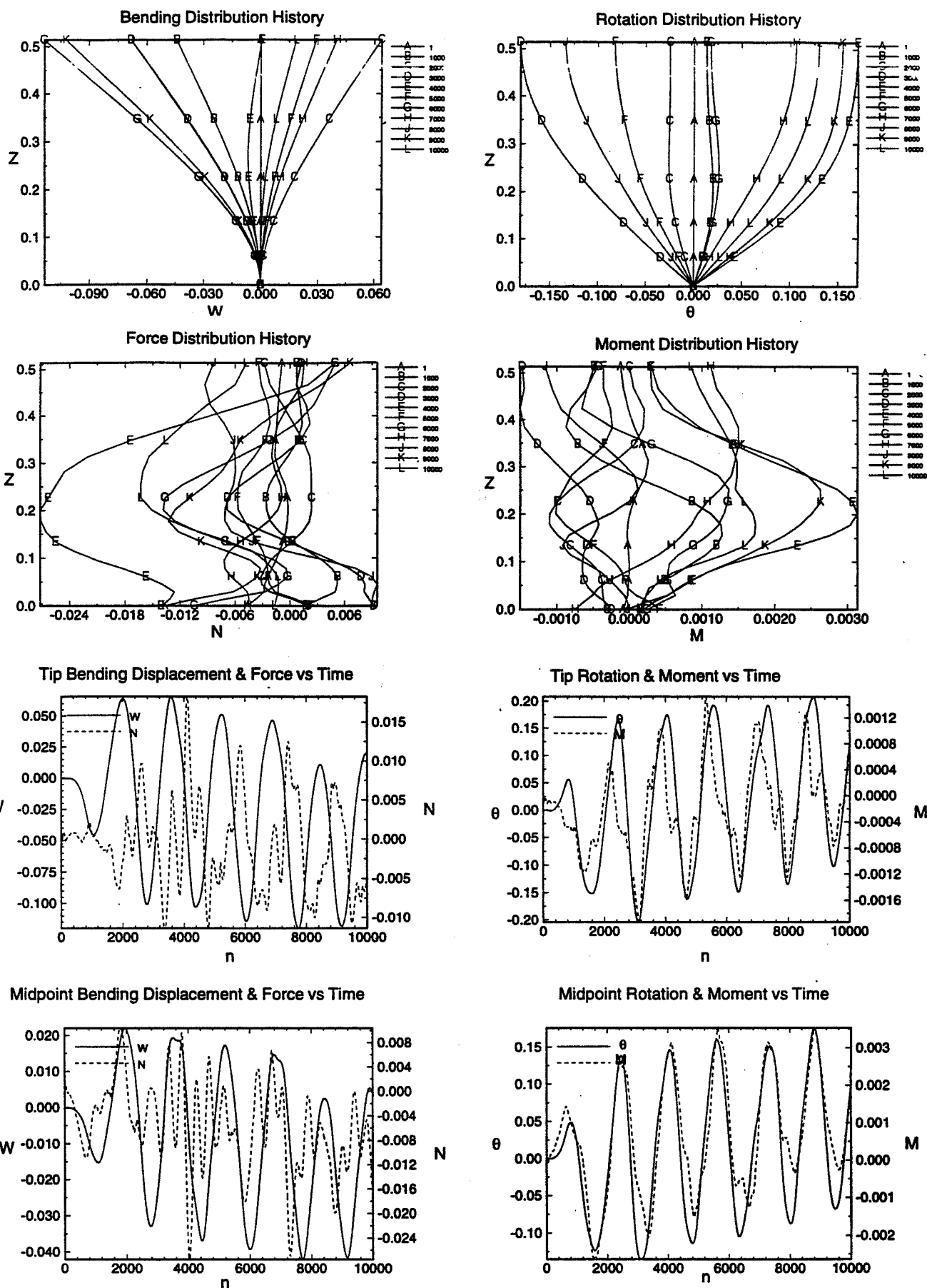


Fig (2) Deflection and load responses for the uncoupled bending-torsion case,
 $R_e = 10^6$, $\Delta t = 0.0022$, $it = 8,000 - 18,000$.

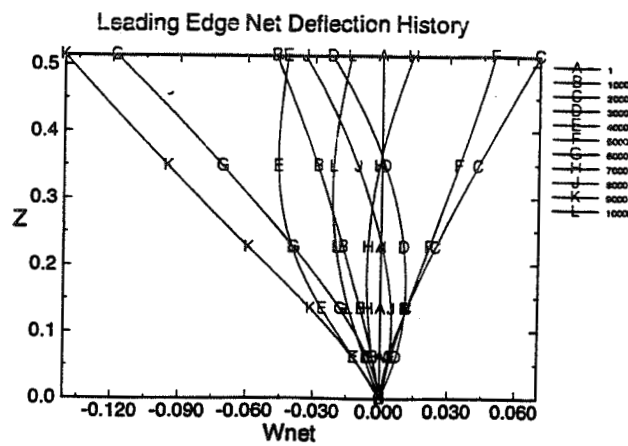


Fig (3) Net deflection of the tail leading edge for the uncoupled bending-torsion case, $R_e = 10^6$, $\Delta t = 0.0022$, $it = 8,000 - 18,000$.

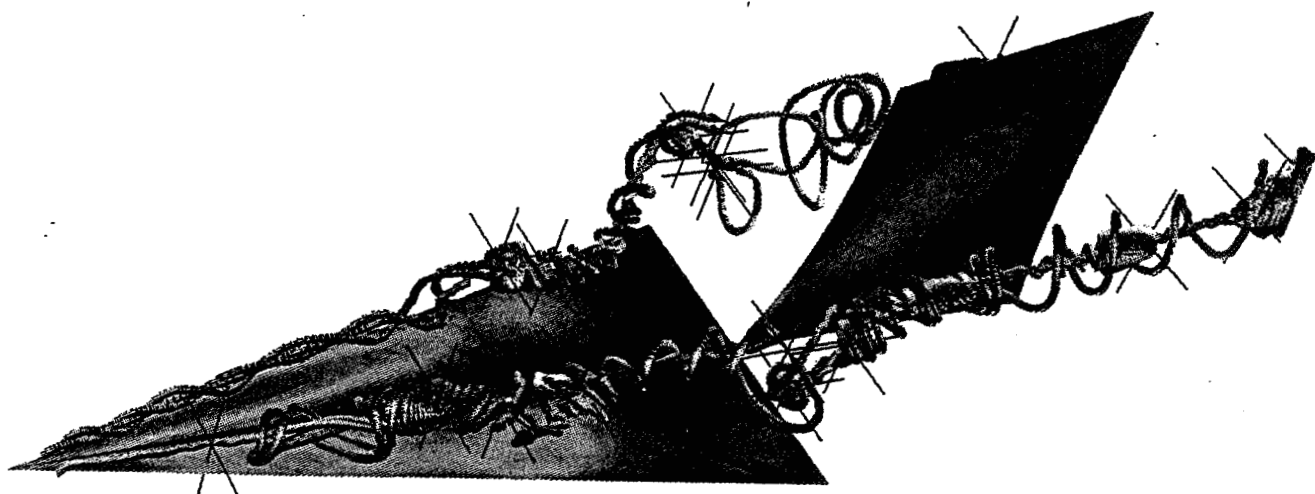
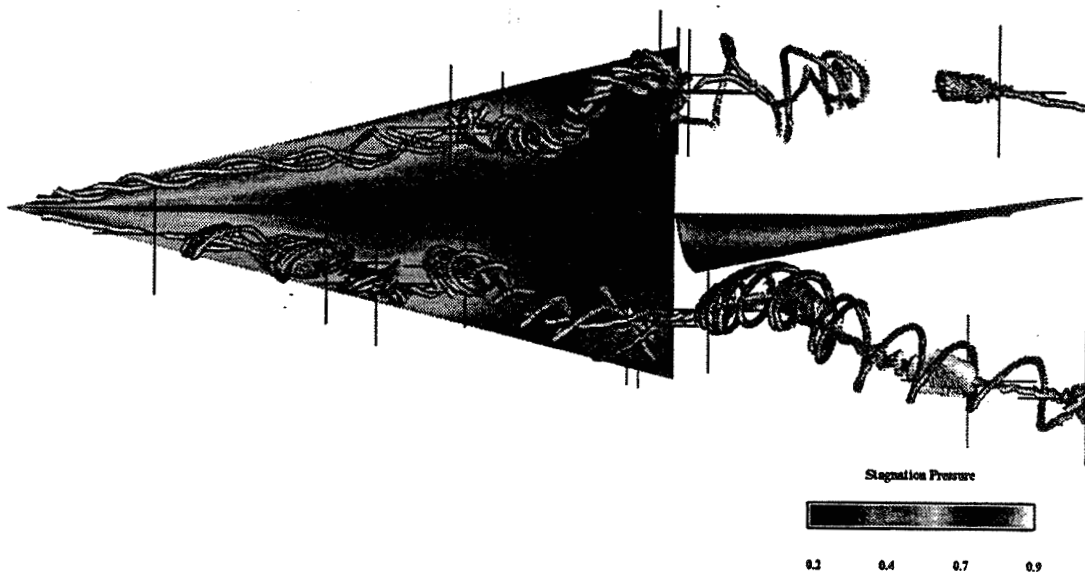


Fig (4) Top view and three-dimensional view of the wing-tail configuration for the uncoupled bending-torsion case, $R_e = 10^6$, $\Delta t = 0.0022$, $it = 12,000$.

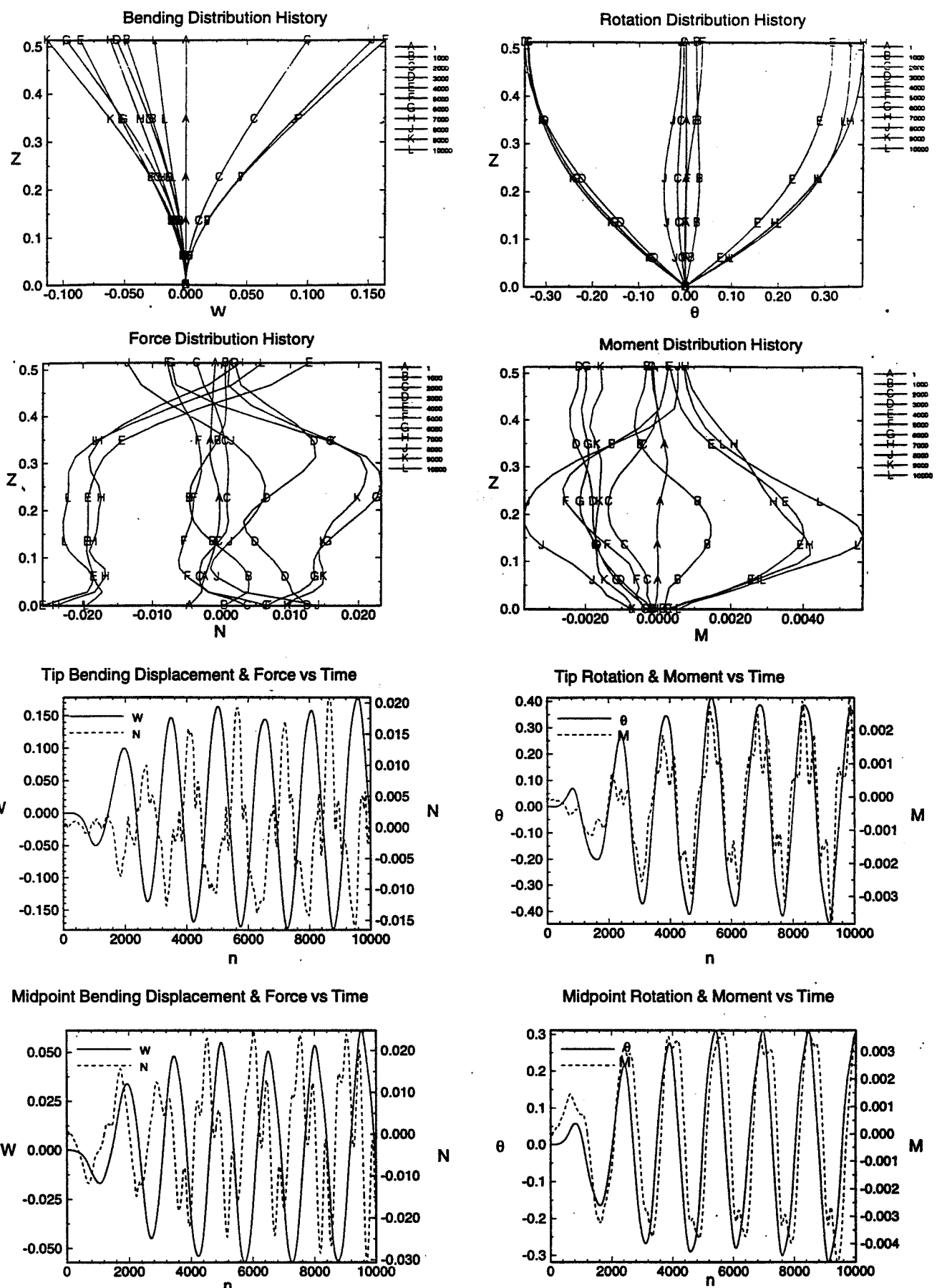


Fig (5) Deflection and load responses for the coupled bending-torsion case,
 $R_e = 10^6$, $\Delta t = 0.0022$, $it = 8,000 - 18,000$.

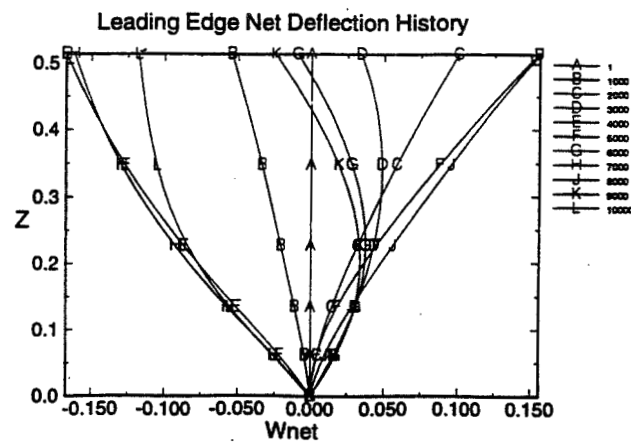


Fig (6) Net deflection of the tail leading edge for the coupled bending-torsion case, $R_e = 10^6$, $\Delta t = 0.0022$, $it = 8,000 - 18,000$.

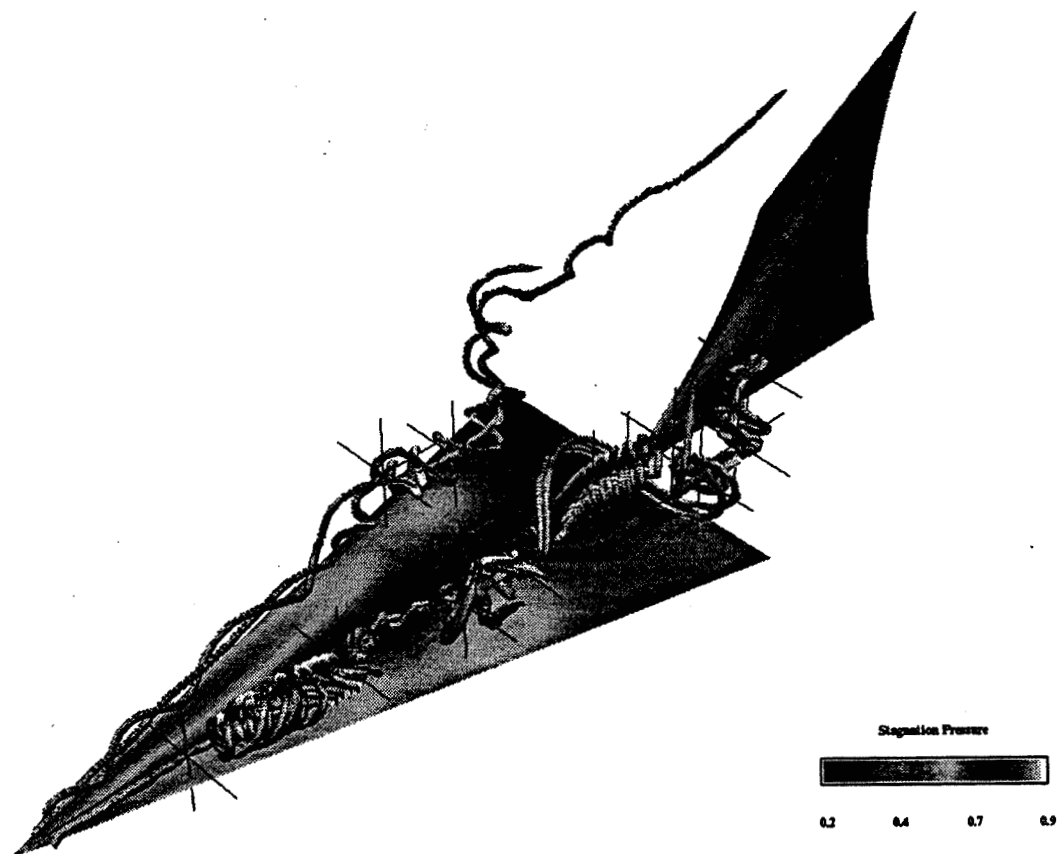


Fig (7) Three-dimensional view of the wing-tail configuration for the coupled bending-torsion case, $R_e = 10^6$, $\Delta t = 0.0022$, $it = 12,000$.

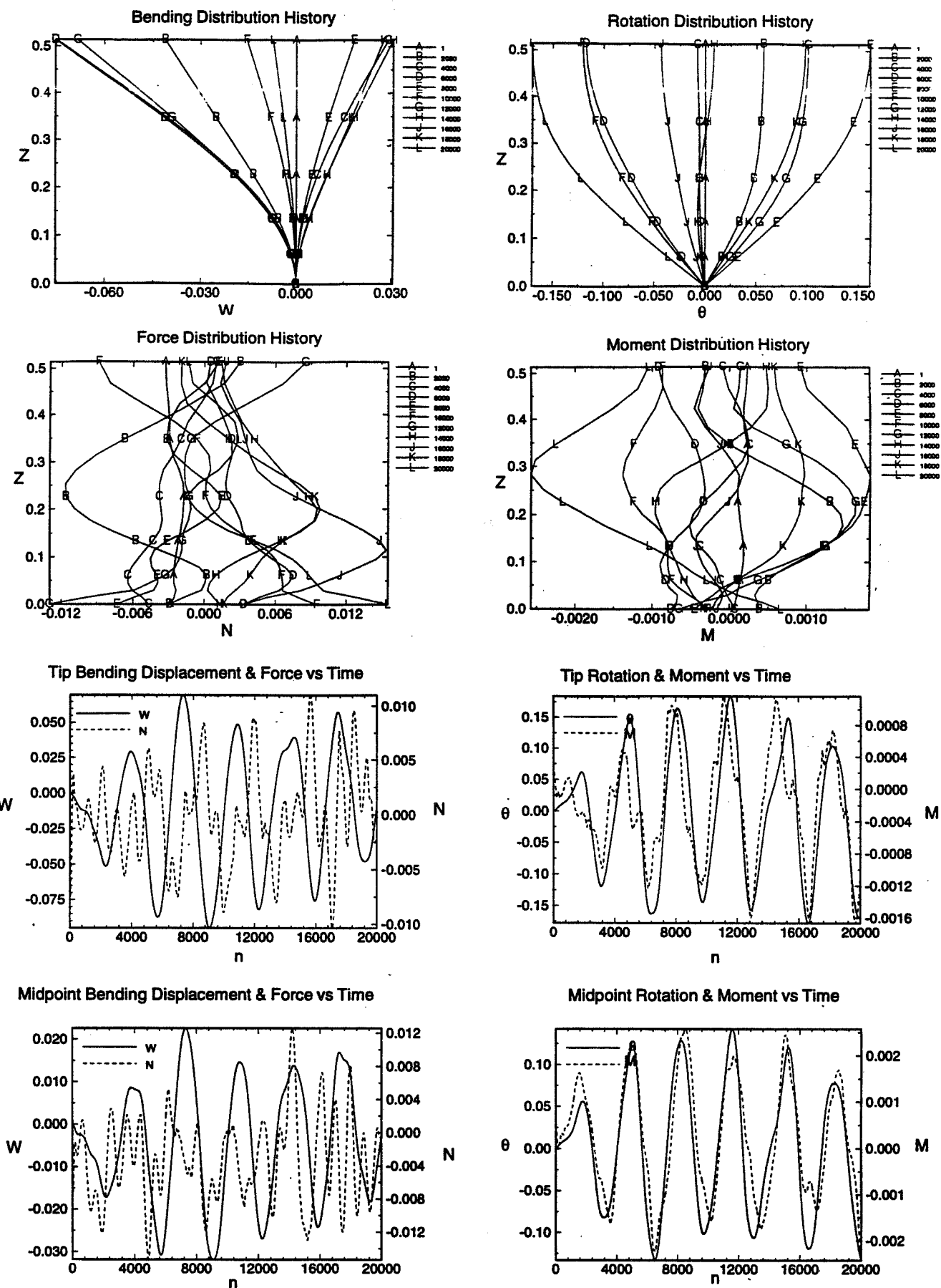


Fig (8) Deflection and load responses for the uncoupled bending-torsion case,
 $R_e = 10^4$, $\Delta t = 0.0011$, $it = 8,000 - 28,000$.

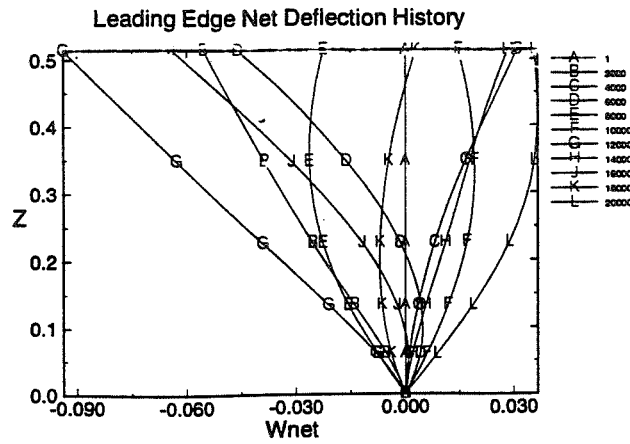


Fig (9) Net deflection of the tail leading edge for the uncoupled bending-torsion case, $R_e = 10^4$, $\Delta t = 0.0011$, $it = 8,000 - 28,000$.

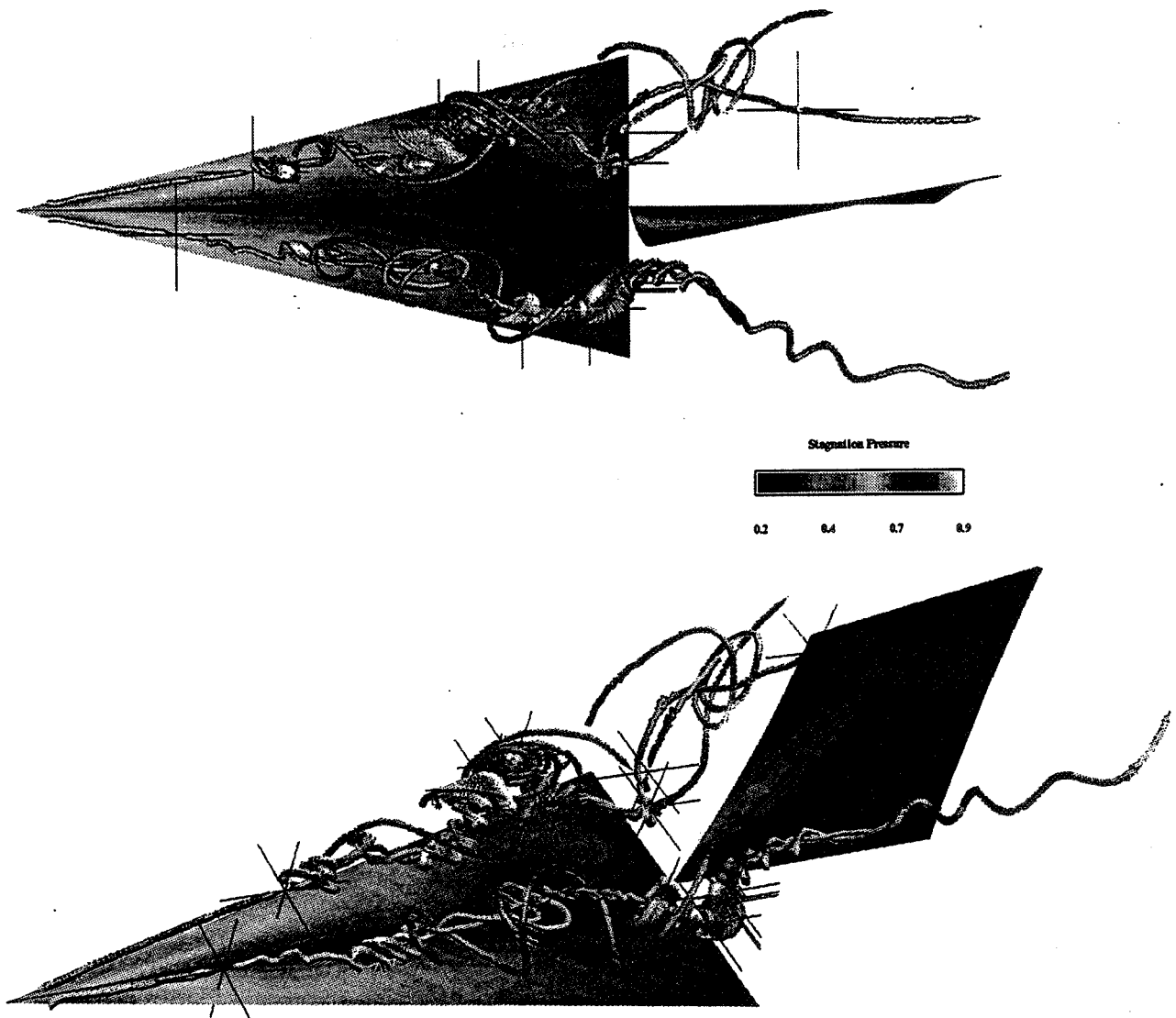


Fig (10) Top view and three-dimensional view of the wing-tail configuration for the uncoupled bending-torsion case, $R_e = 10^4$, $\Delta t = 0.0011$, $it = 16,000$.



34-02

38278

Gurnee/DE

AIAA-95-1771-CP

**FORCED ROLLING OSCILLATION
OF A 65°-DELTA WING
IN TRANSONIC
VORTEX-BREAKDOWN FLOW**

Margaret A. Menzies, Osama A. Kandil, and Hamdy A. Kandil

**Aerospace Engineering Department
Old Dominion University
Norfolk VA 23529**

**13th AIAA APPLIED
AERODYNAMICS CONFERENCE
Sheraton Harbor, CA-June 19-22, 1995**

FORCED ROLLING OSCILLATION OF A 65°-DELTA WING IN TRANSONIC VORTEX-BREAKDOWN FLOW

Margaret A. Menzies*, Osama A. Kandil†, and Hamdy A. Kandil‡
Aerospace Engineering Department
Old Dominion University, Norfolk VA 23529

ABSTRACT

Unsteady, transonic, vortex dominated flow over a 65°-sharp-edged, cropped-delta wing of zero thickness undergoing forced rolling oscillations is investigated computationally. The wing angle of attack is 20° and the free stream Mach number and Reynolds number are 0.85 and 3.23×10^6 , respectively. The initial condition of the flow is characterized by a transverse terminating shock which induces vortex breakdown of the leading edge vortex cores. The computational investigation uses the time accurate solution of the laminar, unsteady, compressible, full Navier-Stokes equations with the implicit, upwind, Roe flux-difference splitting, finite-volume scheme. While the maximum roll amplitude is kept constant at 4.0°, both Reynolds number and roll frequency are varied covering three cases of forced sinusoidal rolling. First, the Reynolds number is held at 3.23×10^6 and the wing is forced to oscillate in roll around the axis of geometric symmetry at a reduced frequency of 2π . Second, the Reynolds number is reduced to 0.5×10^6 to observe the effects of added viscosity on the vortex breakdown. Third, with the Reynolds number held at 0.5×10^6 , the roll frequency is reduced to 1π to complete the study.

INTRODUCTION

The need for developing the capability to predict and understand complex flows around modern fighter aircraft at moderate to high angles of attack has generated considerable interest. These unsteady flows around highly swept wings are characterized by the existence of large and small scale unsteady vortices, moving shock waves of varying strength, time-dependant vortex-shock interactions and unsteady asymmetric flows with vortex shedding and breakdown. Not only is understanding of the flow response due to oscillations crucial for improving the performance and maneuvering capability of defense fighters (e.g. YF22), but it is imperative for stability and control of these aircraft.

A considerable amount of experimental¹⁻³ and computational⁴⁻⁸ research has been dedicated to vortical flows around delta wings in the low-speed regime where at large angles of attack, the leading-edge primary vortex breaks down. In supersonic flow with shock waves appearing above and below the primary vortex further experimental⁹⁻¹⁰ and computational¹¹⁻¹³ research has been pursued. Recent experimental measurements of transonic flows around a 65°-cropped delta wing¹⁴⁻²⁰ show that a

complex shock-wave system appears over the upper wing surface. The shock-wave system consists of a ray shock wave beneath the leading-edge primary vortex and a transverse, time-dependent¹⁵, normal-shock wave (known as a terminating shock) which runs from the plane of symmetry to the wing leading edge. The terminating shock wave interacts with the primary-vortex core causing it to breakdown at an angle of attack as low as 18°.

Computational simulations for transonic delta-wing flows have been developed on a very limited scale by using the Euler equations¹⁹⁻²¹ and the thin-layer Navier-Stokes equations²². The Euler-equations solutions were not capable of fully resolving the flow in the terminating shock region and the thin-layer Navier-Stokes equations solutions did not address that region. In Refs. 23 and 24 by Kandil, Kandil and Liu, the laminar, unsteady, compressible, full Navier-Stokes equations are integrated time accurately to study and construct the flow field structure of a transonic flow around a 65° sharp-edged, cropped-delta wing at 20° angle of attack, 0.85 Mach number and 3.23×10^6 Reynolds number. A shock system, which consists of a ray shock under the primary vortex core and a transverse terminating shock, has been captured. Behind the terminating shock, the leading-edge vortex core breaks down into a bubble type. The flow field ahead of the terminating shock includes a supersonic pocket which is surrounded by the ray shock and the terminating shock. These results have been validated using the available experimental data and they are in good agreement.

Many low speed²⁵⁻²⁷ and supersonic²⁸⁻³⁰ studies have focused on the self excited rolling phenomenon known as wing-rock, which is characterized by large amplitude, high frequency, rolling oscillations. However, most fighters when supermaneuvering operate in the transonic regime. In this paper, the 65° sharp-edged, cropped delta wing is forced to oscillate in roll at an angle of attack of 20° and freestream Mach number of 0.85. The focus of this work is to study the behavior of the terminating shock, the vortex-breakdown flow behind the terminating shock, and the aerodynamic response of the wing due to its forced rolling oscillation in the vortex-breakdown flow.

FORMULATION

Governing Equations:

The conservative form of the dimensionless, unsteady, compressible, full Navier-Stokes equations in terms of the time-dependent, body-conformed coordinates ξ^1 , ξ^2 , and ξ^3 , is given by:

$$\frac{\partial \bar{Q}}{\partial t} + \frac{\partial \bar{E}_m}{\partial \xi^m} - \frac{\partial (\bar{E}_v)_s}{\partial \xi^s} = 0 \quad (1)$$

$$m = 1, 2, 3; s = 1, 2, 3$$

*Graduate Research Assistant, AIAA Member.

†Professor, Eminent Scholar and Department Chairman, AIAA Associate Fellow.

‡Research Assistant Professor, AIAA Member.

Copyright © 1995 by Osama A. Kandil. Published by The American Institute of Aeronautics and Astronautics, Inc. with permission.

where

$$\xi^m = \xi^m(x_1, x_2, x_3, t) \quad (2)$$

$$\bar{Q} = \frac{\hat{q}}{J} = \frac{1}{J} [\rho, \rho u_1, \rho u_2, \rho u_3, \rho e]^t \quad (3)$$

The definitions of the inviscid and viscous fluxes; \bar{E}_m and $(\bar{E}_v)_s$, are given in Ref. 30.

Boundary and Initial Conditions and Grid Motion:

All boundary conditions are explicitly implemented. They include inflow-outflow conditions, solid-boundary conditions and plane of geometric symmetry conditions. At the plane of geometric symmetry, periodic conditions are enforced. At the inflow boundaries, the Riemann-invariant boundary-type conditions are enforced. At the outflow boundaries, first-order extrapolation from the interior point is used.

Since the wing is undergoing rolling motion, the grid is moved with the same angular motion as that of the body. The grid speed, $\frac{\partial \xi^m}{\partial t}$, and the metric coefficient, $\frac{\partial \xi^m}{\partial n}$, are computed at each time step of the computational scheme. Consequently, the kinematical boundary conditions at the inflow-outflow boundaries and at the wing surface are expressed in terms of the relative velocities. The dynamical boundary condition, $\frac{\partial p}{\partial n}$, on the wing surface is no longer equal to zero. This condition is modified for the oscillating wing as:

$$\frac{\partial p}{\partial n} \Big|_{wing} = -\rho \vec{a} \cdot \hat{n} \quad (4)$$

where \vec{a} is the acceleration of a point on the wing flat surface; \hat{n} , the unit normal to the wing surface which is equal to the unit vector \vec{e}_z for a flat surface. The acceleration is given by:

$$\vec{a} = \vec{\Omega} \times \vec{r} + \vec{\Omega} \times (\vec{\Omega} \times \vec{r}) \quad (5)$$

where $\vec{\Omega}$ is the angular velocity. Notice that for a rigid body, the position vector \vec{r} , is not a function of time and hence, $\vec{r}' = \vec{r}'' = 0$. Finally, the boundary condition for the temperature is obtained from the adiabatic boundary condition and is given by:

$$\frac{\partial T}{\partial n} \Big|_{wing} = 0 \quad (6)$$

The initial conditions correspond to the flow solution around a stationary wing at an angle of attack of 20° that was impulsively injected into a free stream with $M_\infty = 0.85$, and Reynolds number of 3.23×10^6 . The solution after 18,000 time steps at a $\Delta t = 0.0002$ (corresponding to a total dimensionless time of 3.6) is then used for the starting point of all subsequent cases.

COMPUTATIONAL SCHEME

The implicit, upwind, flux-difference splitting, finite-volume scheme is used to solve the unsteady, compressible, full Navier-Stokes equations. This scheme uses the flux-difference splitting of Roe and a smooth flux limiter is used to eliminate oscillation at locations of large flow gradients. The viscous and

heat flux terms are linearized in time and the cross derivative terms are eliminated in the implicit operator and retained in the explicit terms. The viscous terms are differenced using second-order accurate central differencing. The resulting difference equation is approximately factored to solve the equations in three sweeps in the ξ^1 , ξ^2 , and ξ^3 , directions. The computational scheme is coded in the computer program "FTNS3D"

The method of solution consists of two steps. In the first step, the problem is solved for the stationary wing at 20° angle of attack and a 0° roll angle. This solution represents the initial conditions for the second step. In the second step, the wing rolling function is specified and the Navier-Stokes equations are solved accurately in time. At each time step, the wing and the grid are rotated through an angle corresponding to the wing rolling angle. The metric coefficients and the grid speed are computed and the Roe flux-differencing scheme is used to obtain the solution. The computations proceed until periodic response is reached.

COMPUTATIONAL RESULTS AND DISCUSSION

A 65° swept-back, sharp edged, cropped delta wing of zero thickness is considered for the computational solutions. The cropping ratio (tip length/root-chord length) is 0.15. An O-H grid of $125 \times 85 \times 84$ in the wrap-around, normal, and axial directions, respectively, is used. The computational domain extends two-chord lengths forward and five-chord lengths backward from the wing trailing edge. The radius of the computational domain is four-chord lengths. The minimum grid size in the normal direction to the wing surface is 5×10^{-4} from the leading edge to the plane of symmetry. The initial conditions correspond to the solution of the wing held at 20.0° angle of attack and 0.0° roll angle after 18,000 time steps. The grid is then coarsened due to impeding computational cost to $65 \times 43 \times 84$, wrap-around, normal, and axial directions, respectively. This is accomplished by retaining the odd numbered grid points in the wrap-around and normal directions. The cell centered fine solution is then interpolated to the coarse grid by averaging in both the normal and lateral directions simultaneously.

Initial Conditions (Stationary Wing), $\theta_i = 0.0^\circ$:

Plots of the initial conditions depict a solution characterized by weak oblique shocks beneath the primary vortices and a terminating shock located at approximately $x = 0.86$ (See Fig. 1.) These shocks bound a substantial supersonic pocket. Immediately behind the transverse shock, centered about the plane of symmetry, a large high pressure region is observed in the breakdown. Careful study of the pressure contours in Fig. 1 shows that this area contains two regions of high pressure gradients; the leading edge, the terminating shock and at $x = 0.93$. Outboard of the oblique shocks, a subsonic, separated region depicts a secondary vortex which exists until $x = 0.91$. The enlarged primary vortex diffuses and behaves as an attracting and repelling spiral saddle critical point indicating vortex breakdown due to the terminating shock (See Fig. 2.) Total Mach contours and streamlines on the vertical ray planes, (Fig. 3) depict clearly a bubble type vortex breakdown and the flow appears to be completely symmetric. The resulting lift coefficient is approximately 0.408.

Case I-High Reynolds number Rolling Oscillation,

$$\theta = 4.0^\circ \sin 2\pi t:$$

From the initial conditions with $Re = 3.23 \times 10^6$, the wing is forced to oscillate in roll around the axis of geometric symmetry. The amplitude of rolling oscillation (θ_a) is 4.0° and the reduced frequency (k) is 2π . The period corresponding to the frequency is one and with a $\Delta t = 0.001$, each cycle of oscillation takes 1,000 time steps. The motion starts with the right-hand side of the wing (looking in the upstream direction) rolling downward. The case is run for 12 complete cycles and periodicity is achieved after 6.5 cycles.

Transient Response:

Figure 4 shows that with the onset of motion, the lift coefficient increases in an oscillatory fashion until periodicity is achieved after 6.5 cycles. The rate of change of the lift coefficient increases as well, until the third cycle. The largest increase occurs from $t = 1.25$ where $Cl = 0.422$ to $t = 2.25$ where $Cl = 0.448$. Unlike the lift coefficient, the rolling moment coefficient is cyclic after the first cycle and oscillates between ± 0.14 . The position and strength of the left and right side vortex breakdown and ultimate disappearance of the breakdown over time possibly explain this inconsistency.

At the initial conditions, the flow is symmetric and each side of the wing experiences vortex breakdown at approximately $x = 0.86$ (Fig. 3). After the first quarter cycle, the pressure gradient in the high pressure region behind the terminating shock moves forward from $x=0.93$ to $x = 0.88$ closing the axial distance between the two gradients. The Mach contours of the vertical planes show significant asymmetry as the vortex breakdown bubble is compressed on the left side of the wing (the side moving upwards). Breakdown occurs on the expansion (downward) side just ahead of the breakdown on the compressed side of the wing.

After a half cycle is completed, the wing passes back through zero degrees of roll. At the maximum roll velocity, the right side is compressing the flow while the left (going downward) side is expanding it. On the plane of symmetry, the secondary pressure compression joins the terminating shock which moves aft slightly and as a result of the combining gradients, appears much stronger. The vortex breakdown on the right side appears more compressed and hovers closer to the wing surface. The bubble cells inside the breakdown separates fore to aft leading toward a spiral type breakdown. The left side appears similar to that of the initial conditions.

As the motion continues (left side down when looking upstream), the terminating shock on the plane of symmetry starts to expand and moves forward. The right side breakdown develops into a spiral which is greatly reduced in size when compared to the initial conditions. The left side develops an additional attracting and repelling spiral saddle point in the bubble breakdown. The breakdown location moves forward from approximately $x = 0.85$ to $x = 0.80$ on the left, while the right side appears stationary at $x = 0.85$.

With the completion of the first cycle, further expansion and weakening of the terminating shock around the plane of symmetry is observed. The supersonic pocket is significantly smaller than at the initial conditions as the shock on the plane of

symmetry moves to approximately $x=0.70$. It is interesting to note that on the right (expanded) side, the breakdown develops a bubble amid the spiral type breakdown and on the left (compressed) side, the breakdown is reduced from four to just two bubble cells. Breakdown occurs on the right side at approximately $x = 0.81$ and on the left at approximately $x = 0.85$. Figures 5 and 6 show snapshots at each quarter cycle.

With continued motion, the transverse shock near the plane of symmetry continues to move forward, expand and weaken until it disappears shortly after the completion of the second cycle. The vortex breakdown dissipates becoming weakened spirals. After two cycles are completed, the lift coefficient undergoes the largest rate of change while the rolling moment converges to periodicity. This indicates that the vortex breakdown position shifts from fore to aft as the core compresses and expands due to the wing motion. Simultaneously, the breakdown is weakened resulting in the overall increase in lift. To further this hypothesis, the pitching moment coefficient, plotted in Fig. 7, increases in magnitude over time in the same fashion as the lift coefficient. This suggests that as the breakdown weakens and ultimately disappears, that the lift of the wing is increased due to additional lift from the aft portion of the surface where the breakdown occurs. The cyclic rolling moment curve is produced by the relative fore and aft position and relative strength of the vortex breakdowns of the right and left sides oscillating with the motion.

The pressure contours on the plane of symmetry indicates that the terminating shock initially moves forward for the first quarter cycle. It is joined by the secondary high pressure gradient and shifts aft after the first half cycle and then the shock moves forward weakening until the completion of the second cycle. After the second cycle was completed, another pressure gradient develops on the trailing edge of the wing. As the motion continues, this compression moves forward and strengthens until periodicity is achieved, and the gradient remains stationary at $x = 0.80$. Additionally, observation of the pressure contours on the wing surface depict a gradient that cycles forward in position on the outer edges from side to side as the wing rolls. Figures 8 and 9 are samples of these plots. After the sixth cycle the oscillations in position of the pressure gradient cease.

Periodic Response:

After six and one half cycles, periodicity is achieved with only minor fluctuations per oscillation noted in the lift coefficient. The coefficient of lift oscillates between 0.480 and 0.494 leading the roll angle with a phase angle just greater than 90° with minimal hysteresis noted. The coefficient of rolling moment leads the roll angle by 90° and oscillates between ± 0.14 .

This flow has no notable vortex breakdown and the transverse terminating shock extends evenly at $x = 0.80$. Streamlines along vertical planes sectioning the vortex flow showed a very clean flow with little or no disturbance (See Fig. 10.) As the wing rolls, the primary vortex core expands on the wing side moving downward. This effect appears strongest as the wing rolls through zero degrees. By $x = 0.85$ a secondary vortex is depicted. Similar to the primary vortex, it too experiences compression and expansion as the wing rolls changing shape from a small circular core when compressed to an elongated vertically ellipsoidal shaped core when expanded. Figure 11 illustrates a

typical cycle. In Fig. 12, the three peaks depicted are the primary, secondary and tertiary vortices.

Computer Simulation:

To generate the computer animation, the flow field solution and rotated grid coordinates are recorded every 5 computational cycles (this corresponds to dimensionless time of 0.005). From each solution and grid file, a frame for each view in the animation is produced using the plotting packages known as FAST and Tecplot. One view animates the total pressure contours on cross-flow planes initially positioned on either side of the vortex breakdown. The second view shows the total mach contours on the wing surface and several instantaneous streamlines passing through the vortex core. A plot of the lift coefficient curve is displayed in addition to the two views of the flow field. A total of 4,800 frames (1,600 per view) are used to simulate the wing rolling through 8 complete cycles. The completed frames are recorded on video at a speed of approximately 24 frames per second.

Case II-Reduced Reynolds Number Rolling Oscillation,

$$\theta = 4.0^\circ \sin 2\pi t:$$

Restarting from the same initial conditions as in case I, the Reynold's number is lowered to 0.5×10^6 . The wing is again forced to oscillate in roll around the axis of symmetry with the same amplitude, $\theta_a = 4.0^\circ$, and reduced frequency, $k = 2\pi$, as in the previous case. Again, the motion started with the right-hand side of the wing (looking in the upstream direction) rolling downward. The case is run for 12 complete cycles and periodicity is achieved after only 5.5 cycles.

Transient Response:

The fluid behavior is similar to that of case I. The first noticeable difference is the plot of the lift coefficient as shown in figure 13. The increasing rate of change for the lift coefficient continues until, as in case I, the third cycle. The largest increase occurred one half cycle later from $t = 1.75$ with $Cl = 0.440$ to $t = 2.75$ with $Cl = 0.452$. The lift coefficient also stabilized at a slightly lower value of 0.475 vice 0.484 for $Re = 3.23 \times 10^6$. Periodicity is achieved in one less cycle than in case I; however, the mean of the lift coefficient decreases slightly after the seventh cycle. The rolling moment coefficient curve appears to be identical.

Periodic Response:

After five and one half cycles, periodicity was achieved. The coefficient of lift oscillated between 0.472 and 0.484 leading the roll angle in phase just greater than 90 degree with a similar hysteresis as experienced with case I. The rolling moment coefficient curve appeared to be identical ranging ± 0.14 with a phase lead of 90° referenced to the roll angle.

Case III-Reduced Reynolds number and Frequency,

$$\theta = 4.0^\circ \sin 2\pi t:$$

From the initial conditions, the Reynolds number is lowered to $Re = 0.5 \times 10^6$. The wing is then forced to oscillate in roll with a maximum roll amplitude, (θ_a), of 4.0° and a reduced frequency, (k), of 1π . This frequency corresponds to a

period of 2 and with $\Delta t=0.001$, each cycle of oscillation takes 2,000 time steps to complete. The motion starts with the right-hand side of the wing (looking in the upstream direction) rolling downward. This case is run for nine complete cycles but periodicity is never achieved.

Transient Response:

The plot of the coefficient of lift versus roll angle, figure 14, reveals unexpected results. The first cycle produced a lift coefficient of 0.417. The lift decreases in a somewhat oscillatory manner for the next three cycles to 0.391 until the start of the fifth cycle. The lift coefficient curves of the fifth and sixth cycles are the only cycles related, appearing almost cyclic and ranging in lift from 0.397 to 0.410. Halfway through the seventh cycle the lift coefficient increases dramatically to 0.417 and hovers there for one cycle before decreasing in value.

The symmetric flow at the initial conditions has a transverse shock at $x = 0.86$ and a secondary high pressure gradient at $x = 0.93$. As in the first two cases, the two pressure gradients merge as a result of the rolling motion. However, in this case, the merger occurs during the first quarter cycle and the terminating shock moves forward to $x = 0.79$ which coincides with a large increase in the lift. The right hand side of the wing (looking in the upstream direction) is moving downward and thereby expanding the flow. The right side vortex breakdown appears larger and occurs slightly ahead of the breakdown on the left side. Similar to the previous cases, the vortex breakdown on the expanded side develops an additional bubble cell.

Plots of the second quarter cycle show that the terminating shock progresses further upstream to start pressure compression at $x = 0.70$ and passes Mach 1.0 at $x = 0.76$. The lift is relatively constant. The left (downward moving) side which expands the flow, has an enlarged vortex breakdown that advances forward from $x = 0.90$ to $x = 0.80$. The compressed vortex breakdown transfers to a spiral type breakdown but unexpectedly advances to a position forward of the expanded vortex breakdown. In the previous two cases, the expanded side vortex breakdown occurred forward of the compressed side vortex breakdown.

Continued motion of the wing strengthens the terminating shock which advances to $x = 0.70$. The expanded flow side of the wing develops another bubble cell in the breakdown and both right and left vortex breakdowns appear at $x = 0.80$.

The first cycle is completed by reversing motion to a roll angle of 0° . The terminating shock expands, weakens and advances further to $x = 0.64$. Behind the shock, the region of constant pressure develops which is bounded at $x = 0.90$. This combination produces the maximum lift coefficient. The vortex breakdown on the left side, upward moving, reduces to spirals and remains stationary while the right side breakdown advances from $x = 0.80$ to $x = 0.75$. Figures 15 and 16 show snapshots at each quarter cycle.

Plots of the start of the second cycle show the terminating shock pressure compression narrows and strengthens but remains at $x = 0.64$. The aft boundary of the high pressure region behind the shock advances to $x = 0.85$ and is depicted by a negative pressure gradient. At this point, the lift starts to decrease. Both vortex breakdowns advance although the right expanded side

breakdown, appears forward of the left side breakdown. The left side vortex breakdown is compressed and flattened due to the motion of the wing. Three trends in the behavior of the vortex breakdowns continue for the remainder of the case. First, the vortex breakdowns exhibit longitudinal oscillations with the right side leading. Second, during these oscillations the breakdowns move forward. Third, the compressed side breakdown appear flattened when compared to the expanded side. See figure 17.

From 1.25 cycles to 1.5 cycles, plots of the pressure contours appear very similar. The lift coefficient remains constant at $C_l = 0.412$. Continued to the maximum roll position, the transverse high pressure gradient advances to $x = 0.60$, the aft boundary of the high pressure region advances, and a second high pressure gradient appears on the trailing edge.

In the next two quarter cycles, the transverse pressure compression is greatly expanded and the lift coefficient continues to decrease. The region of high pressure is considerably smaller and farther forward starting at $x = 0.55$ and bounded at $x = 0.65$. By 2.75 cycles, the lift coefficient decreases to $x = 0.397$. The high pressure area favors the expanded side on the aft boundary, and plots of the pressure contours on the plain of symmetry show a distinctive area of low pressure at $x = 0.95$ just prior to a developing shock. See figure 18.

Figure 19 isolates the lift coefficient curves for the fifth and sixth cycles, the only cycles that appear similar in shape. The vortex breakdowns occur on the right side at $x = 0.35$ and on the left side at $x = 0.50$ throughout both cycles as depicted in figure 20. The pressure contours plotted on the surface show a weak terminating shock near the trailing edge. The terminating shock of the sixth cycle, which had the higher lift values, is located farther forward than in the fifth cycle. The region of high pressure is greatly reduced in size and located on the front half of the wing. Additional high and low pressure pockets develop aft of centerline.

By the close of the seventh cycle the lift coefficient has increased substantially. The most notable change in the flow characteristics from previous cycles is the weakening and ultimate disappearance of the newly developed terminating shock. With continued motion, the shock reappears at $x = 0.90$ thereby reducing the lift coefficient values.

CONCLUSION

The unsteady, compressible, full Navier-Stokes equations are integrated time accurately using the implicit, upwind, flux-difference splitting, finite-volume scheme to study the unsteady transonic flow around a 65° sharp-edged, cropped delta wing. The wing is first forced to oscillate in roll around the axis of symmetry with a maximum roll amplitude, θ_a , of 4.0° and a reduced frequency, k , of 2.0. It has been shown that the rolling motion affected the flow most significantly at the zero degree roll angle where the roll velocity is at a maximum. This is consistent with the noted phase lead of 90° for the rolling moment coefficient and the 90+° lead of the lift coefficient. Initially, the expansion (downward moving) side vortex breakdown tends to occur slightly ahead of the compression side breakdown. The terminating shock moves upwind and weakens with the motion until after the second cycle. A secondary high pressure gradient is initiated from the trailing edge and like the terminating shock

also moves upwind until periodicity is reached. However, this secondary high pressure gradient does not produce vortex breakdown and the lift coefficient increases in an oscillatory manner until the initial vortex breakdown washes downwind. When viewing the animation, it is clear that the core of the vortex is undisturbed by the advance of secondary high pressure gradient which results in the overall increase in lift.

The second case demonstrated that the rate of change in the lift coefficient is related to the position and strength of the trailing edge high pressure gradient and periodicity was achieved in one less cycle with a lower Reynolds number. The overall lift decreased and the strength of the primary vortex and secondary pressure gradient appeared reduced due to the lower Reynolds number. But reducing Reynolds number alone did not significantly alter the features of the fluid flow. However, reducing the rolling frequency in conjunction with the Reynolds number reduction, as in the third case, substantially altered the fluid flow. The variation of the lift coefficient curve for the third case is attributed to the following three factors: 1) the position and size of the high pressure region, 2) the intensity of the pressure gradients bounding the high pressure region, and 3) the position and strength of the shock that developed from the trailing edge. Additionally, but to a lesser extent, the position of the right and left side vortex breakdown also affected the lift coefficient curve. The behavior of the vortex breakdown established three trends. First, the vortex breakdowns exhibited longitudinal oscillations with the right side leading. Second, during these oscillations, the breakdowns moved forward. Third, the compressed side breakdown appeared flattened when compared to the expanded side.

Using the computational methods described, complex details of unsteady, transonic flow around a delta wing undergoing rolling oscillations of varied frequency and Reynolds number have been presented and animated for the first time.

ACKNOWLEDGMENT

This work is supported by the NASA-Langley Research Center under grant No. NAG-1-648 along with partial support from the AFOSR and the Virginia Space Grant Consortium. The computational resources provided by the NAS Center at AMES and the NASA Langley Research Center are acknowledged and appreciated. Specific acknowledgment and appreciation is extended to the Data Visualization and Animation Lab, LaRC, Va.

REFERENCES

- ¹Lambourne, N.C. and Bryer, D. W., "Bursting of Leading-Edge Vortices: Some Observations and Discussion of the Phenomenon," Aeronautical Research Council, R&M 3282, 1961.
- ²Hummel, O., "On the Vortex Formation Over a Slender Wing at Large Angles of Incidence," AGARD CP-247, Jan. 1979, pp. 15.1-15.7.
- ³Verhaagen, N. G., "An Experimental Investigation of the Vortex Flow Over a Delta and Double Delta Wings at Low Speed," AGARD CP-342, Apr. 1983, pp. 7.1-7.16.

- ⁴Kandil, O. A., "Numerical Prediction of Vortex Cores from the Leading and Trailing Edges of Delta Wings," ICAS Paper No. 14.2, 12th Congress of the International Council of Aeronautical Sciences, Munich, Germany, Oct. 1980.
- ⁵Hoeijmakers, H. W. M., "Aerodynamics of Vortical Type Flows in Three Dimensions," AGARD CP-342, Jul. 1983, pp. 18.1-18.35.
- ⁶Newsome, R. W. and Kandil, O. A., "Vortical Flow Aerodynamics-Physical Aspects and Numerical Simulation," AIAA Paper 87-0205, Jan 1987.
- ⁷Thomas, J. L., Taylor, S. L. and Anderson, K., "Navier-Stokes Computations of Vortical Flows Over Low Aspect Wings," AIAA Paper 87-0207, Jan 1987.
- ⁸Kandil, O. A. and Chuang, H. A., "Computation of Vortex-Dominated Flow for a Delta Wing Undergoing Pitching Oscillations," AIAA Journal, Vol. 28, No. 9, Sept. 1990, pp. 1589-1595.
- ⁹Stanbrook, A. and Squire, L. C., "Possible Types of Flow at Swept Leading Edge," Aeronautical Quarterly, Vol. XV, Feb. 1964.
- ¹⁰Miller, D. S. and Wood, R. W., "Lee-Side Flow over Delta Wings at Supersonic Speeds," NASA TP 2430, 1985.
- ¹¹Kandil, O. A. and Chuang, A. H., "Influence of Numerical Dissipation on Computational Euler Equations for Vortex-Dominated Flows," AIAA Journal, Vol. 25, No. 11, Nov. 1987, pp. 1426-1434.
- ¹²Newsome, R. W. and Thomas, J. L., "Computation of Leading-Edge Vortex Flows," NACA CP-2416, Oct. 1985, pp. 305-330.
- ¹³Murman, E. M., Goodsell, A., Powell, K. and Landahl, M., "Leading Edge Vortex Solutions with Large Total Pressure Loss," AIAA Paper 87-0039, Jan. 1987.
- ¹⁴Boersen, S. J. and Elsenaar, A., "Tests on the AFWAL 65° Delta Wing at NLR: A Study of Vortex Flow Development Between Mach = 0.4 and 4," Proceedings of Symposium on International Vortex Flow Experiment on Euler Code Validation, Stockholm, Sweden, Oct. 1-3, 1986, pp. 23-36.
- ¹⁵Bannink, W. J. and Houtman, E. M., "Experiments on the Transonic Flow Over a Delta Wing at High Angles of Attack," Proceedings of Symposium on International Vortex Flow Experiment on Euler Code Validation, Stockholm, Sweden, Oct. 1-3, 1986, pp. 37-46.
- ¹⁶Hartmann, K., "Force and Pressure Measurements Including Surface Flow Visualization on a Cropped Delta Wing," Proceedings of Symposium on International Vortex Flow Experiment on Euler Code Validation, Stockholm, Sweden, Oct. 1-3, 1986, pp. 63-87.
- ¹⁷Bütfisch, K. A., Pallek, D. and Saurland, K. H., "International Vortex Flow Experiment-Results of Three Component LDA Measurements on a 65° Delta Wing," DFVLR IB 222-87 A 34, 1987.
- ¹⁸Elsenaar, A., Hjelmberg, L., Bütfisch, K. and Bannink, W. J., "The International Vortex Flow Experiment," AGARD-CP-437, Lisbon, Portugal, May 1988, Vol. 1, pp. 9.1-9.23.
- ¹⁹Bannink, W. J. and Houtman, E. M., "Experimental and Computational Study of the Vortical Flow Over a Delta Wing at High Angles of Attack," IUTAM Symposium on Fluid Dynamics of High Angle of Attack, University of Japan, Tokyo, Japan, Sept. 14-17, 1992.
- ²⁰Erickson, G. E., "Wind Tunnel Investigation of the Interaction and Breakdown Characteristics of Slender-Wing Vortices at Subsonic, Transonic and Supersonic Speeds," NASA TP 3114, Nov. 1991.
- ²¹Hitzel, S. M., "Wing Vortex-Flows Up into Vortex-Breakdown-A Numerical Simulation," AIAA 88-2518-CP, 1988, pp. 73-83.
- ²²Laine, S., Siikonen, T. and Kaurinkoski, P., "Calculation of Transonic Viscous Flow Around a Delta Wing," ICAS 92-4.2.1, Beijing, PRC, Sept. 22-25, 1992, pp. 286-295.
- ²³Kandil, O. A., Kandil, H. A. and Liu, C. H., "Shock-Vortex Interaction Over a 65-Degree Delta Wing in Transonic Flow," AIAA Paper 93-2973, AIAA 24th Fluid Dynamics Conference, Orlando, FL, Jul. 6-9, 1993.
- ²⁴Kandil, H. A., Kandil, O. A. and Liu, C. H., "Supersonic Vortex Breakdown Over a Delta Wing in Transonic Flow," AIAA -93-3472-CP, AIAA Applied Aerodynamics Conference, Monterey, CA, Aug. 9-11, 1993, pp. 582-596.
- ²⁵Chaderjian, N. M., "Navier-Stokes Prediction of Large-Amplitude Delta-Wing Roll Oscillations Characterizing Wing Rock," AIAA-92-4428-CP, AIAA Atmospheric Flight Mechanics Conference, Hilton Head Island, SC, Aug. 10-12, 1992.
- ²⁶Kandil, O. A. and Salman, A. A., "Prediction and Control of Slender Wing Rock," ICAS 92-4.7.2, 18th Congress, International Council of the Aeronautical Sciences, Beijing, Peoples Republic of China, Sept. 20-25, 1992.
- ²⁷Gordnier, R. E. and Visbal, M. R., "Numerical Simulation of Delta-Wing Roll," AIAA-93-0554, 31st Aerospace Sciences Meeting and Exhibit, Reno, NV, Jan 11-14, 1993.
- ²⁸Kandil, O. A. and Chuang, H. A., "Unsteady Navier-Stokes Computations Past Oscillating Delta Wing at High Incidence," AIAA-89-0081-CP Jan. 1989. Also AIAA Journal, Vol. 28, No. 9, Sept. 1990, pp. 1565-1572.
- ²⁹Kandil, O. A. and Salman, A. A., "Unsteady Vortex-Dominated Flow Around Wings with Oscillating Leading-Edge Flaps," AIAA-91-0435, 29th Aerospace Sciences Meeting, Reno, NV, Jan 7-10, 1991.
- ³⁰Kandil, O. A. and Kandil, H. A., "Pitching Oscillation of a 65-Degree Delta Wing in Transonic Vortex Breakdown Flow," AIAA 94-1426-CP, AIAA/ASME/ASCE/AHS/ASC Structures and Structural Dynamics Conference, Hilton Head, SC Apr. 18-20, 1994.

Initial Conditions

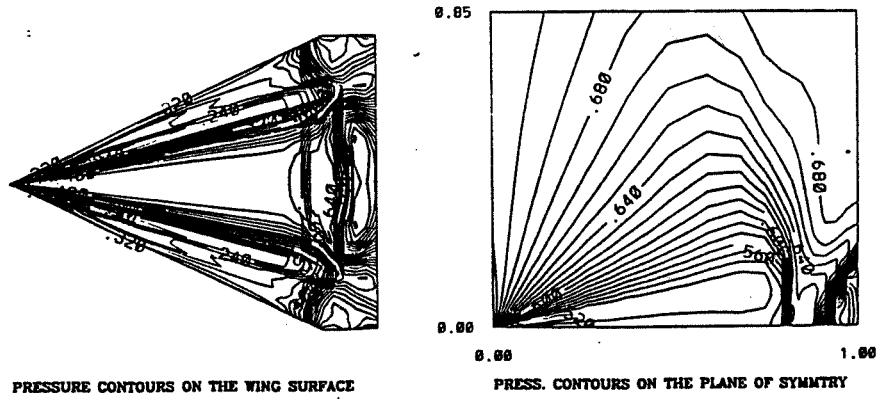


Figure 1. Static Pressure Contours on the Wing Surface and Plane of Symmetry.

$$Re = 3.23 \times 10^6, M_\infty = 0.85, \alpha = 20.0^\circ$$

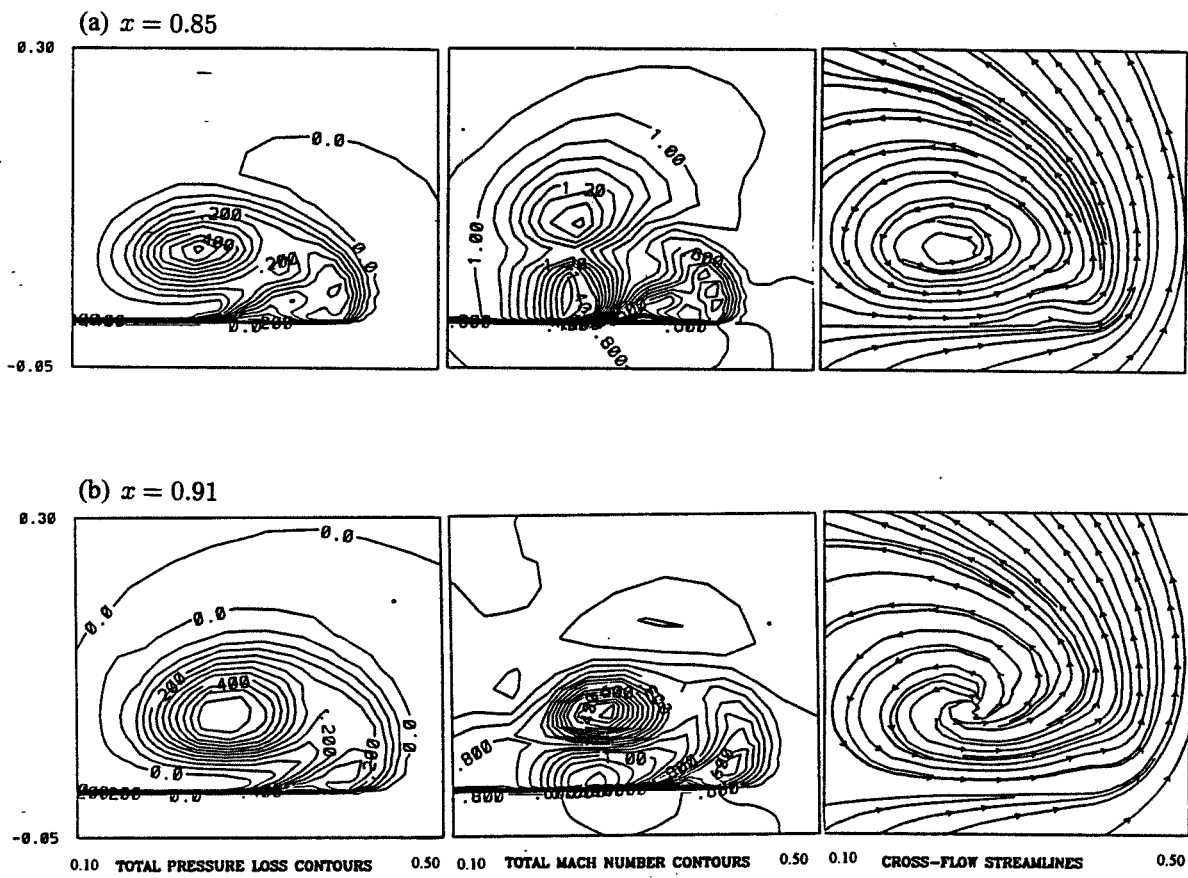


Figure 2. Total Pressure Loss Contours, Total Mach Number Contours, and Streamlines on Cross-Flow Planes Located Forward of the Shock (a), and Aft of the Shock (b).

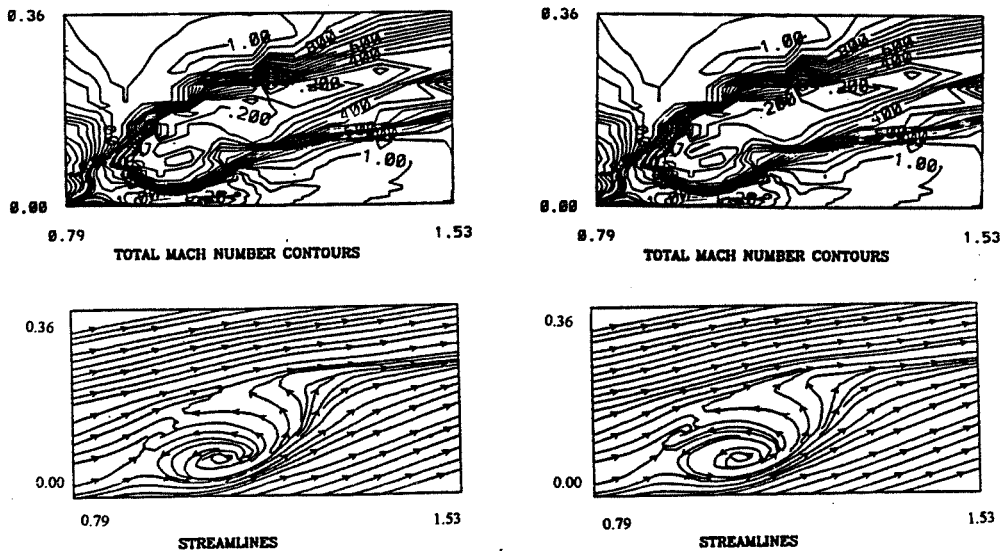


Figure 3. Total Mach Number Contours and Streamlines
on a Vertical Plane Sectioning the Vortex Breakdown.

Case I-Transient Response

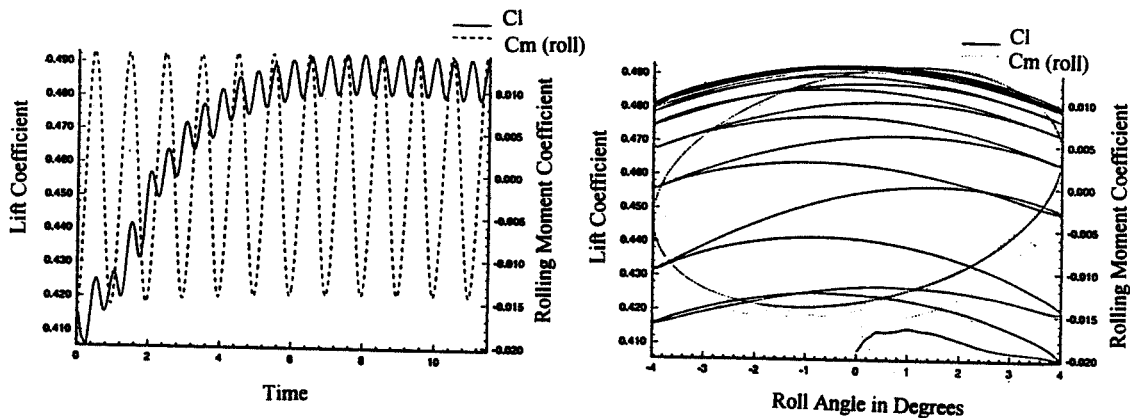


Figure 4. Coefficient of Lift and Rolling Moment versus
Time and Roll Angle During Rolling Oscillation.

$$Re = 3.23 \times 10^6, \theta = 4.0^\circ \sin 2\pi t$$

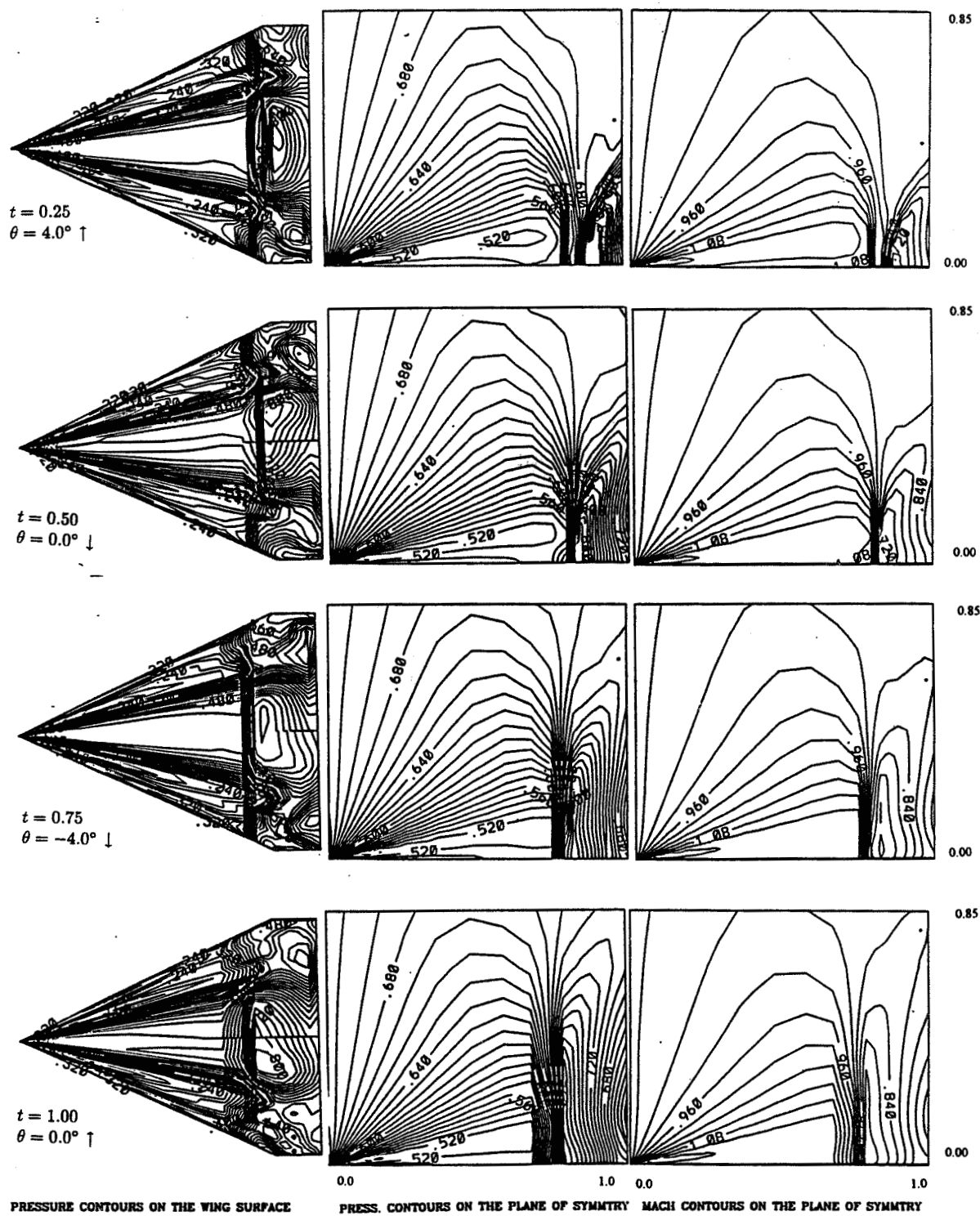


Figure 5. Snapshots of the First Cycle Shown at Each Quarter Cycle.

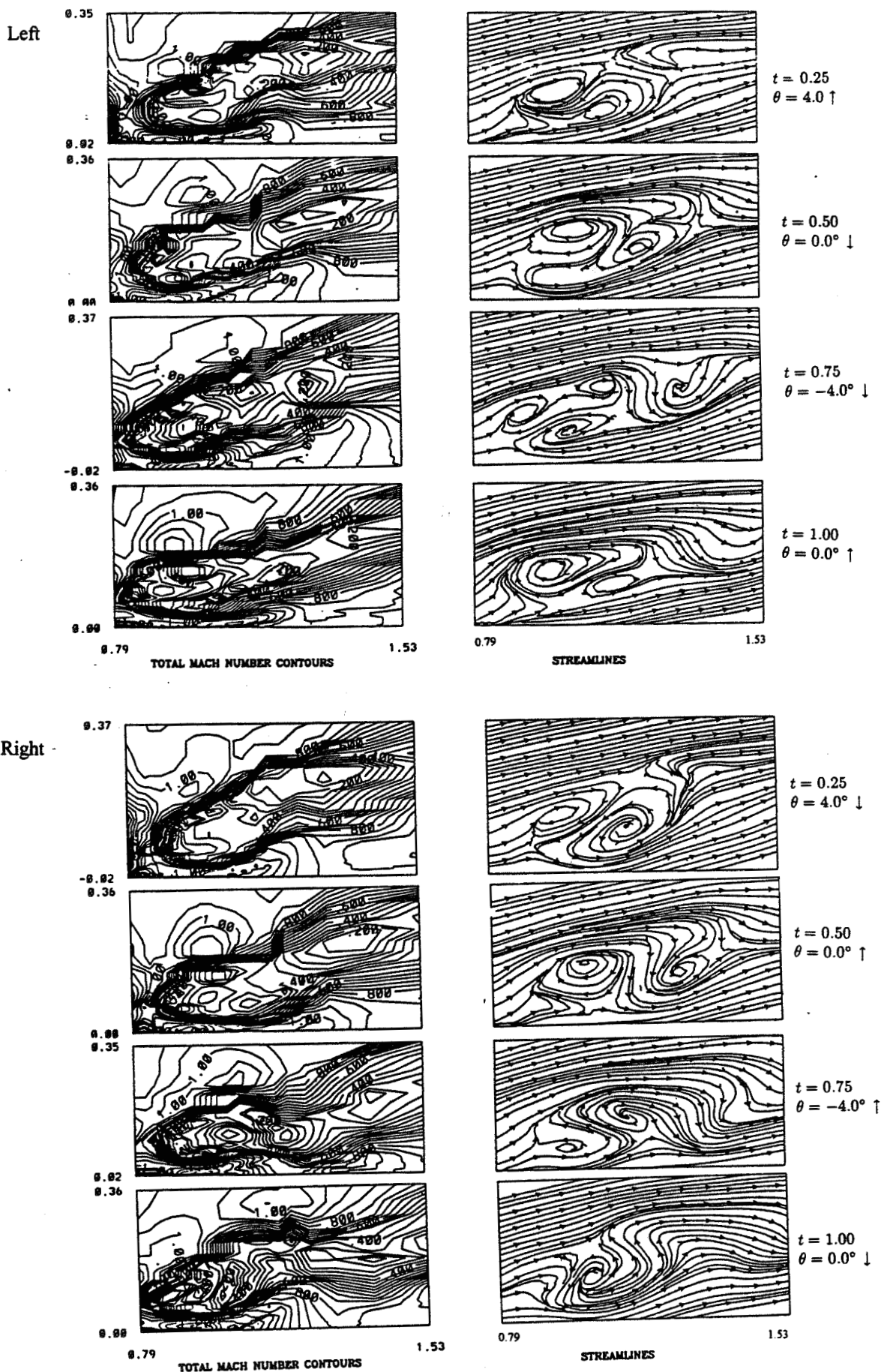


Figure 6. Snapshots of the First Cycle Shown at Each Quarter Cycle of a Vertical Plane Sectioning the Vortex Breakdown.

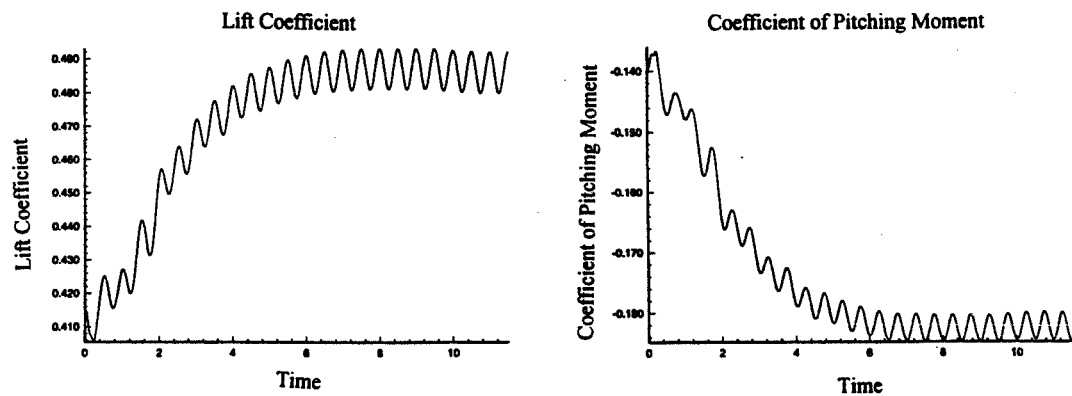


Figure 7. Comparison of the Coefficient of Lift and Pitching Moment versus Time.

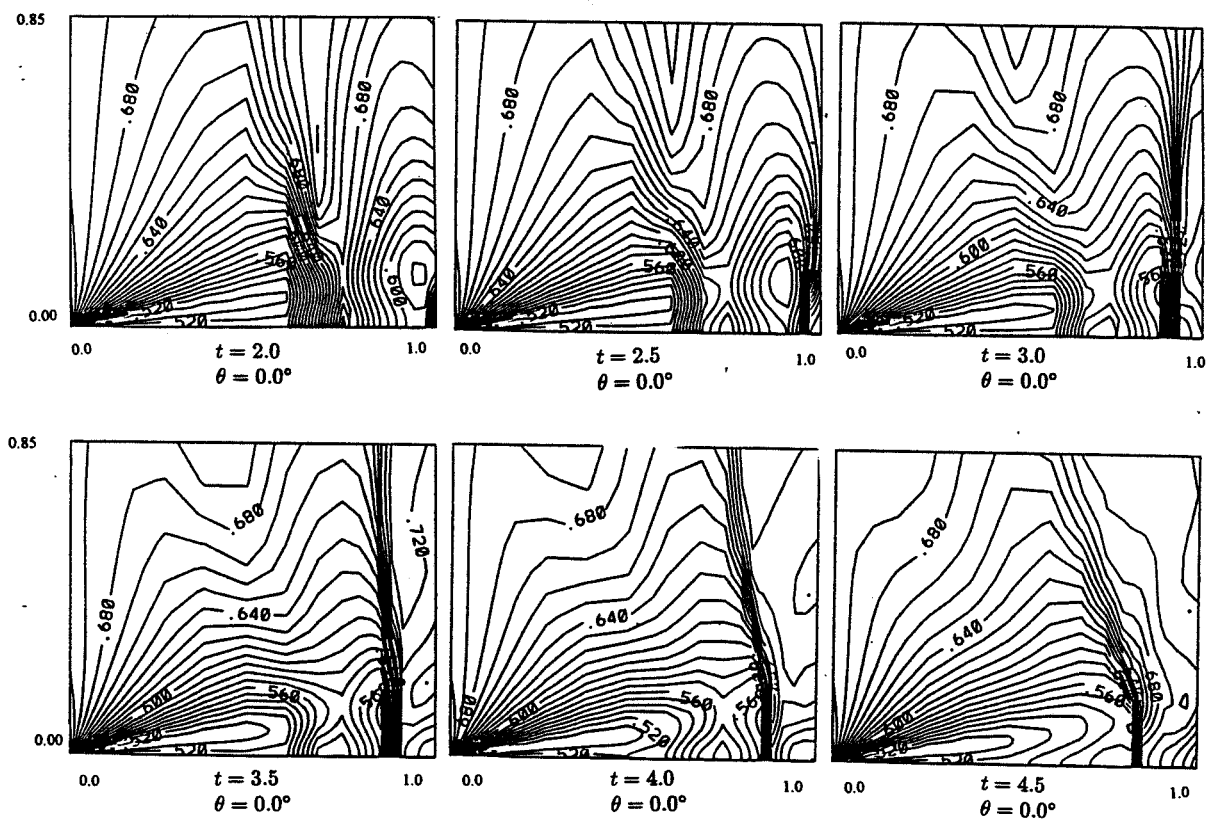


Figure 8. Samples of Static Pressure Contours on the Plane of Symmetry.

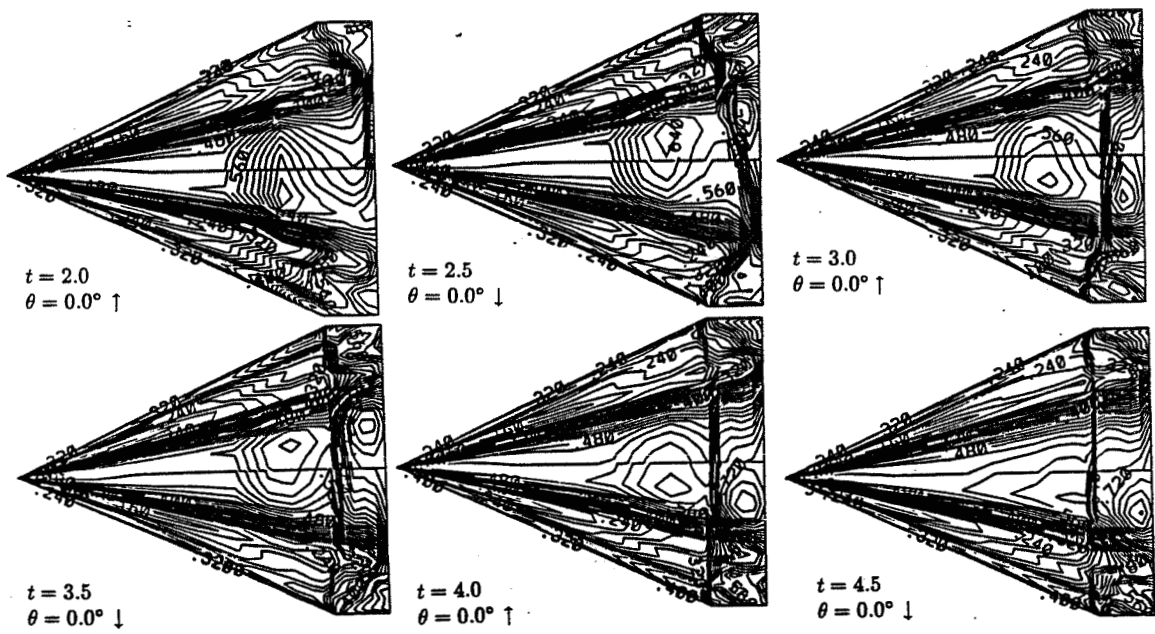


Figure 9. Samples of Static Pressure Contours on the Wing Surface.

Case I-Periodic Response

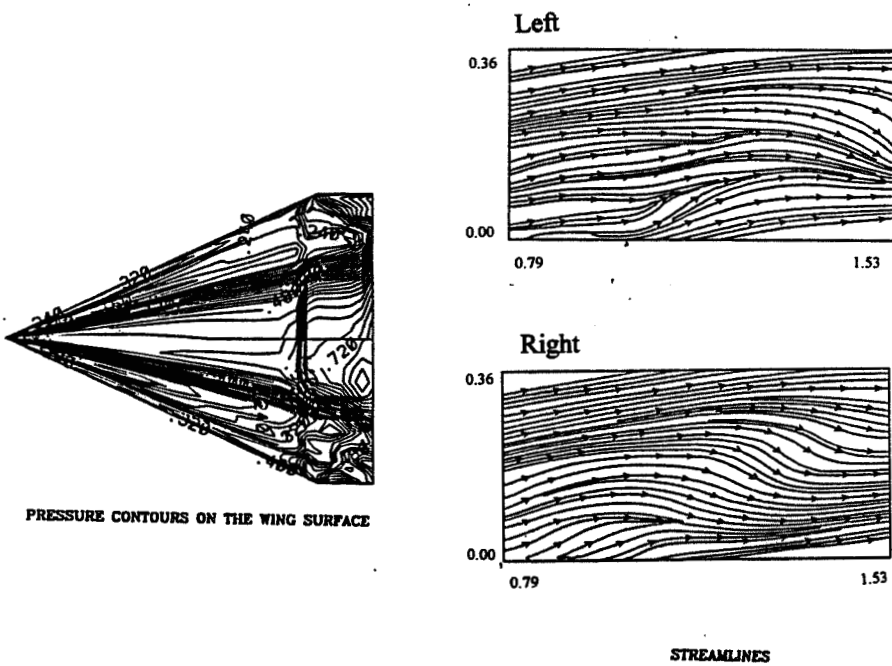


Figure 10. Static Pressure Contours on the Wing Surface and Streamlines of Vertical Planes Sectioning the Vortex at $t = 7.0$.

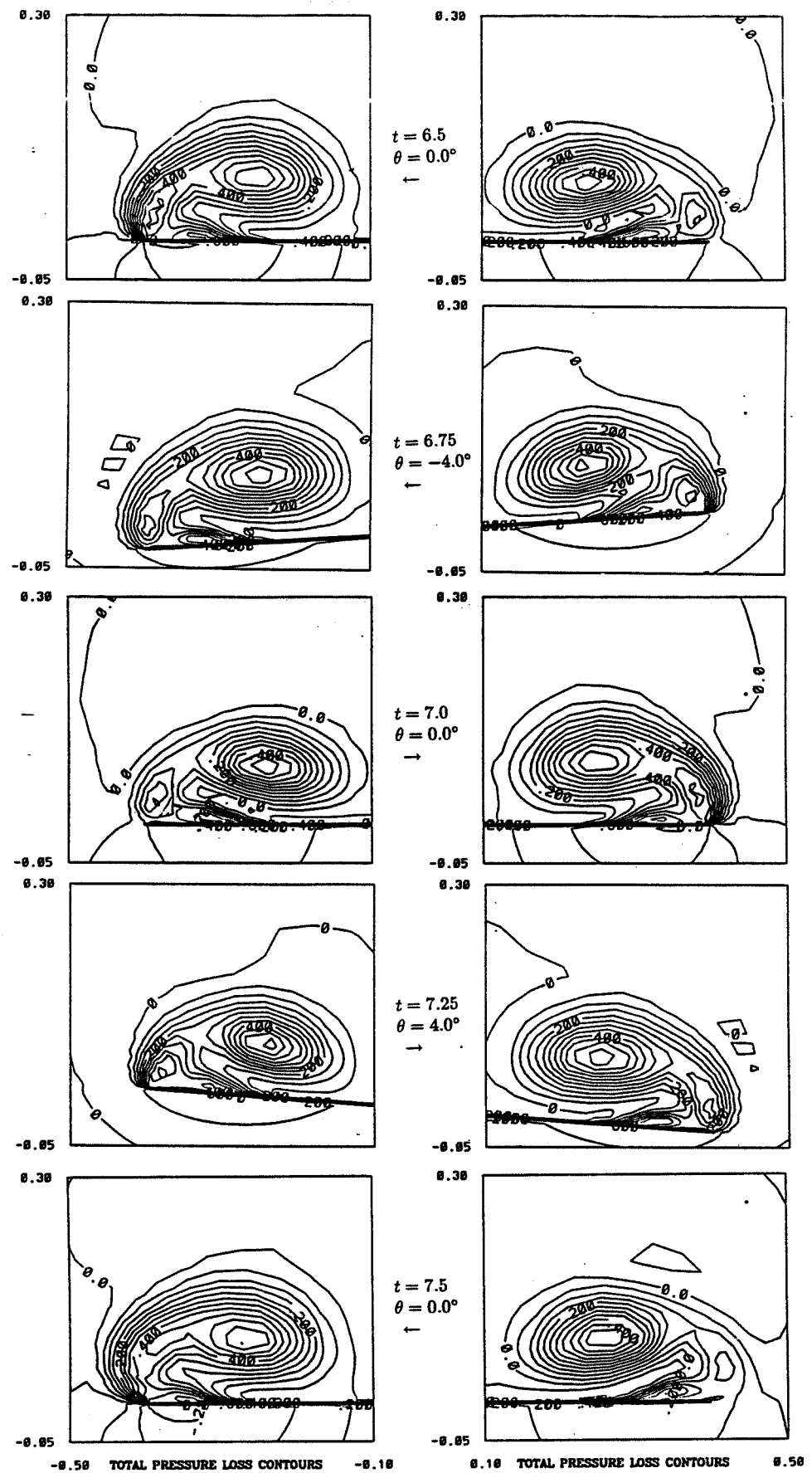


Figure 11. Typical Total Pressure Loss Contours on a Cross-Flow Plane
at $x = 0.85$, Shown at Each Quarter Cycle.

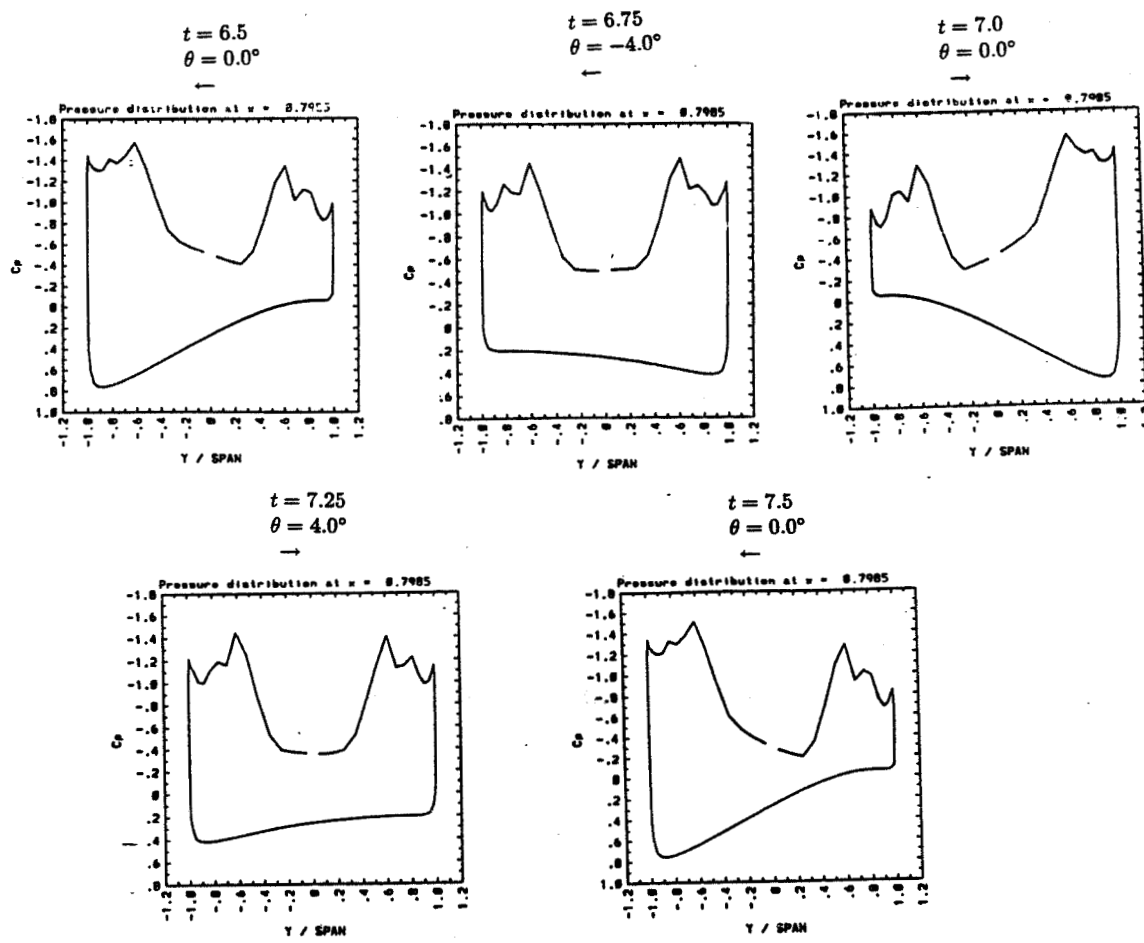


Figure 12. Snapshots of Span Wise Surface Pressure Coefficients
Shown at Each Quarter Cycle.

Case II-Transient Response

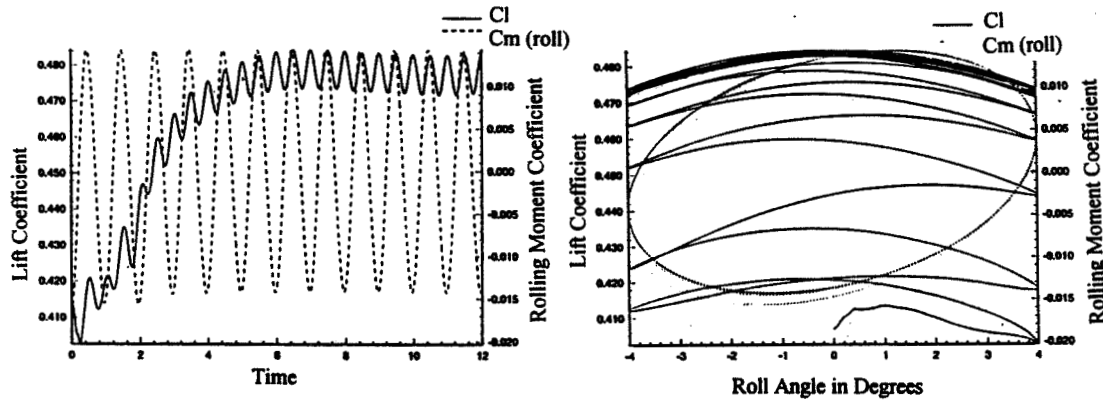


Figure 13. Coefficients of Lift and Rolling Moment versus
Time and Roll Angle During Rolling Oscillations.

$$Re = 0.50 \times 10^6, \theta = 4.0^\circ \sin 2\pi t$$

Case III-Transient Response

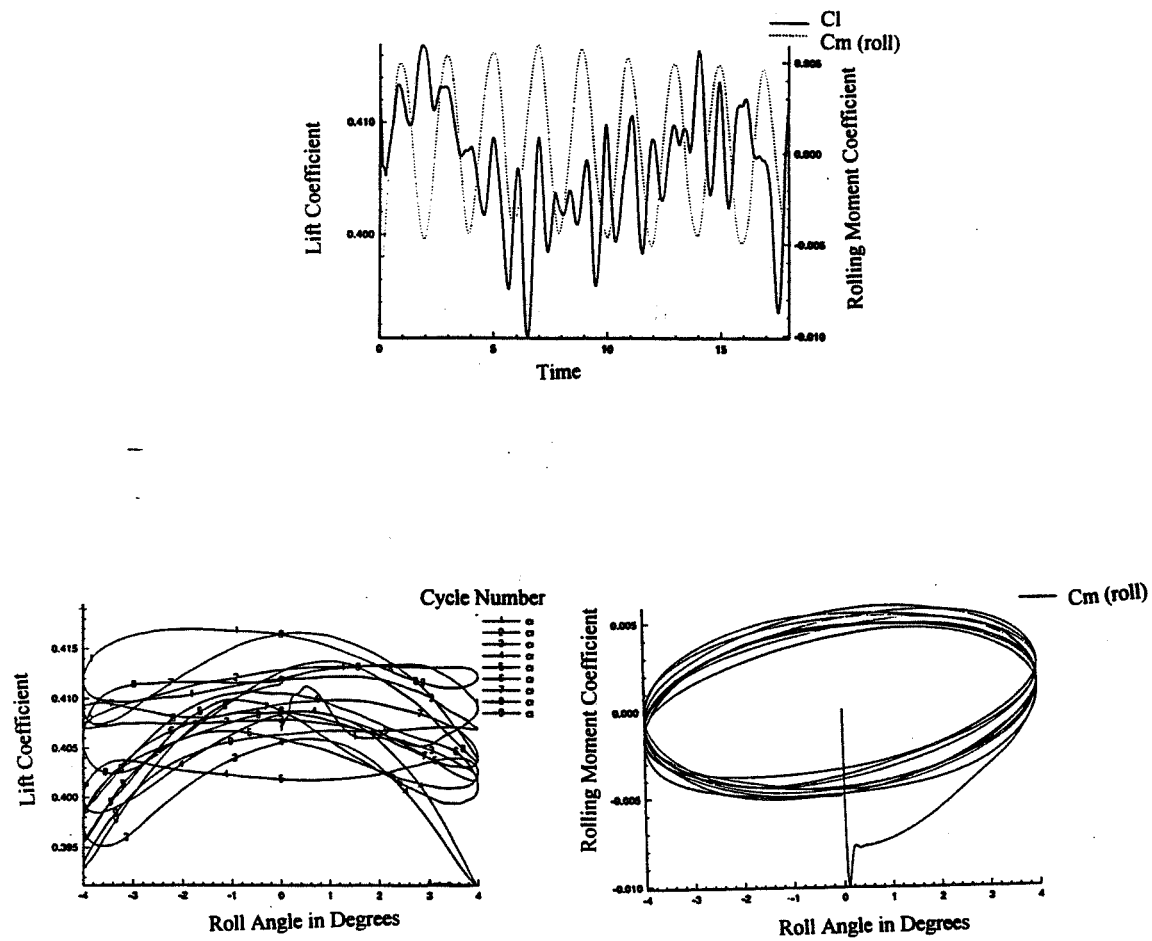


Figure 14. Coefficient of Lift and Rolling Moment versus Time and Roll Angle During Rolling Oscillations.

$$Re = 0.50 \times 10^6, \theta = 4.0^\circ \sin 1\pi t$$

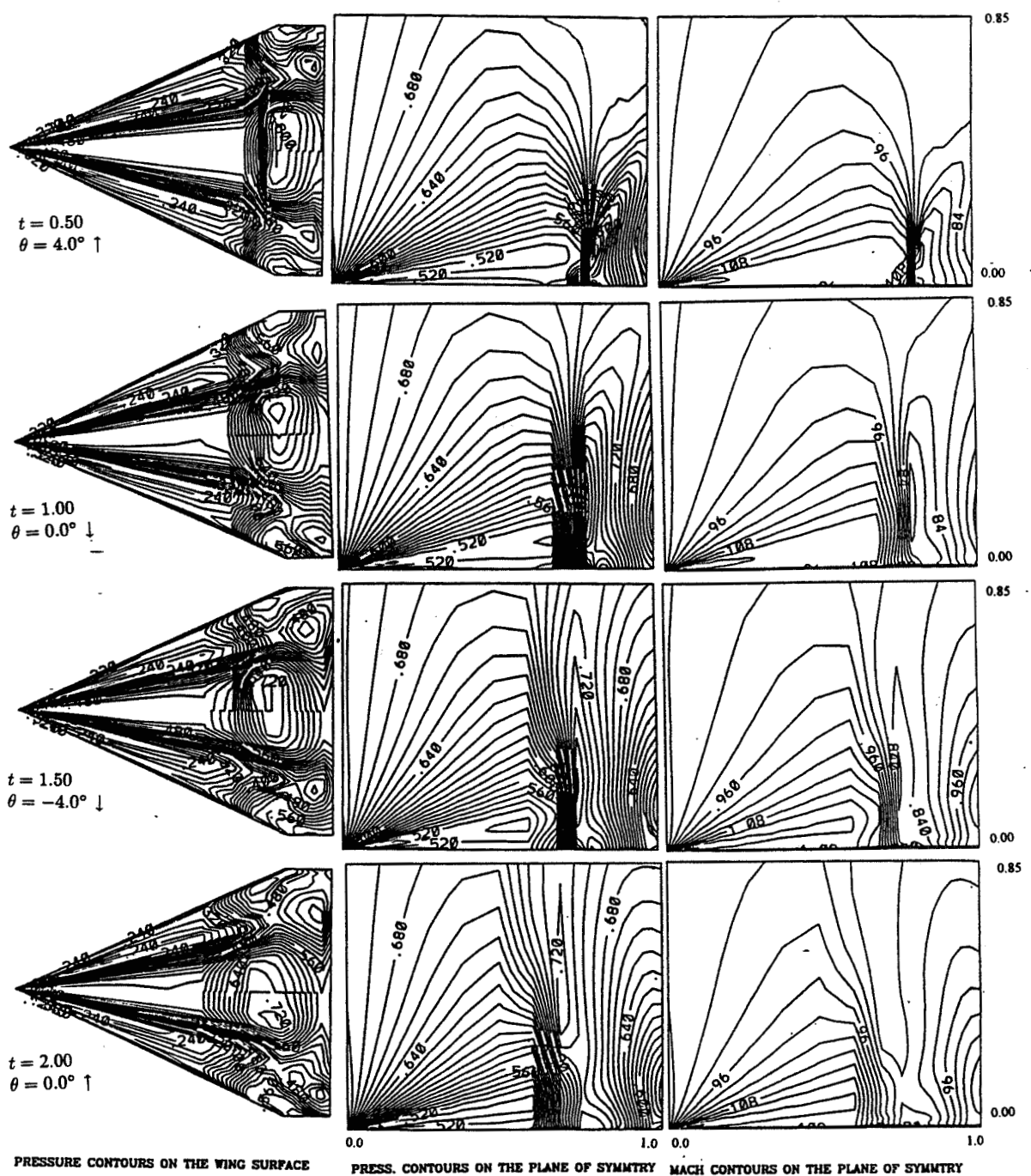


Figure 15. Snapshots of the First Cycle Shown at Each Quarter Cycle.

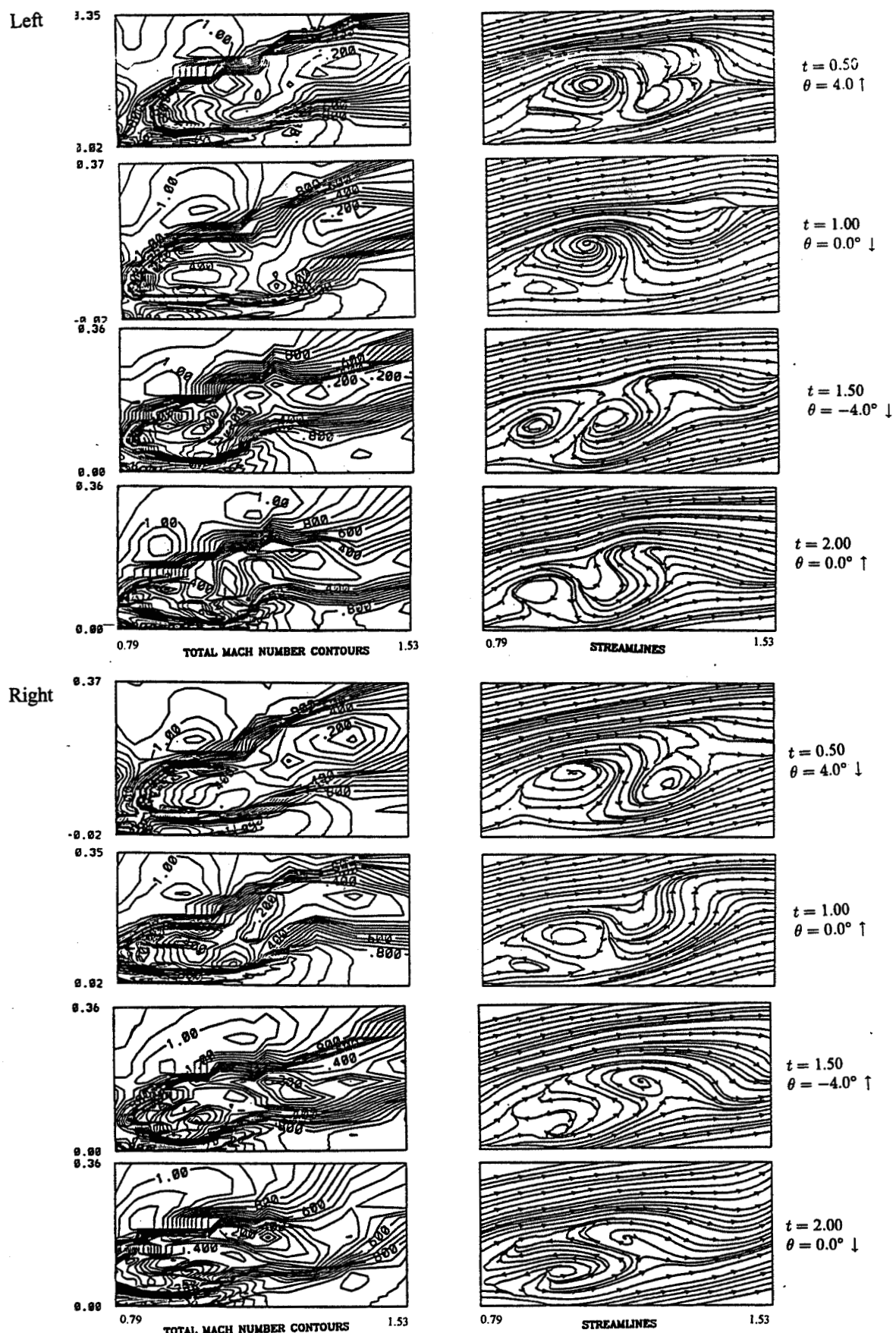


Figure 16. Snapshots of the First Cycle Shown at Each Quarter Cycle of a Vertical Plane Sectioning the Vortex Breakdown.

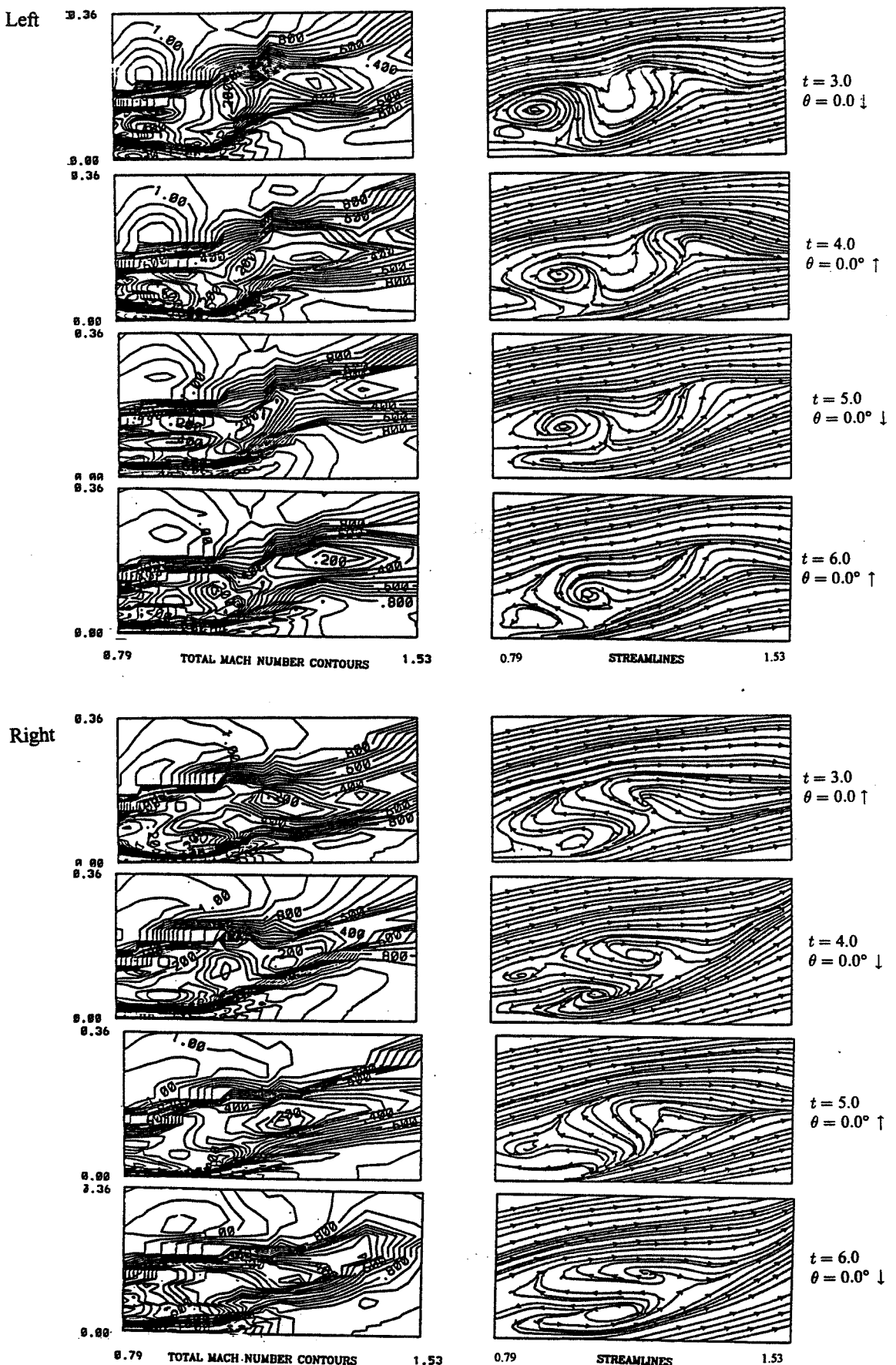
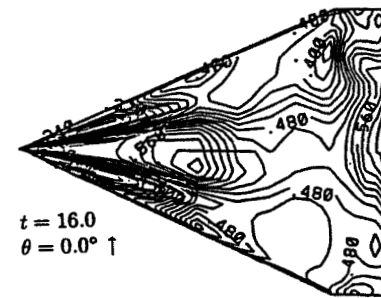
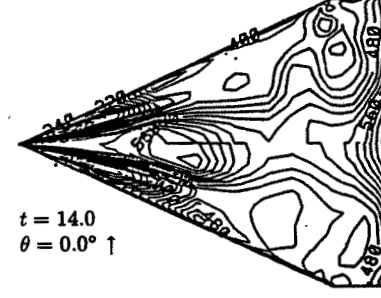
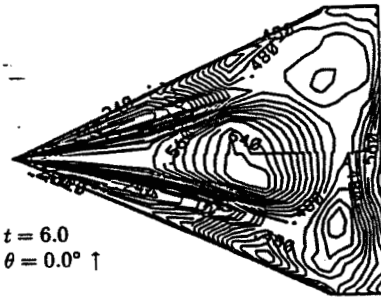
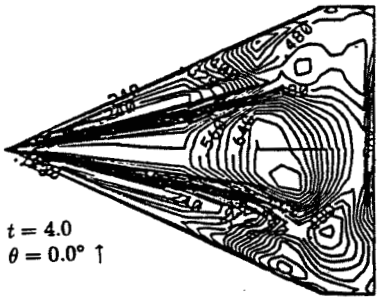
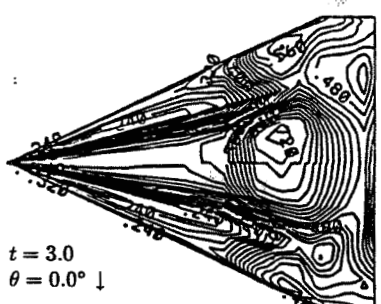
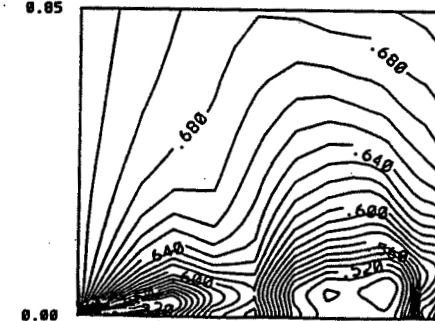
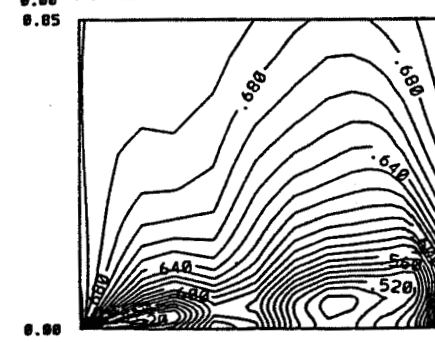
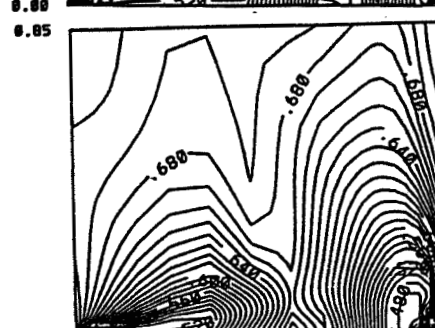
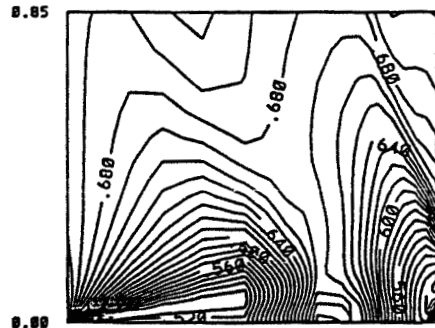
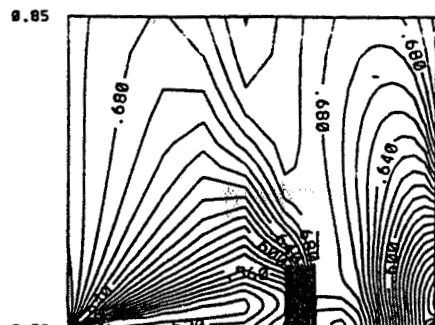


Figure 17. Selected Snapshots of the First Cycle of a Vertical Plane Sectioning the Vortex Breakdown.



PRESSURE CONTURS ON THE WING SURFACE



PRESS. CONTURS ON THE PLANE OF SYMMTRY

Figure 18. Selected Snapshots of the Pressure Contours
on the Wing Surface and on the Plane of Symmetry.

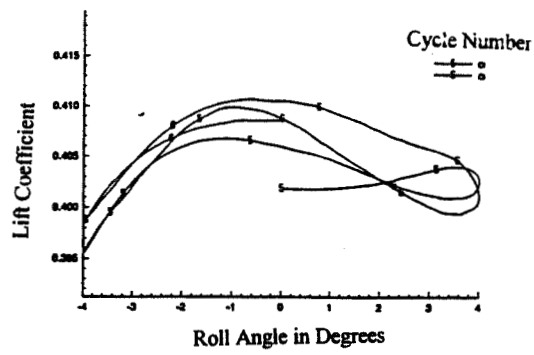


Figure 19. Coefficient of Lift versus Roll Angle for the Fifth and Sixth Cycle.

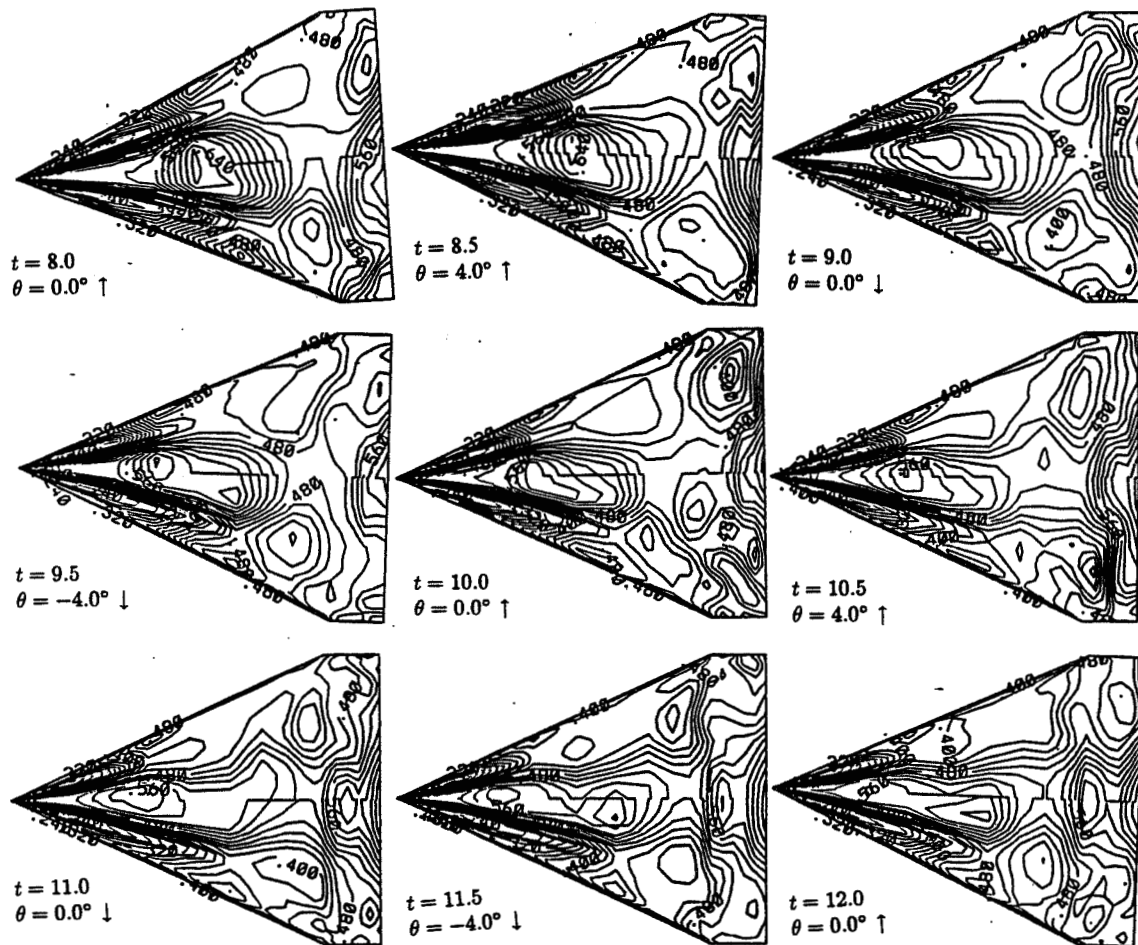


Figure 20. Snapshots of the Pressure Contours on the Wing Surface During the Fifth and Sixth Cycle.



A hybrid boundary element – finite volume method for unsteady transonic airfoil flows

Hong Hu

Department of Mathematics, Hampton University, Hampton, Virginia 23668, USA

&

Osama A. Kandil

Department of Aerospace Engineering, Old Dominion University, Norfolk, Virginia 23529, USA

(Received 9 July 1994; accepted 18 July 1994)

A hybrid boundary element – finite volume method for unsteady transonic flow computation has been developed. In this method, the unsteady Euler equations in a moving frame of reference are solved in a small embedded domain (inner domain) around the airfoil using an implicit finite volume scheme. The unsteady full-potential equation, written in the same frame of reference and in the form of the Poisson equation, is solved in the outer domain using the integral equation – boundary element method to provide the boundary conditions for the inner Euler domain. The solution procedure is a time-accurate stepping procedure, where the outer boundary conditions for the inner domain are updated using the integral equation – boundary element solution over the outer domain. The method is applied to unsteady transonic flows around the NACA0012 airfoil undergoing pitching oscillation and ramp motion. The results are compared with those of an implicit Euler equation solver, which is used throughout a large computational domain, and experimental data.

Key words: BEM–FVM coupling, unsteady transonic airfoil flows, full-potential equation, Euler equations.

INTRODUCTION

The problem of accurate and efficient prediction of unsteady transonic airfoil flows remains challenging. The well-established unsteady transonic computational codes are based on the unsteady transonic small-disturbance (UTSD) theory.^{1–4} The UTSD equations are limited to small disturbances and cannot treat flows with strong shocks and large reduced frequencies. Improved accuracy is obtained by using the unsteady full-potential (UFP) equations.^{5,6} Both UTSD and UFP formulations suffer from the isentropic flow assumption which limits their applications. Non-isentropic flow corrections of the unsteady potential formulation have been recently added to the UTSD equations⁷ and UFP equations⁸ to improve their accuracy for flows with strong shocks.

The unsteady Navier–Stokes equations represent the best mathematical model for the unsteady transonic flow since they properly model the shock development

and motion, shock-boundary layer interaction, entropy evolution and vorticity shedding. The time-accurate solution of the Navier–Stokes equations is computationally expensive due to the need for solving the flow on a fine grid. Numerical solutions of the unsteady Euler equations are less expensive than that of the unsteady Navier–Stokes equations. For unsteady transonic flows, the unsteady Euler equations adequately model most of the flow features with the exception of viscous effects near solid walls, where they are substantial. Recently, successful time-accurate solutions of the unsteady Euler equations have been obtained for a pitching airfoil.⁹

However, the finite-difference (FD) or finite-volume (FV) computation of the unsteady Euler equations requires a large computational domain, whose outer boundary extends 20–30 airfoil chord lengths from the airfoil boundary, and hence they are still expensive. On the other hand, the integral equation (IE) – boundary element (BE) solution of the full-potential

equation represents an alternative to the FD or FV solution of the Euler equations for inviscid flows without shocks or with weak shocks. Recently, IE-BE solutions of the unsteady full-potential equation have been obtained for unsteady inviscid transonic flows.^{10,11} Also, an IE-BE with embedded Euler domain method, a hybrid BE-FV method, has been developed for steady inviscid transonic flows with strong shocks.^{12,13} In the latter method, the unsteady Euler equations were solved by using an FV scheme in the small domain around the shock, while the IE-BE solution of the full-potential equation was obtained in the region outside this Euler domain. This method has been shown to be efficient and accurate in treating transonic flows with strong shocks. The advantages of the IE-BE method in using a small computational domain and a coarse grid (or large boundary elements) have been utilized. For unsteady transonic flows with strong shocks, this hybrid method is highly desirable for further development.

In the present paper, the development of this hybrid method for unsteady flows is presented. The resulting method is applied to the NACA0012 airfoil undergoing pitching oscillation and ramp motion.

FORMULATION

For a general unsteady motion of a body, the governing equations of the fluid flow are simple to solve if a moving (body-fixed) frame of reference formulation is used. This formulation does not require the grid-motion calculation since the grid is rigidly fixed in the frame. In addition to the space-fixed frame of reference $OXYZ$, a moving frame of reference $oxyz$ is introduced as shown in Fig. 1. The moving frame of reference $oxyz$ is translating at a velocity of $\vec{V}_o(t)$ and rotating around a pivot point, $\mathbf{r}_p = (x_p, y_p, z_p)$, at an angular velocity of $\Omega(t)$. The relationship among the absolute velocity (\mathbf{V}), relative velocity [$\mathbf{V}_r = (u_r, v_r)$] and transformation

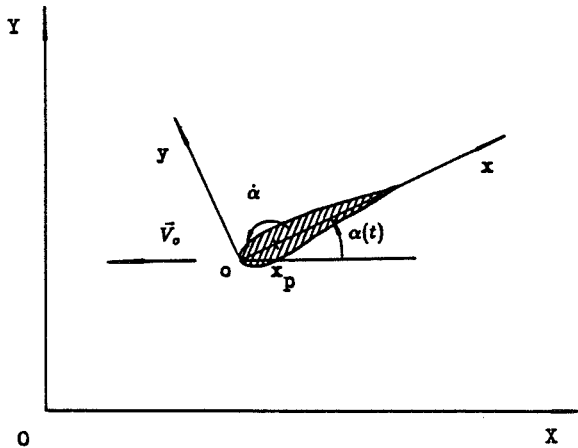


Fig. 1. Frames of reference for unsteady airfoil flows.

velocity [$\mathbf{V}_o + \mathbf{V}_r = \mathbf{V}_o + \Omega \times (\mathbf{r} - \mathbf{r}_p)$] is given by

$$\mathbf{V} = \mathbf{V}_r + \mathbf{V}_o + \Omega \times (\mathbf{r} - \mathbf{r}_p) \quad (1)$$

where \mathbf{r} is the position vector measured in the moving frame of reference.

Unsteady euler equations

The conservative form of the two-dimensional, unsteady Euler equations in the moving frame of reference is given⁹ by

$$\frac{\partial \mathbf{q}_r}{\partial t} + \frac{\partial \mathbf{E}_r}{\partial x} + \frac{\partial \mathbf{F}_r}{\partial y} = \mathbf{S} \quad (2)$$

where

$$\mathbf{q}_r = [\rho, \rho u_r, \rho v_r, \rho e_r]^t \quad (3)$$

$$\mathbf{E}_r = [\rho u_r, \rho u_r^2 + p, \rho u_r v_r, \rho u_r h_r]^t \quad (4)$$

$$\mathbf{F}_r = [\rho v_r, \rho u_r v_r, \rho v_r^2 + p, \rho v_r h_r]^t \quad (5)$$

$$\begin{aligned} \mathbf{S} = & \{0, \rho[\ddot{\alpha}(y - y_p) + 2\dot{\alpha}v_r + \dot{\alpha}^2(x - x_p)], \\ & \rho[-\ddot{\alpha}(x - x_p) - 2\dot{\alpha}u_r + \dot{\alpha}^2(y - y_p)], \\ & -\rho[u_o(\ddot{\alpha}(y - y_p) + \dot{\alpha}v_r + \dot{\alpha}^2(x - x_p)) \\ & + v_o(\ddot{\alpha}(x - x_p) + \dot{\alpha}u_r - \dot{\alpha}^2(y - y_p)) \\ & - \ddot{\alpha}(u_r(y - y_p) - v_r(x - x_p) \\ & - \dot{\alpha}(x - x_p)^2 - \dot{\alpha}(y - y_p)^2)]\}^t \end{aligned} \quad (6)$$

The total energy (e_r) and the rothalpy (h_r) per unit mass as referred to the moving frame of reference are given by

$$\begin{aligned} e_r = & \frac{p}{\rho(\kappa - 1)} + \frac{u_r^2 + v_r^2}{2} - \frac{u_o^2 + v_o^2}{2} \\ & - \frac{\dot{\alpha}^2}{2} [(x - x_p)^2 + (y - y_p)^2] \end{aligned} \quad (7)$$

and

$$\begin{aligned} h_r = & \frac{\kappa p}{\rho(\kappa - 1)} + \frac{u_r^2 + v_r^2}{2} - \frac{u_o^2 + v_o^2}{2} \\ & - \frac{\dot{\alpha}^2}{2} [(x - x_p)^2 + (y - y_p)^2] \end{aligned} \quad (8)$$

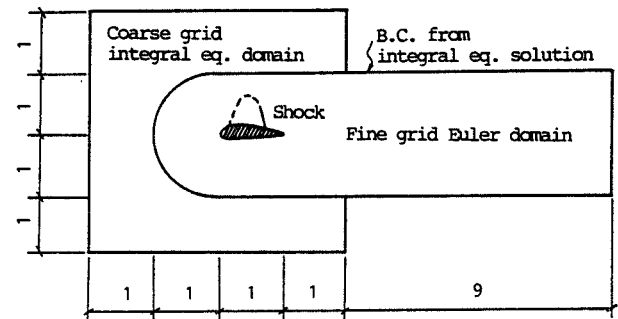


Fig. 2. Euler domain and IE-BE domain.

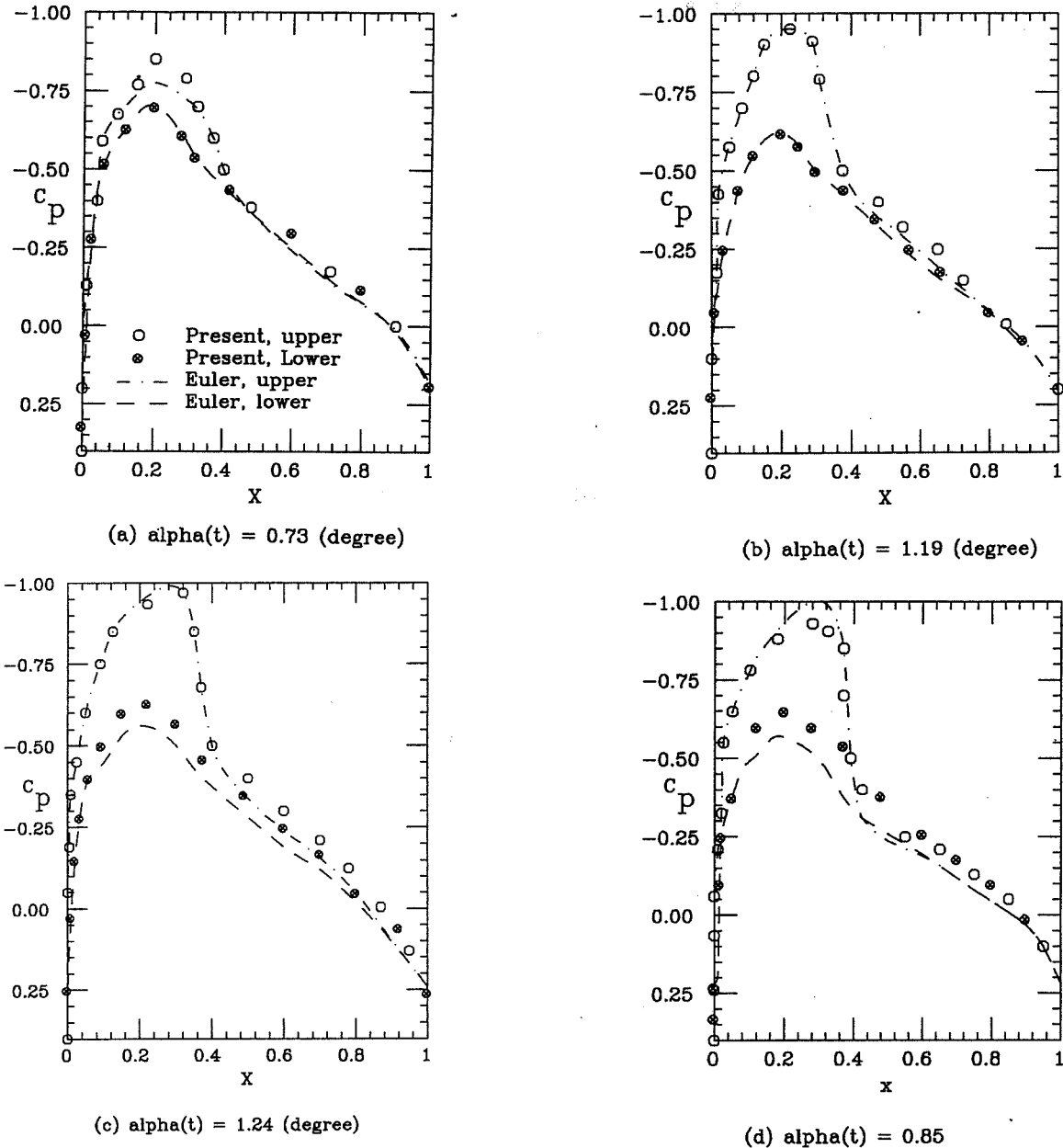


Fig. 3. Unsteady surface pressure distribution at different time level during pitching oscillation, $M_\infty = 0.755$, $\alpha = 0.016^\circ + 1.255^\circ \sin(0.1632t)$.

respectively. In eqns (2)–(8), the flow vector field (\mathbf{q}_r) and the inviscid fluxes (\mathbf{E}_r and \mathbf{F}_r) are based on the relative velocity. The source term (\mathbf{S}) is an algebraic term contributed from the motion of the moving frame of reference, which has been written for pitching oscillation or ramp motion at an angular velocity and angular acceleration of $\Omega = \dot{\alpha}\mathbf{k}$ and $\ddot{\Omega} = \ddot{\alpha}\mathbf{k}$, respectively. The translation velocity is \mathbf{V}_o , and u_o and v_o are its Cartesian components. p is the pressure, ρ the density, t the time, and κ the gas specific-heat ratio. The subscript r refers to the relative values with respect to the moving frame of reference.

Unsteady full-potential equation

The non-dimensional unsteady full-potential equation in the moving frame of reference has been derived as follows:^{10,11}

$$\nabla^2 \Phi = G_1 + G_2 \quad (9)$$

with

$$G_1 = -\frac{\nabla \rho}{\rho} \cdot \mathbf{V}_r \quad (10)$$

$$G_2 = -\frac{1}{\rho} \frac{\partial \rho}{\partial t} \quad (11)$$

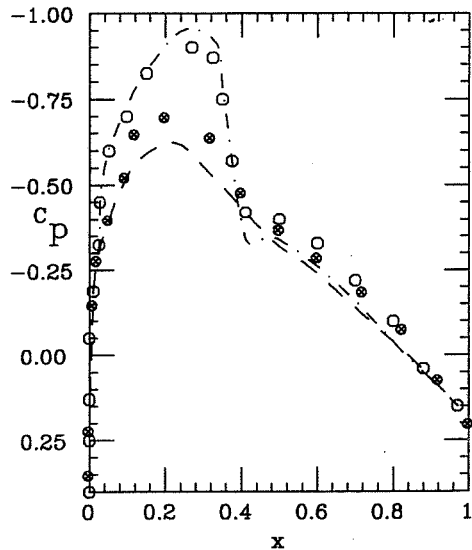
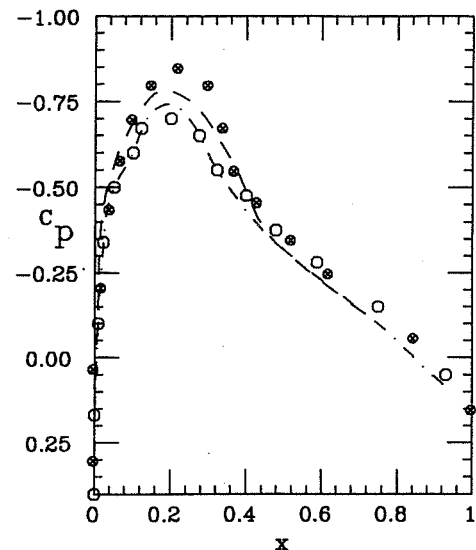
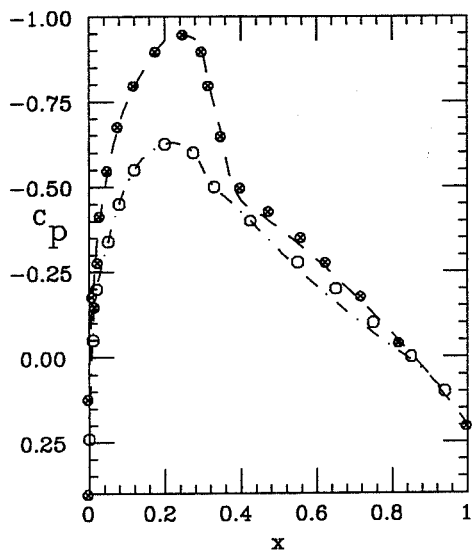
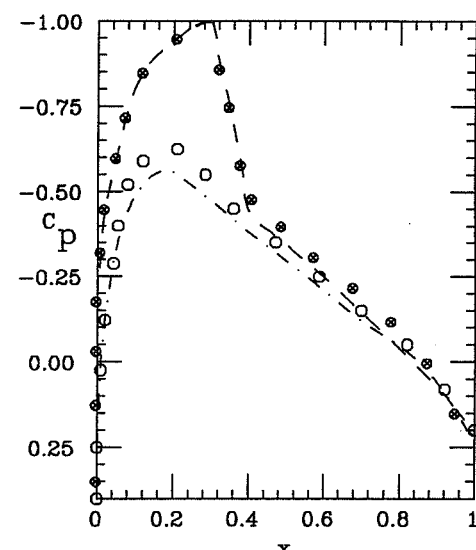
(e) $\alpha(t) = 0.17$ (degree)(f) $\alpha(t) = -0.70$ (degree)(g) $\alpha(t) = -1.16$ (degree)(h) $\alpha(t) = -1.20$ (degree)

Fig. 3. — contd.

and

$$\rho = \left\{ 1 + \frac{\kappa - 1}{2} M_\infty^2 \left[-V_r^2 + (\mathbf{V}_o + \mathbf{V}_e)^2 - 2 \left(\frac{\partial \Phi}{\partial t} \right) \right] \right\}^{1/\kappa-1} \quad (12)$$

where Φ is the absolute velocity potential ($\mathbf{V} = \nabla \Phi$), G_1 the compressibility, and G_2 the unsteadiness.

Integral equation-boundary element solution

Equation (9) is a Poisson equation. By using the Green theorem, the IE-BE solution of eqn (9) in terms of the

absolute velocity field is given by

$$\begin{aligned} \mathbf{V}(x, y, t) = & \frac{1}{2\pi} \int_g \gamma_g \frac{(y - \eta)\mathbf{i} - (x - \xi)\mathbf{j}}{(x - \xi)^2 + (y - \eta)^2} ds(\xi, \eta) \\ & + \frac{1}{2\pi} \iint G_1 \frac{(x - \xi)\mathbf{i} + (y - \eta)\mathbf{j}}{(x - \xi)^2 + (y - \eta)^2} d\xi d\eta \\ & + \frac{1}{2\pi} \iint G_2 \frac{(x - \xi)\mathbf{i} + (y - \eta)\mathbf{j}}{(x - \xi)^2 + (y - \eta)^2} d\xi d\eta \\ & + \frac{1}{2\pi} \int_w \gamma_w \frac{(y - \eta)\mathbf{i} - (x - \xi)\mathbf{j}}{(x - \xi)^2 + (y - \eta)^2} ds(\xi, \eta) \end{aligned} \quad (13)$$

where γ is the surface vorticity distribution; the subscripts g and w refer to the wing and wake

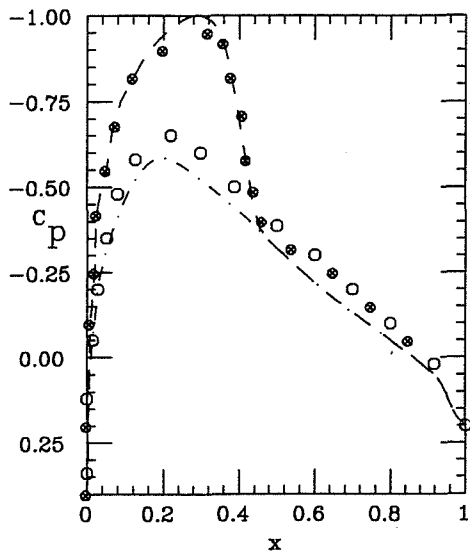
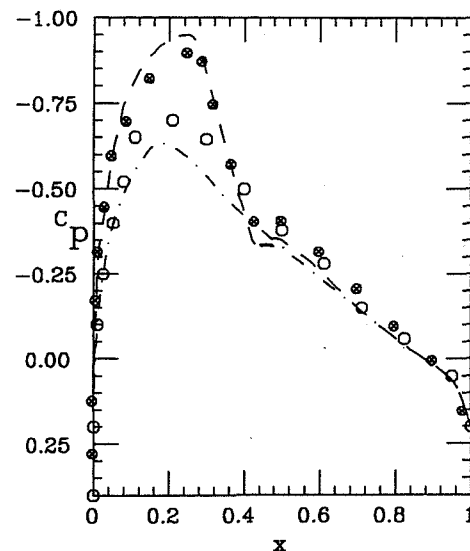
(i) $\alpha(t) = -0.82$ (degree)(j) $\alpha(t) = -0.14$ (degree)

Fig. 3. — contd.

surfaces, respectively; and ds is the infinitesimal surface area.

The first integral term of eqn (13) is the contribution of the airfoil surface vorticity (γ_g); the second and the third integral terms are the contributions of the full compressibility (G_1) and the unsteadiness (G_2), respectively. The last integral term is the contribution of the wake vorticity (γ_w) shed at the airfoil trailing edge and convected in the flow field. It should be noticed that the IE solution, eqn (13), automatically satisfies the far-field boundary condition, since $\mathbf{V}(x, y, t) \rightarrow 0$ when $(x, y) \rightarrow \infty$. Therefore, only a small computational domain around the airfoil is needed.

COMPUTATIONAL SCHEMES

Computational domains

A sketch of an Euler computational domain inside a full-potential IE domain is shown in Fig. 2. The domain sizes are also shown in Fig. 2. In this zonal scheme, the unsteady Euler equations are solved using an implicit, approximately-factored, central-difference, FV scheme.⁹ The outer boundary conditions are provided by the IE-BE solution of the unsteady full-potential equation. The IE-BE computation in the region outside the embedded Euler inner domain is carried out simultaneously with the unsteady Euler computation, but relatively larger time steps are used.

Solution procedure

The steps of the solution procedure of this hybrid method can be described as follows.

Step 1 — Euler time marching

Starting with the initial conditions, which may correspond to a steady flow solution, the FV Euler computation in the small embedded domain is carried out for several time steps.

Step 2 — IE-BE computations for boundary conditions

The IE-BE computation in the outer domain over a coarse grid is then carried out to provide the boundary conditions for the Euler inner domain. In this step, the airfoil surface vorticity (γ_g) is calculated by numerical integration around the airfoil along a closed path, while

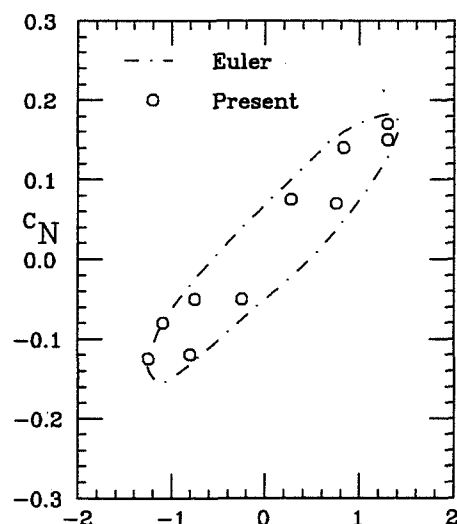


Fig. 4. Normal-force coefficient during one cycle of periodic flow response for pitching oscillation.

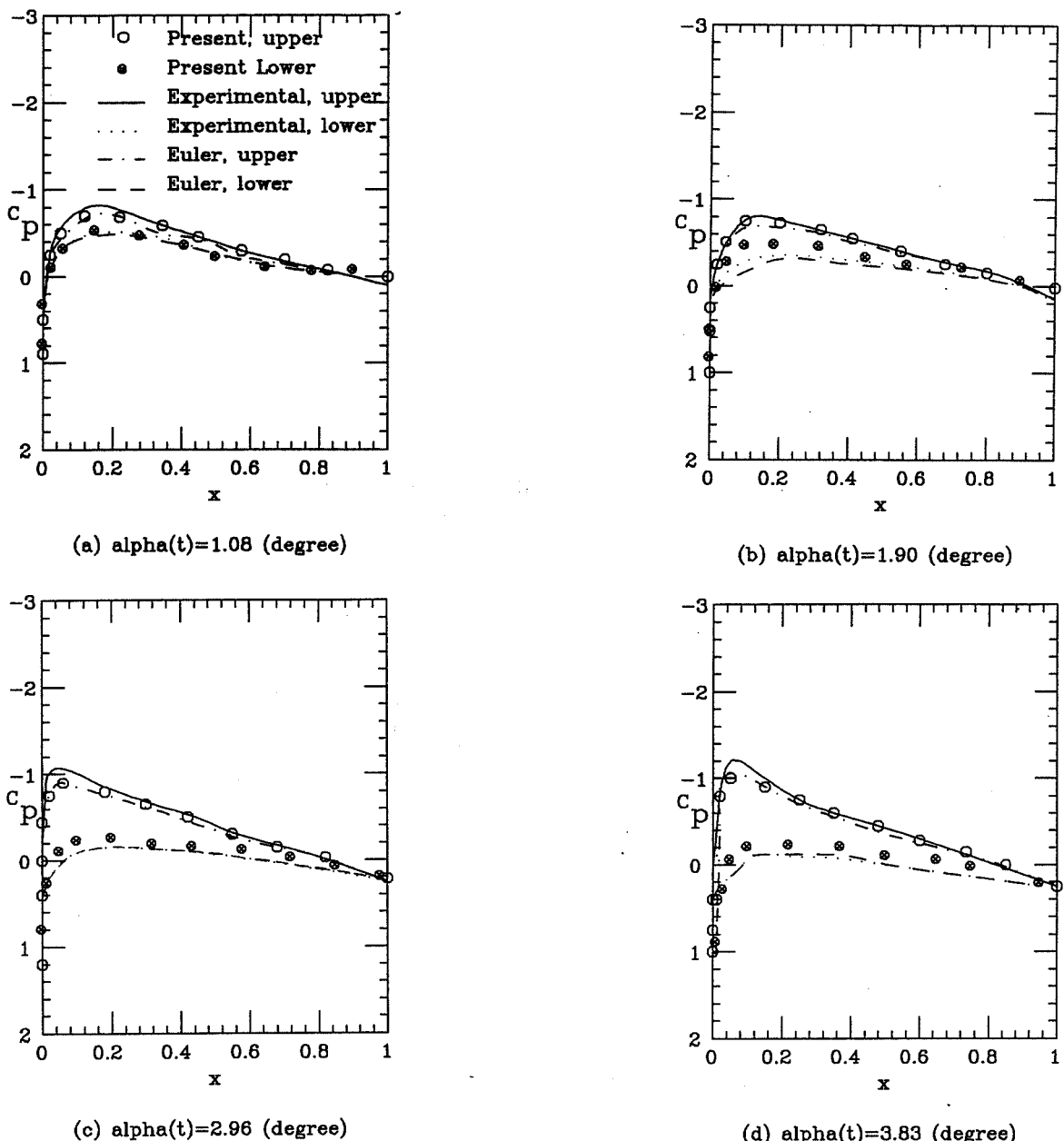


Fig. 5. Unsteady surface pressure distribution at different time levels during transient ramp motion, $M_\infty = 0.56$, $\alpha = -0.01^\circ + 0.855t$.

the wake vorticity (γ_w) is determined by the fact that the total circulation is conserved. Once the vorticities are determined and the Euler solutions are interpolated into the IE-BE coarse grid, eqns (10)–(12) are used to calculate ρ , G_1 and G_2 . Then, eqn (13) along with eqn (1) is used to compute the outer boundary conditions for the inner Euler domain.

Step 3 — Euler time marching

With initial conditions obtained from the previous Euler computation and boundary conditions obtained from the IE-BE computation, Step 1 is repeated for the next several time steps.

Step 4

Steps 2 and 3 are repeated to march in time. For the periodic oscillation, the time marching is continued until periodic flow response is achieved.

COMPUTATIONAL APPLICATIONS

The present method has been applied to two unsteady flow cases around the NACA0012 airfoil. The first application is that of unsteady transonic flow around an airfoil which is undergoing a forced pitching oscillation about an axis at the quart-chord length. The second

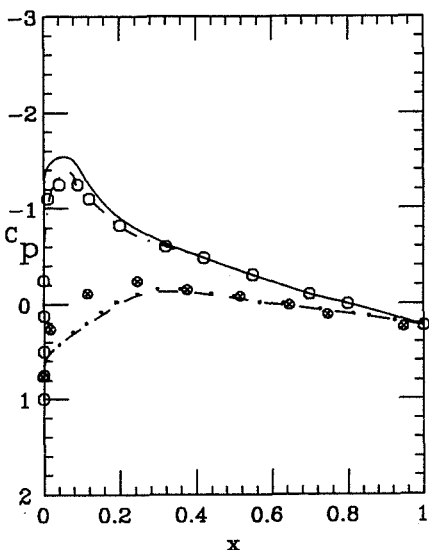
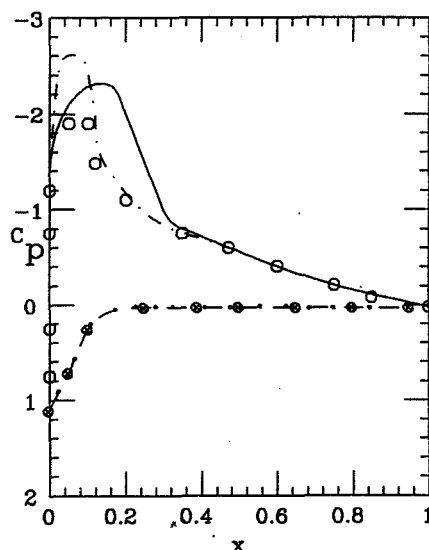
(e) $\alpha(t) = 4.70$ (degree)(f) $\alpha(t) = 7.57$ (degree)

Fig. 5. — contd.

application is that of unsteady transonic flow around an airfoil which is undergoing a forced transient ramp motion about an axis at the quard-chord length.

The computational domains are shown in Fig. 2. The Euler domain ahead of the airfoil is one half of a circle whose radius is one chord length and its center is at the leading edge. The Euler domain extends 10 chords behind the trailing edge with a lateral width of two chords. The IE-BE domain surrounds the Euler domain, as shown in the figure, with dimension of 4×4 chords. The grid in the Euler domain is generated using an elliptic-grid generator with 128×42 in the wrap-around and normal directions of the airfoil.

The computational results of the present method are compared with those of the Euler method of Ref. 9 which is used throughout a large Euler computational domain and experimental data if available. This domain extends 10 chords in the directions ahead of the leading edge, laterally from the airfoil surface and behind the trailing edge. The grid for the Euler method is 128×64 in the wrap-around and normal directions of the airfoil and it is also generated using the same elliptic generator.

Pitching oscillation

The free-stream Mach number of this flow is 0.755 and the pitching oscillation is given by

$$\alpha(t) = \alpha_m + \alpha_a \sin(kt) \quad (14)$$

where $\alpha(t)$ is the instantaneous angle of attack, α_m is the mean angle of attack which equals 0.016° , α_a is angle-of-attack amplitude which equals 1.255° , and k is reduced frequency which is based on the airfoil chord length and equals 0.1632 . The time step of the time-accurate

stepping is 0.01, and the periodic flow response has been achieved in the third cycle of oscillation.

In Fig. 3, we show snapshots of the computed surface pressure using the present method and the Euler method of Ref. 9 during the third cycle of periodic flow response. Figure 3(a)–(e) show the surface pressure during the first half of the cycle and Fig. 3(f)–(j) show the surface pressure during the second half of the cycle. As the angle of attack increases, a shock is formed on the upper surface and it then moves in the downstream direction with an increasing strength. As the angle of attack decreases, the shock moves in the upstream direction until it disappears from the upper surface when the angle of attack reaches a near-zero value. When the angle of attack becomes negative, the shock is formed on the lower surface and it then moves in the downstream direction with an increasing strength until the angle of attack reaches its maximum negative value. Finally, as the angle of attack increases to zero value completing the cycle, the shock moves in the upstream direction with diminishing strength.

The results of the two methods show excellent agreement for the shock motion. However, there are discrepancies between the magnitudes of the pressure coefficient of the two methods which do not exceed 7%. Figure 4 shows a comparison of the two methods for the history of the normal-force coefficient versus the angle of attack during the third cycle of the periodic flow response. The hysteresis loop of the present hybrid method is slightly slender and its axis has slightly less slope than those of the Euler method. The computational time of the present method is 70% that of the Euler method.

Transient ramp motion

The free-stream Mach number of this flow is 0.56 and the ramp function of the angle of attack is given by

$$\alpha(t) = \alpha_i + \omega t \quad (15)$$

where α_i is the initial angle of attack which equals -0.01° and ω is the reduced angular velocity which equals 0.855° per unit time. The step of the time-accurate stepping is also 0.01 .

In Fig. 5, we show snapshots of the computed surface pressure at several time steps using the present hybrid method and the Euler method of Ref. 9, along with the experimental data of Ref. 14. Figure 5(a) shows the solutions along with the experimental data at $\alpha = 1.08^\circ$. The present solution is in excellent agreement with that of the Euler solution and with the experimental data. At $\alpha = 1.9^\circ, 2.96^\circ$ and 3.83° , as shown in Fig. 5(b)-(d), we see good agreement of the present results with those of the Euler method and the experimental data with the exception of slight under-prediction at the locations of the maximum pressure on the upper surface. At $\alpha = 4.7^\circ$ of Fig. 5(e), we see a shock is formed on the upper surface. Both the present method and the Euler method under-predict the pressure in the vicinity of the shock. As the angle of attack increases, the discrepancy between the experimental data and the inviscid solutions in the shock region increases. For example, at $\alpha = 7.57^\circ$ of Fig. 5(f), we see that the present method under-predicts the peak pressure while the Euler method over-predicts it. Both methods do not predict the experimental shock location. We attribute these differences to the absence of the viscous terms including the turbulence effects from the inviscid methods. Figure 6 shows a

comparison of the two methods along with the experimental data for the history of the normal-force coefficient versus the angle of attack during the ramp motion. The computational time of the present method is 70% that of the Euler method.

CONCLUDING REMARKS

A hybrid BE-FV method for unsteady transonic flow computations has been developed. Since the Euler equations are solved in a small computational domain, the present hybrid method requires less computational time than other existing Euler methods, which solve Euler equations in the whole computational domain. This hybrid method has been applied to unsteady transonic flows around the NACA0012 airfoil undergoing pitching oscillation and ramp motion. The computational time required for the present applications is 70% that of the computational time for the same applications using the Euler equation solver throughout the whole computational domain. The reduction of the computational time is very promising and in particular for three-dimensional transonic flow computations.

ACKNOWLEDGEMENT

This research work has been partially supported under Grant No. NAG-1-648 from the NASA Langley Research Center.

REFERENCES

1. Ballhaus, W. F. & Goorjian, P. M. Implicit finite-difference computations of unsteady transonic flows about airfoils. *AIAA Journal*, 1977, **15**(12), 1728-35.
2. Whitlow, W., Jr, XGTRAN2L: a program for solving the general-frequency unsteady transonic small disturbance equation. NASA TM-85723, 1983.
3. Edwards, J. W., Bland, S. R. & Seidel, D. A. Experience with transonic unsteady aerodynamic calculations. NASA TM-86278, 1984.
4. Goorjian, P. M. & Guruswamy, G. P. Unsteady transonic aerodynamic and aeroelastic calculations about airfoils and wings. AGARD CP-374, 1985.
5. Chipman, R. & Jameson, A. Full conservative numerical solutions for unsteady irrotational transonic flow about airfoils. AIAA Paper 79-1555, 1979.
6. Goorjian, P. M. Implicit computations of unsteady transonic flow governed by the full potential equation in conservative form. AIAA Paper 80-0150, 1980.
7. Fuglsang, D. & Williams, M. H. Non-isentropic unsteady transonic small disturbance theory. AIAA Paper 85-0600, 1985.
8. Whitlow, W., Jr, Hafez, M. M. & Osher, S. J. An entropy correction method for unsteady full potential flows with strong shocks. NASA TM-87769, 1986.
9. Kandil, O. A. & Chuang, H. A. Unsteady transonic airfoil

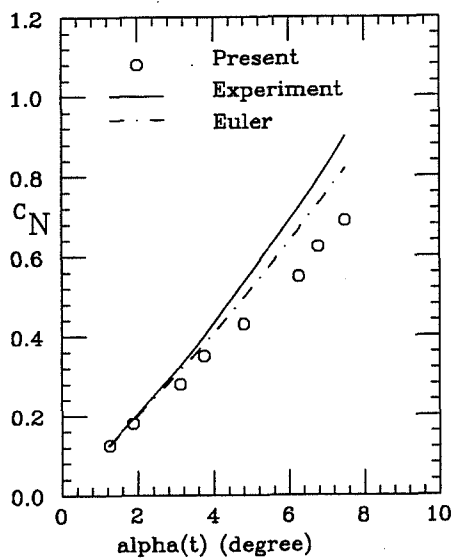


Fig. 6. Normal-force coefficient during transient ramp motion.

- computation using implicit Euler scheme on body-fixed grid. *AIAA Journal*, 1989, **27**(8), 1031–6.
- 10. Kandil, O. A. & Hu, H. Integral solution of unsteady full-potential equation for a transonic pitching airfoil. *Journal of Aircraft*, 1990, **27**(2), 123–30.
 - 11. Hu, H. Unsteady transonic wing flow computations using field-boundary element methods. *Engineering Analysis with Boundary Elements*, 1992, **10**(2), 99–105.
 - 12. Kandil, O. A. & Hu, H. Full-potential integral solution for transonic flows with and without embedded Euler domains. *AIAA Journal*, 1988, **26**(9), 1074–86.
 - 13. Hu, H. Study of integral equation methods for transonic flow calculations. *Engineering Analysis with Boundary Elements*, 1993, **11**(2), 101–7.
 - 14. Landon, R. H. NACA0012 oscillatory and transient pitching. AGARD R-702, 1982, pp. 3.1–25.